学位論文

Study of a cryogenic suspension system for the gravitational wave telescope KAGRA (重力波望遠鏡KAGRAのための低温懸架システムの研究)

平成26年12月博士（理学）申請

東京大学大学院理学系研究科
天文学専攻
陳　タン

Abstract

Gravitational wave is a propagation ripple of space-time at the speed of light, predicted by Albert Einstein around a century ago. Since the gravitational wave has extremely weak interaction against material, the permeability is very high. This also means that the gravitational wave should be a new observation window to the universe. Hulse and Taylor showed the existence of the gravitational wave indirectly by the observation of a binary pulsar. They received the Nobel Prize in 1993 for this discovery. But the gravitational wave has not been observed directly until now.

For creating a new gravitational wave astronomy, large interferometer gravitational wave telescopes such as Advanced LIGO, Advanced VIRGO, GEO and KAGRA are under upgrade or being built currently. The most common type telescope for the gravitational wave is currently large Michelson interferometer. The Michelson interferometer measures the change of the distance between "free" masses (actually, suspended mirrors). Because the effect of the gravitational wave is extremely weak, many noises should be suppressed. For example, in order to suppress the seismic vibration noise, multi suspension systems are used for the mirrors in the telescopes. Besides this seismic motion, thermal noise from the mirrors, coatings and suspension are also the fundamental noise sources.

KAGRA is the project to construct the first km-scale cryogenic interferometric gravitational wave telescope (for thermal noise reduction) in the Kamioka mine, an underground site with a small seismic motion. The main mirror of KAGRA will be held by a cryogenic suspension system under a super seismic attenuation system. A study of this cryogenic suspension system which holds the cryogenic mirror is necessary to confirm and improve the performance of KAGRA. The cryogenic suspension system consists of a platform, an intermediate mass, a recoil mass of the intermediate mass, a recoil mass for the mirror and a sapphire mirror suspended by sapphire fibers. The cryogenic suspensions will be cooled down to $\sim$20 K using cryostats. Each cryostat consists of double radiation shields surrounding the cryogenic suspension system in a vacuum chamber. Four pulse tube cryocoolers for each cryostat will cool the shields. This suspension system will be cooled by thermal radiation and thermal contact via the fibers and soft heat links between the suspension and the cryocoolers. There are two issues to be investigated in the suspension and cooling system, which are described in this thesis. One is the suspension thermal noise from the sapphire suspension system. The other one is the vibration noise from the cooling system via heat links.

The sapphire suspension consists of a mirror, two ears attached on the mirror, four fibers with heads suspending the mirror with the ears, and four blades to support the fibers. All of these components are made of sapphire. Moreover, Hydroxide Catalysis Bonding (HCB) and detachable indium bonding will be used between the mirror and the

ear, and between the ear and the fiber head, respectively. In designing this system, we need to know the mechanical loss, the heat conductivity and the strength of each part of the sapphire suspension system. These topics are the main parts of this thesis. The thermal noise is smaller when the mechanical loss is smaller. The thermal resistance should be small otherwise the mirror can not be cooled. In order to support the 23kg sapphire mirror, the strength must be enough large.

Mechanical loss of fibers, HCB and indium bonding at low temperatures is investigated. Our measured lowest mechanical loss is 1.1×10^{-7} which is better than the required value of 2×10^{-7}. The author and colleagues also measured the mechanical loss of indium bonding and HCB. We bonded two sapphire cylinders by each bonding technique and measured the mechanical dissipation of these sapphire cylinders. In the result the measured loss of the indium bonding was 3.1×10^{-3}, which is lower than the requirement value 1.5×10^{-2}. The measured HCB mechanical loss was below 1.0 at 20 K, which is also smaller than the requirement value of 1.0. Therefore, all of the measured mechanical losses satisfied the requirements.

We also measured the heat extraction by the fiber, indium bonding and HCB. We measured thermal conductivity of sapphire fibers with nail heads and found that the values are between 5500 W/m/K and 6500 W/m/K and larger than the requirement, 5000 W/m/K. We also measured the thermal resistance of the bonded sapphire samples to determine if the bonding had significant thermal resistance at low temperatures. In the result we found the bondings will not influence the heat extraction from the mirror. So every component also satisfied the requirement in terms of the heat extraction.

Strength test of fibers had been done by our collaborators. According to the results, all of the fibers could hold a mass at least 6 times heavier than the case of KAGRA. In our laboratory, we performed strength tests for the bonding technique, especially for HCB, which will hold the mirror mass. Since the cryogenic suspension is thought to experience 20 thermal cycles in 10 years at most, we did a strength test at liquid helium temperature after 10 and 20 thermal cycles for the bonded samples by HCB. Then all of the samples, including samples after 20 thermal cycles had higher strength than the required value 1MPa. Because the indium bonding surfaces are not designed to hold any masses, the strength test for this bonding is not necessary.

Therefore, all of the components of the sapphire suspension system in concern were studied and satisfied the requirements at last.

Another important issue is the vibration noise from the cooling system. In order to estimate the influence, we measured the vibration of the radiation shield of KAGRA cryostat at cryogenic temperatures for the design of cryogenic payload. This vibration could shake the mirrors. Two cryogenic accelerometers were developed. (One of them is developed by collaborators at the Rome university.) We measured the vibration of the cooled radiation shield during a cooling test of the KAGRA cryostat in Toshiba Keihin Product Operations, Yokohama. We investigated how the shield vibration is different from the ground motion. Moreover, we also checked how the operation of cryocooler changes the vibration spectrum. We evaluated the radiation shield vibration at the KAGRA site, of which seismic motion is two order of magnitude lower than that around Toshiba. Then we calculated the displacement noise because of this radiation shield vibration through the heat links and the cryogenic suspension system. We found this displacement noise can exceed the design sensitivity of KAGRA. Accordingly, we proposed an additional vibration attenuation system for the vibration of the cooling system. This system can suppress the displacement noise below the design sensitivity of KAGRA.

As a result, we can construct a reliable cryogenic sapphire suspension using these components and techniques, and also the vibration due to the cooling systems will not make a significant noise.

KAGRA will be the first km-scale cryogenic telescope using the cryogenic mirror suspension systems, which will be necessary for future ground-based telescopes including the Einstein Telescope: a next generation gravitational wave telescope which will have cryogenic mirrors and locate in the underground. Cryogenic type interferometers have a potential that allows us to achieve a much higher sensitivity, which can observe more gravitational wave events and make new discoveries in physics and astronomy. The study in this thesis about the cryogenic suspension is a significant milestone for the future gravitational wave telescopes and also for a new gravitational wave astronomy.

Contents

Chapter 1

Introduction

Gravitational wave is a propagation ripple of space-time at the speed of light, predicted by Albert Einstein around a century ago [1]. Since the gravitational wave has extremely weak interaction against material, the permeability is very high. This is why people are expecting using this gravitational wave to observe the universe. Several decades ago, Hulse and Taylor showed the existence of the gravitational wave indirectly by the observation of the binary pulsar PR1913+16 [2]. Their observational result of the change in the revolution period accords well with expectation from the general theory of relativity. Nevertheless, the gravitational wave has not been observed directly even after a century from Einstein's prediction.

Many groups in the world are developing gravitational wave telescopes to observe the faint ripples of space-time. There are mainly four projects developing large laser interferometer gravitational wave telescopes, which are the most common type. They are Advanced LIGO[3], Advanced VIRGO[4], [5], GEO-HF[6] and KAGRA[7], [8]. These telescopes are under upgrade or being built currently. These telescopes are so called the second generation gravitational wave telescopes compared to the first generation telescopes like TAMA300[9], GEO[10], VIRGO[11] and the LIGO interferometer[12]. The second generation telescopes have about one order better sensitivity than what the first generation telescopes have in terms of strain: the observable volume becomes 1000 times lager. In addition, KAGRA being constructed under the ground for low seismic vibration and will use cooled mirrors to suppress the thermal noises. These two specific features are the first challenges for the km-scale interferometers. These techniques will also be used in the third generation telescope like the Einstein Telescope (ET)[13], which will have one order better sensitivity than what the second generation telescopes have. This is why KAGRA is also called 2.5 generation.

In order to measure an extremely small distance change between mirrors, any displacement noises should not be larger than gravitational wave signals. In order to make mirrors in an interferometric detector free mass, mirrors of KAGRA will be suspended in a manner similar to other gravitational wave telescopes. The main mirror of KAGRA will be suspended by four sapphire fibers, called a sapphire suspension system. This sapphire suspension system is included in the cryogenic suspension system. This cryogenic suspension system will be cooled down by cryocoolers through metal heat links as a heat path at low temperatures.

There are two issues about the cryogenic suspension system reported in this thesis.

The first one is the vibration noise from the cooling system. An increase of the vibration from the cooling system was observed in CLIO [14], [15] which is a 100 m cryogenic interferometer in 2006 [16]. After the experience in CLIO, the cryostat for KAGRA was designed to be as rigid as possible. To check the case of KAGRA, a vibration measurement of the KAGRA cryostat was performed.

The other one is the design of the cryogenic sapphire suspension system. The main mirror made of sapphire will be suspended by four sapphire fibers[1] in the cryogenic sapphire suspension system. It is difficult to use two sapphire fibers which have “U” shape to suspend the mirror because the fibers which should have 1.6 mm diameter to extract heat can not be bent to fit the curvature of the mirror perfectly. To construct this sapphire cryogenic system, two kinds of bonding techniques will be used. For designing this system what have to be considered is the mechanical loss which is linked to the thermal noise, the thermal conductivity and the strength of each component.

Mechanical loss measurement

The suspension thermal noise depends on the temperature and the mechanical loss of each parts of the sapphire suspension system. In order to estimate the thermal noise, measurements of the mechanical losses at low temperatures are necessary.

Mechanical loss measurements of a sapphire cylinder shape fiber, whose diameter is 0.25 mm, were performed by T. Uchiyama et al in 2000 [17]. The result was acceptable for KAGRA. But after 15 years from then, the design has to be changed because many more realistic parameters had been obtained including the absorption of the mirror, thermal conductivity of the fiber. Given a preliminary estimation of the thermal conductivity and, consequently, of the required thickness of the four suspension fibers made of sapphire, providing a figure of 1.6 mm diameter by 300 mm length. Therefore a new measurement of the mechanical loss, adopting the realistic shape and feasible clamping strategy is necessary. In this thesis the mechanical loss measurements of new fibers with heads are reported.

In order to estimate the required values of the mechanical losses, Levin’s method was used [18]. This is also the first estimation of the thermal noise for a suspended mirror system by this method.

The measurements of mechanical loss at low temperatures in bonded sapphire elements have never been reported until this thesis. The author and colleagues measured the mechanical loss at low temperatures through Hydroxide Catalysis Bonding (HCB) and indium bonding, which are the best candidates for bonding mirror suspension parts in KAGRA suspensions.

Thermal conductivity

Because the mirror and its coating absorb the power of the laser during the interferometer operating, in order to keep the temperature of the mirror at 20 K, the sapphire suspension

---

[1] The number of the fibers should not be lager because the violin mode of the fiber can split up into many peaks in the observation frequency region of KAGRA.

system should transfer the absorbed heat to the upper stage of the pendulum system. Thus, thermal conductivity of the fiber and the bonding surfaces should be known.

Thermal conductivity measurements of sapphire cylindrical fibers, namely without any head at the terminals were measured by T. Uchiyama et al and T. Tomaru et al [19] [81]. What they measured were the fibers that had several hundred μm in diameter without any heads. As mentioned above, the most reasonable shape of the fibers adopted for KAGRA is 1.6 mm diameter by 300 mm length, terminated with bulky heads on both the ends, designed to be bonded. Since the surface component of the thermal conductivity plays a role in the overall thermal conductivity of a sample, several measurements on 1.6 mm diameter samples have been performed and discussed in the context of this thesis. The thermal conductivity measurements of the shaped fibers are reported in this thesis. Cryogenics compliant bonding techniques experiments were reported in a previous study for the HCB by T. Suzuki et al, which shows a thermal conductivity measurement of a bonded sapphire sample by NGK Insulators LTD and bonded by a research group in Stanford University [20]. The samples studied in this thesis have been produced by Impex [53] and bonded by ourself through a collaboration with a research group in Glasgow that has optimized HCB for sapphire. In the case of the indium bonding, there are not any previous studies at low temperatures for sapphire block. This is the first study fully dedicated to the implementation of such techniques for assembling a cryogenic sapphire suspension.

Strength

In order to suspend the 23 kg mirror, sapphire fibers and HCB should have enough strength. The strength test was performed for the sapphire fibers which will be used in Glasgow by collaborators in the Glasgow and Roma groups. On the other hand, a strength test for HCB has been reported by T. Suzuki in their paper [20]. Their strength test was performed at room temperature and the sample had no experience of low temperatures. The strength test of HCB samples which had different crystal axis on the bonding surface was performed by Glasgow collaborators in Japan. These samples had no thermal cycle experiences. Because the KAGRA sapphire suspension can experience several thermal cycles, the strength of the bonded sample at low temperatures after thermal cycles was measured and reported in this thesis.

Given the introduction, provided in chapter 1, the contents of this thesis are the followings. Chapter 2 is dedicated to gravitational waves and to the main methods to detect them. Gravitational wave detectors, including KAGRA, are also introduced in this chapter. An outline of the cryogenic suspension of KAGRA is described in the chapter 3. The components in the cryogenic suspension of KAGRA are also explained in the chapter 3. The requirements of mechanical loss, thermal conductivity and strength of the mirror suspension of KAGRA are presented and discussed in chapter 4. The mechanical loss measurements of the sapphire fibers and bonds are reported in chapter 5. The measurements of thermal conductivity of fibers and bonds are reported in chapter 6. The results of strength tests for HCB and indium bonding are shown in the chapter

7. Then the vibration measurement of the cryostat and the estimated impact on the KAGRA are shown in chapter 8. Chapter 9 summarizes the results of the experiments for the sapphire suspension and the vibration measurement as well as discussions and future works. The conclusions of this thesis are in chapter 10.

Chapter 2

Gravitational waves and its detection

2.1 Gravitational waves

In this section, gravitational waves are introduced, starting from the General theory of Relativity [1]. Then the main sources of the gravitational wave are briefly discussed.

2.1.1 Gravitational waves

The thesis of the existence of gravitational waves is derived from the Einstein equation for space-time in vacuum and under the assumption of the weak gravitational field approximation (Lorentz background).

Einstein equation

In the General theory of Relativity, the space-time distance between two close points, ds, is defined by the square root of the following expression:

$$ds^2 = g_{\mu\nu} dx^\mu dx^\nu, \tag{2.1}$$

where μ, ν are $0, 1, 2, 3$ respectively, and dx^μ, dx^ν are the infinitesimal components along the four coordinates and $g_{\mu\nu}$ is called metric tensor and is used to describe the space-time curvature. According to the theory, the energy and the mass present in the space-time deform geometrically the space-time through the Einstein equation:

$$G_{\mu\nu} \equiv R_{\mu\nu} - \frac{1}{2} g_{\mu\nu} R = \frac{8\pi G}{c^4} T_{\mu\nu}, \tag{2.2}$$

where $G_{\mu\nu}$ is called Einstein tensor, $T_{\mu\nu}$ is the energy momentum tensor, c is the speed of light, and G is the gravitational constant. $R_{\mu\nu}$ is the Ricci and R is, finally, the scalar curvature. The differential relationships between the metric tensor and the curvature can be described by tensor components, $\Gamma^\alpha_{\beta\gamma}$, the Cristoffel symbols, as:

$$\begin{aligned}
\Gamma^\alpha{}_{\beta\gamma} &= \frac{1}{2} g^{\alpha\mu} \left(g_{\mu\beta,\gamma} + g_{\mu\gamma,\beta} - g_{\beta\gamma,\mu} \right) && (2.3)\\
R^\mu{}_{\alpha\beta\gamma} &= \Gamma^\mu{}_{\alpha\gamma,\beta} - \Gamma^\mu{}_{\alpha\beta,\gamma} + \Gamma^\mu{}_{\lambda\beta} \Gamma^\lambda{}_{\alpha\gamma} - \Gamma^\mu{}_{\lambda\gamma} \Gamma^\lambda{}_{\alpha\beta} && (2.4)\\
R_{\alpha\beta} &= R^\mu{}_{\alpha\mu\beta} && (2.5)\\
R &= R^\mu{}_\mu && (2.6)
\end{aligned}$$

Linearized Einstein equation

When there is no mass and energy in the space-time, the metric tensor $g_{\mu\nu}$ is the same as the Minkowski metric $\eta_{\mu\nu}$,

$$g_{\mu\nu} = \eta_{\mu\nu} = \begin{pmatrix} -1 & 0 & 0 & 0 \\ 0 & 1 & 0 & 0 \\ 0 & 0 & 1 & 0 \\ 0 & 0 & 0 & 1 \end{pmatrix} \tag{2.7}$$

In the case of a weak gravitational field, a perturbation $h_{\mu\nu}(|h_{\mu\nu}| \ll 1)$ can be added to the Minkowski metric.

$$g_{\mu\nu} = \eta_{\mu\nu} + h_{\mu\nu} \tag{2.8}$$

Now $\eta_{\mu\nu}$ and $\eta^{\mu\nu}$ can lower or raise the index as follows:

$$\begin{aligned} h^{\mu}{}_{\nu} &= \eta^{\mu\alpha} h_{\alpha\nu} && (2.9) \\ h_{\mu}{}^{\nu} &= \eta_{\mu\alpha} h^{\alpha\nu} && (2.10) \end{aligned}$$

Here, the Einstein equation is solved under this weak gravitation filed approximation.

Let's define a tensor named trace reverse tensor $\bar{h}_{\mu\nu}$:

$$\begin{aligned} \bar{h}_{\mu\nu} &\equiv h_{\mu\nu} - \frac{1}{2}\eta_{\mu\nu} h && (2.11) \\ h &\equiv h^{\alpha}{}_{\alpha}, && (2.12) \end{aligned}$$

then $h_{\mu\nu}$ can be written as:

$$h_{\mu\nu} = \bar{h}_{\mu\nu} + \frac{1}{2}\eta_{\mu\nu} h. \tag{2.13}$$

Christoffel symbols $\Gamma^{\alpha}{}_{\beta\gamma}$ and the Einstein tensor $G_{\mu\nu}$ are rewritten as

$$\begin{aligned} \Gamma^{\alpha}{}_{\beta\gamma} &= \frac{1}{2}\left(\bar{h}^{\alpha}{}_{\beta,\gamma} + \bar{h}^{\alpha}{}_{\gamma,\beta} - \bar{h}_{\beta\gamma}{}^{,\alpha}\right) && (2.14) \\ G_{\mu\nu} &= -\frac{1}{2}\left(\bar{h}_{\mu\nu,\alpha}{}^{,\alpha} + \eta_{\mu\nu}\bar{h}_{\alpha\beta}{}^{,\alpha\beta} - \bar{h}_{\mu\alpha,\nu}{}^{,\alpha} - \bar{h}_{\nu\alpha,\mu}{}^{,\alpha}\right). && (2.15) \end{aligned}$$

Here $\eta_{\mu\nu,\alpha} = 0$ is used. Now let's use the "Lorentz gauge", defined as:

$$\bar{h}^{\mu\nu}{}_{,\nu} = 0. \tag{2.16}$$

Then a simpler expression of Eq.(2.2) can be derived:

$$\Box \bar{h}_{\mu\nu} = -\frac{16\pi G}{c^4} T_{\mu\nu}. \tag{2.17}$$

This is the Linearized Einstein equation with a weak gravitational field.

Gravitational waves

The Einstein equation in vacuum is

$$
\begin{aligned}
\Box \bar{h}_{\mu\nu} &= 0 && (2.18)\\
\Box &\equiv -\frac{\partial^2}{c^2 \partial t^2} + \Delta, && (2.19)
\end{aligned}
$$

where $\Box$ is called the d′Alembertian operator. The plane wave solution of this wave equation is

$$
\bar{h}_{\mu\nu} = A_{\mu\nu} e^{i k_\alpha x^\alpha}, \tag{2.20}
$$

where $A_{\mu\nu}$ is a symmetric 4×4 matrix. The component of this matrix and the wave number vector k_α are derived from the wave function with Lorentz gauge. The condition can be written as follows.

$$
\begin{aligned}
A^{\mu\nu} k_\alpha &= 0 && (2.21)\\
k_\alpha k^\alpha &= 0 && (2.22)
\end{aligned}
$$

These equations imply that the gravitational wave is transverse wave and propagates at the speed of light. Here a gravitational wave which has an angular frequency $\omega = ck$ is assumed to propagate along the z axis, then

$$
\begin{aligned}
k_\alpha &= (-k, 0, 0, k) && (2.23)\\
\bar{h}_{\mu\nu} &= A_{\mu\nu} e^{ik(ct-z)}. && (2.24)
\end{aligned}
$$

Even if the Lorentz gauge was chosen, $A_{\mu\nu}$ is not unique. Another gauge called Transverse Traceless gauge (TT gauge) can be applied to simplify the components of $A_{\mu\nu}$.

$$
\begin{aligned}
A^\alpha{}_\alpha &= 0 && (2.25)\\
A_{\mu\nu} U^\nu &= 0, && (2.26)
\end{aligned}
$$

where U^ν is an arbitrary constant time like unit vector. Under these gauges, a plane wave propagating along z axis can be described like the followings:

$$
\begin{aligned}
k_\alpha &= \left(\omega, 0, 0, \frac{\omega}{c}\right) && (2.27)\\
\bar{h}_{\mu\nu} &= A_{\mu\nu} e^{ik(ct-z)} && (2.28)\\
A_{\mu\nu} &= \begin{pmatrix} 0 & 0 & 0 & 0 \\ 0 & \bar{h}_+ & \bar{h}_\times & 0 \\ 0 & \bar{h}_\times & -\bar{h}_+ & 0 \\ 0 & 0 & 0 & 0 \end{pmatrix} && (2.29)
\end{aligned}
$$

where $\bar{h}_+, \bar{h}_\times$ are the amplitudes of the independent polarization of the gravitational wave. The mode of $\bar{h}_+$ is called “plus mode” and the mode of $\bar{h}_\times$ is called “cross mode”.

Action on free particles from the gravitational wave

Free particles in a gravity field conform to the geodesic equation:

$$\frac{\mathrm{d}}{\mathrm{d}\tau}U^{\mu} + \Gamma^{\mu}{}_{\alpha\beta}U^{\alpha}U^{\beta} = 0. \tag{2.30}$$

This equation is called the geodesic equation. In this equation τ is the proper time of a particle and U^{α} is the four-velocity described as

$$U^{\alpha} = \frac{\mathrm{d}x^{\alpha}}{\mathrm{d}\tau} \tag{2.31}$$

First, let's assume one particle in the space and check the action due to the gravitational wave. If the particle is at rest at the origin point at the beginning,

$$U^{\mu} = (1, 0, 0, 0). \tag{2.32}$$

Putting Eq.(2.32) into Eq.(2.30), then

$$\begin{aligned} \frac{d}{d\tau}U^{\mu} &= -\Gamma^{\mu}{}_{00} && (2.33) \\ &= -\frac{1}{2}\eta^{\mu\nu}\left(\bar{h}_{\nu 0,0} + \bar{h}_{0\nu,0} - \bar{h}_{00,\nu}\right) && (2.34) \\ &= 0, && (2.35) \end{aligned}$$

which means that in the TT gauge this particle has no acceleration.

Secondly, let's assume two particles encounter the gravitational wave. Originally one of the particles is at the origin $(0, 0, 0)$ and the other one is at a point $(\epsilon, 0, 0)$, therefore the proper distance between the particles Δl is

$$\begin{aligned} \Delta l &= \int \left|ds^2\right|^{\frac{1}{2}} = \int_0^{\epsilon} \sqrt{g_{11}}dx && (2.36) \\ &= \sqrt{g_{11}}\epsilon && (2.37) \\ &\simeq \left(1 + \frac{1}{2}\bar{h}_{11}\right)\epsilon. && (2.38) \end{aligned}$$

This equation shows that the proper distance between two particles changes because of the gravitational wave. The distance change is proportional to the original distance ϵ.

And finally, we consider two particles separated by a distance $\epsilon^j = (\epsilon^x, \epsilon^y, \epsilon^z)$ and with each other and focus on the distance change because of the gravitational wave. If the gravitational wave vector is aligned along z axis, Δl can be written as

$$\begin{aligned} \Delta l^j &= \epsilon^j + \frac{1}{2}\bar{h}_{\mu\nu}\epsilon^j && (2.39) \\ \begin{pmatrix} \Delta l^x \\ \Delta l^y \end{pmatrix} &= \begin{pmatrix} \epsilon^x \\ \epsilon^y \end{pmatrix} + \frac{1}{2}e^{ik(ct-z)}\begin{pmatrix} \bar{h}_{+} & \bar{h}_{\times} \\ \bar{h}_{\times} & -\bar{h}_{+} \end{pmatrix}\begin{pmatrix} \epsilon^x \\ \epsilon^y \end{pmatrix} && (2.40) \\ &= \begin{pmatrix} \epsilon^x \\ \epsilon^y \end{pmatrix} + \frac{1}{2}e^{ik(ct-z)}\bar{h}_{+}\begin{pmatrix} \epsilon^x \\ -\epsilon^y \end{pmatrix} + \frac{1}{2}e^{ik(ct-z)}\bar{h}_{\times}\begin{pmatrix} \epsilon^x \\ \epsilon^y \end{pmatrix} && (2.41) \end{aligned}$$

This equitation shows distance change has two components, which means the gravitational wave have two polarizations. One of them has amplitude $\bar{h}_+$, whose x components and y components change in reverse phase. The other has amplitude $\bar{h}_\times$, whose x components and y components change in phase. Figure 2.1 shows the distance changes between free particles due to gravitational waves with wave vector perpendicular to the drawing.

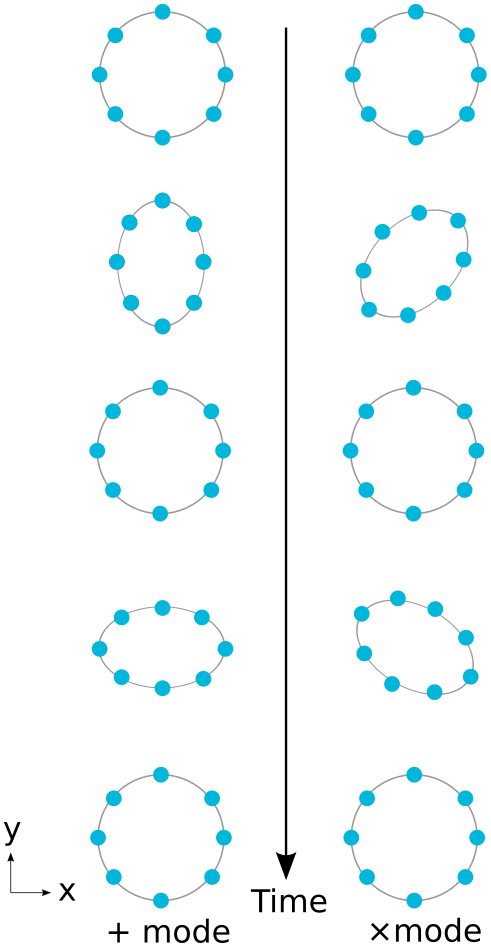

Figure 2.1: Polarization of gravitational wave. The blue points represent a circular distribution of free-falling masses. The effect of gravitational waves impinging perpendicularly to the figure causes a relative change of distances according to two polarization states. The fact that the two polarizations are oriented at 45 degrees is related to the tensorial nature of the field, differently with respect to electromagnetic waves.

2.1.2 Generation and sources of gravitational waves

Generation of gravitational waves

The solution of the linearized Einstein Eq.(2.17) is

$$\bar{h}_{\mu\nu}(t, \boldsymbol{r}) = \frac{4G}{c^4} \int \frac{T_{\mu\nu}(t - \frac{R}{c}, \boldsymbol{r'})}{R} d^3x', \tag{2.42}$$

there $\boldsymbol{r}$ is the position of observer, $\boldsymbol{r'}$ is the wave source position and $R = |\boldsymbol{r} - \boldsymbol{r'}|$ is the distance between the observer and the source. Here the size of gravitational wave sources is assumed to be smaller than R and wavelength of gravitational waves. This equation can be approximated as the following.

$$\begin{aligned} \bar{h}_{\mu\nu}(t, \boldsymbol{r}) &\simeq \frac{4G}{c^4 r} \int T_{\mu\nu} \left(t - \frac{r}{c}, \boldsymbol{r'} \right) d^3x' & (2.43) \\ &\simeq \frac{2G}{c^4 r} \frac{d^2}{dt^2} \int \rho' \left(t - \frac{r}{c}, x' \right) x'_i x'_j d^3x' & (2.44) \\ &= \frac{2G}{c^4 r} \frac{d^2}{dt^2} I_{ij} \left(t - \frac{r}{c} \right) & (2.45) \end{aligned}$$

Here $I_{i,j}$ can be written as the following (TT gauge).

$$I_{ij} = \int \rho'(t, x') \left(x'_i x'_j - \frac{1}{3} \delta^i_j x'^i x'^j \right) d^3x' \tag{2.46}$$

This I_{ij} is a quadrupole moment. Thus the gravitational wave is caused by a change of the quadrupole moment. The plus mode and cross mode gravitational wave can be written as the following.

$$\begin{aligned} \bar{h}_+(t) &= \frac{2G}{c^4 r} \frac{d^2}{dt^2} \frac{I_{11}\left(t - \frac{r}{c}\right) - I_{22}\left(t - \frac{r}{c}\right)}{2} & (2.47) \\ \bar{h}_\times(t) &= -\frac{2G}{c^4 r} \frac{d^2}{dt^2} I_{12} \left(t - \frac{r}{c} \right) & (2.48) \end{aligned}$$

As with the above, the amplitude of the gravitational wave from distance r is

$$\bar{h} \simeq \frac{2G}{c^4 r} \frac{d^2 I}{dt^2}. \tag{2.49}$$

The amplitude of h is extremely small. For example, this value is about 10^{-22} in the case of a neutron star - neutron star binary coalescence at 20 Mpc far from an observer.

Source of gravitational waves

The main sources of the gravitational waves which will be detected in the near future are astronomical phenomenon because the gravitational waves we can generate in our laboratory are too small to observe [21]. Potential astronomical sources are described in the followings.

Pulsars

Pulsars are considered to be rotating neutron stars, which emit electromagnetic waves. If the neutron star is not a sphere shape, but a triaxial ellipsoid shape, gravitational waves can be emitted as clockwork waves. In addition, integration of the signal for a long time(∼month or year) can make the signal to noise ratio higher value. The amplitude of the gravitational waves from a pulsar is the following.

$$\bar{h} = \frac{2\pi^2 G}{c^4}\frac{I_{zz} f_0^2}{r}\epsilon \tag{2.50}$$

$$\epsilon = \frac{I_{xx} - I_{yy}}{I_{zz}} \tag{2.51}$$

there f_0 is the frequency of the gravitational wave, r is the distance between observer and the pulsar and I_{ij} is the inertia tensor of the neutron star (z axis faces the observer) [22]. Data analysis of the current laser interferometer gravitational wave telescope for the pulsar are done and reported [22, 23]. Even though they could not observe the gravitational wave, the upper limits of the gravitational wave amplitude were obtained.

Binaries

Binary systems of neutron stars(NSs) and black holes(BHs) are one of the main targets of the ground based interferometer gravitational wave telescope. According to Lada's paper in 2006 [24], one-thirds of all primary stars in the Galactic disk have accompanying stars. Some small part of them are NS/NS, NS/BH or BH/BH.

In this part, mergers of neutron star binaries are focused. After a merger, the binary becomes a black hole immediately or a heavier neutron star which will be a black hole after a while because of the energy loss by gravitational waves and neutrinos, which depends on the equation of state and mass of the neutron stars in binary. The binary merger is divided into three steps: inspiral stage, merger stage and ring down stage. Information of the masses can be estimated from the wave forms of inspiral stage and information of radiuses is seen in the merger stage wave forms. This information gives a constrain on the equation of state of dense material as atomic nucleus. Spectra or time domain waveforms of the gravitational waves from the ring down stage can give us information on the neutron star and the black hole. For instance, there is a model which indicates that hyperonic matter appearing in the neutron star core dominates the contraction. In this model, because the pressure of the hyperonic matter is less than that of normal matter of proton and neutron, the contraction time is shorter than that of normal matter. Then the spectrum of the hyperonic matter model has broad peaks compared to the sharp peaks in the spectrum of the normal matter model [25]. Therefore, observation of the gravitational waves can give a judgment on it.

The second generation telescopes are expected to observe the last several minutes of the coalescence and the detection rate is estimated to be one event per year ∼ three events per day [26].

Supernovae

Supernovae is also considered to emit gravitational waves as one of the burst sources. The maximum amplitude of the gravitational wave from a supernova at a distance of 10 kpc is thought to be about 10^{-21}. And the frequency is estimated to be from several hundred Hz to several kHz [27].

Cosmic gravitational wave background

Very low frequency gravitational waves named cosmic gravitational wave background from the early universe are expected to be observed by space based telescopes like DECIGO in the future. The estimated spectrum is nearly white in units of energy [28, 29]. Because gravitational waves have very low interaction, the signal emitted at $10^{-30}\,\mathrm{s}$ after the beginning of the Universe can be observed [30].

2.2 Detection principle

There are several kinds of detectors such as a resonance detector [31, 32], an atomic interferometer [33], a torsion-bar antenna [34] and a laser interferometer. In this section, the detection principle of the laser interferometer, which is the most common technique for gravitational wave telescopes currently is described.

In order to detect gravitational waves, we can measure the proper distance between two test masses. Because the distance change via the gravitational wave is extremely small, laser interferometer is used for the detectors. A simple Michelson interferometer is described here.

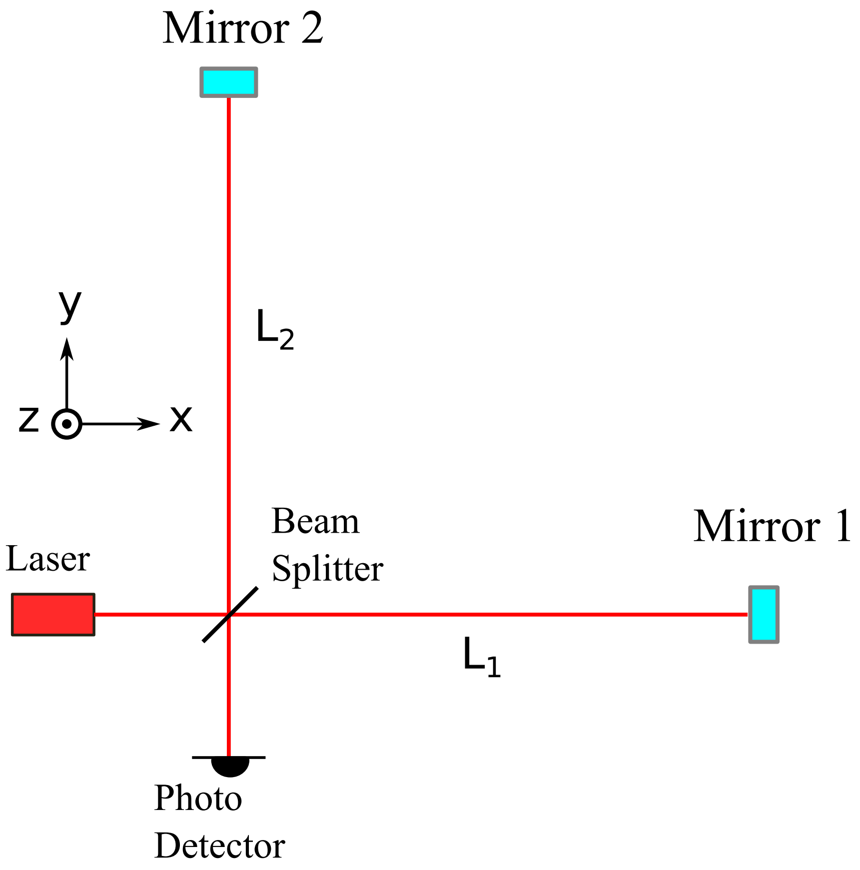

Figure 2.2: Schematic view of a Michelson interferometer. The laser beam from the laser source is split by the beam splitter and goes toward the main mirrors through the “arm” which have the length L_1, L_2. Then reflected laser beam by the mirrors interferes with each other at the beam splitter. The photo detector monitors the power of the laser at the anti-symmetric port.

Figure 2.2 is a schematic view of a Michelson interferometer. A laser light from the laser source is divided by a beam splitter in the center, then reflected by the mirrors called end mirrors and combined at the beam splitter again. The part between the beam splitter and the end mirror is called an arm. A photo detector detects the intensity of the combined laser at the anti-symmetric port. On the other hand, the position where the laser beam is emitted, is called the symmetric port.

The electrical field E_{in} from the laser can be written

$$E_{\mathrm{in}} = E_0 e^{i\Omega t}. \tag{2.52}$$

Here Ω is the angular frequency of the laser. From E_{in}, the electrical fields E_{out1} and E_{out2} at the beam splitter reflected by the mirrors 1 and 2 are able to be written as

$$E_{\mathrm{out1}} = \frac{1}{2} E_0 e^{i(\Omega t - \phi_1)} \tag{2.53}$$

$$\text{and} \quad E_{\mathrm{out2}} = -\frac{1}{2} E_0 e^{i(\Omega t - \phi_2)}. \tag{2.54}$$

The photo detector detects the square of the sum of them:

$$\begin{aligned} P_{\text{out}} &= |E_{\text{out1}} + E_{\text{out2}}|^2 && (2.55) \\ &= \frac{1}{2} P_{\text{in}} (1 - \cos\phi_-). && (2.56) \end{aligned}$$

Here,

$$\begin{aligned} P_{\text{in}} &\equiv E_0^2 && (2.57) \\ \text{and} \quad \phi_- &\equiv \phi_1 - \phi_2. && (2.58) \end{aligned}$$

As above, the phase difference between the two paths can be estimated by observing the output of the photo detector at the anti-symmetric port.

Let's see the output of this interferometer when gravitational waves come. A plus mode gravitational wave along z axis is assumed in the following. The gravitational wave $\bar{h}_{\mu\nu}$ can be written as

$$\bar{h}_{\mu\nu} = \begin{pmatrix} 0 & 0 & 0 & 0 \\ 0 & \bar{h}_+ & 0 & 0 \\ 0 & 0 & -\bar{h}_+ & 0 \\ 0 & 0 & 0 & 0 \end{pmatrix}. \qquad (2.59)$$

The proper distance ds can be written

$$ds^2 = -c^2 dt^2 + \left[1 + \bar{h}(t)\right] dx^2 + \left[1 - \bar{h}(t)\right] dy^2 + dz^2, \qquad (2.60)$$

where $\bar{h}(t)$ is the amplitude of the gravitational wave. In the case of Fig.2.2 , Eq.(2.59) can be

$$dx = \frac{1}{\sqrt{1 + \bar{h}(t)}} c dt \simeq \left[1 - \frac{1}{2}\bar{h}(t)\right] c dt \qquad (2.61)$$

because $\bar{h}(t) \ll 1$ and $ds^2 = 0$ in the case of light. Integration of Eq.(2.61) from the beam splitter to the mirror 1 and from the mirror 1 to the beam splitter gives:

$$\int_0^{2L_1} dx = c \int_{t-\delta t_1}^{t} \left[1 - \frac{1}{2}\bar{h}(t')\right] dt'. \qquad (2.62)$$

Here δt_1 is the round trip time between the beam splitter and the mirror 1, and written by

$$\begin{aligned} \delta t_1 &= \frac{2L_1}{c} + \frac{1}{2} \int_{t-\delta t_1}^{t} \bar{h}(t') dt' && (2.63) \\ &\simeq \frac{2L_1}{c} + \frac{1}{2} \int_{t-\frac{2L_1}{c}}^{t} \bar{h}(t') dt'. && (2.64) \end{aligned}$$

Therefore ϕ_1 which is the phase change of the light during the L_1 pass is

$$\begin{aligned} \phi_1 &= \Omega \delta t_1 && (2.65) \\ &= \frac{2L_1\Omega}{c} + \frac{\Omega}{2} \int_{t-\frac{2L_1}{c}}^{t} \bar{h}(t') dt' && (2.66) \end{aligned}$$

It is the same calculation in the case of L_2 pass,

$$\begin{aligned}\phi_2 &= \Omega\delta t_2 & (2.67)\\ &= \frac{2L_2\Omega}{c} + \frac{\Omega}{2}\int_{t-\frac{2L_2}{c}}^{t} \bar{h}(t')dt'. & (2.68)\end{aligned}$$

So ϕ_- can be written like the following.

$$\begin{aligned}\phi_- &= \frac{2l_-\Omega}{c} + \delta\phi_{GW} & (2.69)\\ \delta\phi_{GW} &= \Omega\int_{t-\frac{2L}{c}}^{t} \bar{h}(t')dt', & (2.70)\end{aligned}$$

there $L_1 \simeq L_2 \equiv L, l_- \equiv L_1 - L_2$. The first term of Eq.(2.69) shows the constant phase difference due to the distance difference between L_1 and L_2. On the other hand, Eq.(2.70) $\delta\phi_{GW}$ is the phase difference caused by the gravitational wave. In order to describe clearer, the Fourier transform is adapted:

$$\begin{aligned}\bar{h}(t) &= \int_{-\infty}^{\infty} \bar{h}(\omega)e^{i\omega t}d\omega & (2.71)\\ \delta\phi_{\mathrm{GW}} &= \int_{-\infty}^{\infty} H_{\mathrm{MI}}(\omega)\bar{h}(\omega)e^{i\omega t}d\omega & (2.72)\\ H_{\mathrm{MI}}(\omega) &= \frac{2\Omega}{\omega}\sin\left(\frac{L\omega}{c}\right)e^{-i\frac{L\omega}{c}} & (2.73)\end{aligned}$$

This equation shows that larger L makes the signal larger at the low frequency band.

$$|H_{\mathrm{MI}}| = \frac{2\Omega L}{c} \quad (\omega \to 0) \tag{2.74}$$

But there is a maximum for $|H_{\mathrm{MI}}|$ at ω_0 when

$$L = \frac{\pi c}{2\omega_0}. \tag{2.75}$$

In the case of 1 kHz, the arm length L is 75 km.

To make a Michelson interferometer which has such long arms on the ground is difficult. Therefore, in order to extend the effective arm length, delay line and Fabry-Perot Michelson interferometer have been proposed. Schematic views of these interferometers are shown in Figs.2.3, 2.4.

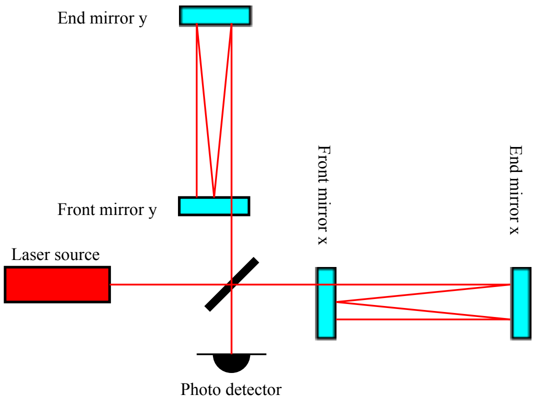

Figure 2.3: Delay line Michelson interferometer. The laser light is reflected by the mirrors many times at different points and goes back to the beam splitter.

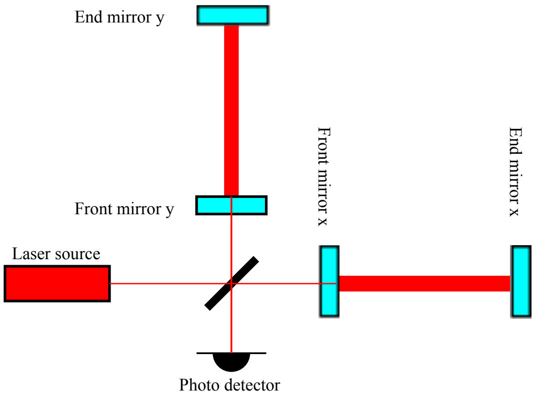

Figure 2.4: Fabry-Perot Michelson interferometer. The laser light resonates in the arm, which makes the signal sensitive to the arm length change.

In these interferometers there are two mirrors called front mirrors in addition to the end mirrors. In the case of the delay line, a laser light in the arm hits the front mirror and the end mirror many times at different points in order to make a longer optical path length. One of the disadvantages of the delay line is that big mirrors are needed because hundreds of laser points should be on the mirror. Another disadvantage is the scattered light from the several hundreds laser spots. On the other hand, Fabry-Perot has a laser cavity between a front mirror and an end mirror, which can extend the arm length with one spot on a mirror. Photons stay in Fabry-Perot cavities for “longer” time. Thus, the signal of gravitational wave is enhanced effectively.

2.3 Gravitational wave telescopes

In the world, several groups are developing, upgrading, constructing or operating their gravitational wave telescopes. Gravitational wave telescopes which are laser interferometer type are described in this chapter. Laser interferometer telescopes can be categorized into two types: ground based laser interferometer and space laser interferometer. The most sensitive frequency band is different between these telescopes. Because telescopes in the space can have much longer arms compared to ground based telescopes, their plans are having long arms to detect low frequency gravitational wave which is difficult to be detected by ground based detectors because of the seismic noise. Low frequency gravitational waves are thought to come from massive source or large structure like BH-BH binaries or cosmic gravitational wave background. On the other hand, ground based laser telescopes focus on the frequency band around 100 Hz, which is the frequency band of such as NS-NS binary mergers.

2.3.1 Space laser interferometer

In the space, there are no seismic vibration and little newtonian noise because of the motion of the mass around the detector. Therefore, telescopes which have a good sensitivity at low frequency band can be achieved.

eLISA

eLISA stands for evolved Laser Interferometer Space Antenna, which is planned by the European Space Agency (ESA) [35]. This interferometer consists of three space crafts, which have a triangle shape. The distances between space crafts are 10^6 km and keep an equilateral triangle shape. Because of this extremely long arms the strain sensitivity is expected to be $\sim 5 \times 10^{-21}\,1/\sqrt{\mathrm{Hz}}$ at 10^{-2} Hz. At the low frequency band of eLISA will observe stochastic gravitational waves caused by many galactic compact binaries: such as white dwarf binaries, NS-NS binaries, BH-BH binaries. This statistical observation can give us important information to model important objects in astrophysics. Gravitational waves from massive black holes are also the main target of eLISA.

DECIGO

The Japanese DECi-Hertz Gravitational wave Observatory (DECIGO) is a planned telescope in the space which has the observation band around $0.1\,\mathrm{Hz} \sim 1\,\mathrm{Hz}$, which is a frequency band between eLISA and ground based telescopes [36]. One unit of DECIGO consists of three space crafts. The length of the arms is planned to be 1000 km in order to have a good sensitivity between 0.1 Hz and 1 Hz. In total four units will be put in the heliocentric orbit to have coincidence observation in order to cancel the noise and determine the direction of gravitational wave sources. The main targets of DECIGO are gravitational waves from compact binaries and inflation at the beginning of the Universe. Since the observation band is lower than the detector on the Earth, the NS-NS binaries can be observed at from several years before the merger. This gravitational wave is phase shifted by the cosmic expansion, therefore the cosmic expansion can be observed by gravitational waves not by red shift of light. The gravitational wave from the inflation is the main target for DECIGO. Observation of DECIGO is expected to eliminate some models and select suitable models.

DECIGO has many technics which have to be developed: such as a stabilized laser source in the space, formation flight, and drag free control. Several technics have to be tested by some projects before DECIGO. Currently, groups in several universities and institutes are developing the technics for DECIGO.

2.3.2 Ground based laser interferometer

In this subsection, large laser interferometer telescopes in the world are introduced after the description of the noise sources of ground based laser interferometer. Even though there are many noise sources, many advantages (e.g.: easier maintenance, improvement, and low cost) are there for the ground based telescope. Therefore, many ground based telescope teams are aiming at the first detection.

Noise source

Fundamental noise sources of advanced gravitational wave telescope like advanced LIGO, advanced VIRGO and KAGRA are mainly seismic noise, quantum noise and thermal noise. In the case of advanced VIRGO, gravity gradient noise will limit the sensitivity in a region of the frequency band.

In the case of ground based telescopes, seismic noise reduction is crucial. For example, a typical power spectrum of the seismic motion around the suburb $x_{\mathrm{seisS}}(f)$ is able to be approximated as

$$x_{\mathrm{seisS}} = \frac{10^{-7}}{f^2}\left[\frac{\mathrm{m}}{\sqrt{\mathrm{Hz}}}\right]. \tag{2.76}$$

In the case of a quieter place like Kamioka mine where KAGRA is being constructed, this vibration x_{seisK} can be smaller by 2 orders of magnitude.

$$x_{\mathrm{seisK}} = \frac{10^{-9}}{f^2}\left[\frac{\mathrm{m}}{\sqrt{\mathrm{Hz}}}\right]. \tag{2.77}$$

In order to suppress the influence of this vibration, multi suspensions are used to separate our main mirrors from the ground motion [37, 38, 39].

The quantum noise becomes important if a laser light is used to measure the distance change between test masses. This noise consists of two parts: one is radiation pressure noise, and the other one is shot noise. Because the number of photons per unit time gives the Poisson distribution, the signal-to-noise ratio of the phase noise is proportional to $\frac{1}{\sqrt{P}}$, where P is the power of the laser, which is called shot noise. On the other hand, radiation pressure noise which is the displacement fluctuation because of the fluctuation of the radiation pressure is proportional to $\sqrt{P}$. So the sum of these two noises cannot be lower than a limit so-called "Standard Quantum Limit" (SQL), which limits the laser interferometer sensitivity with a regular detection method. SQL can be written like the Eq.(2.78).

$$S_{\mathrm{SQL}}(f) = \frac{2\hbar}{m(2\pi f)^2}, \tag{2.78}$$

where S_{SQL} is the power spectrum, $\hbar$ is the reduced Planck's constant and m is the mass of the mirror.

At last, the thermal noise is the displacement vibration due to the thermal energy in each part of the suspension system especially close to the main mirror. There are three kinds of thermal noise depending on the source part: mirror thermal noise, mirror coating thermal noise and suspension thermal noise. At first, the displacement power spectrum of mirror thermal noise $S_{\mathrm{MTN}}(f)$ can be described as

$$S_{\mathrm{MTN}}(f) = \frac{2k_BT}{\pi^{\frac{3}{2}}f}\frac{1-\sigma^2}{w_0E}\phi_{\mathrm{sub}} \tag{2.79}$$

where k_B is the Boltzmann constant, T is the temperature, σ is the Poisson's ration, w_0 is the beam size ($1/e^2$ radius) on the mirror and E and ϕ_{sub} are the Young's modulus and mechanical loss of the mirror substrate respectively [40, 18]. In the case of KAGRA, the displacement power spectrum density $\sqrt{S_{\mathrm{MTN}}(f)}$ is written

$$\sqrt{S_{\mathrm{MTN}}(f)} = 4.8 \times 10^{-22} \frac{\mathrm{m}}{\sqrt{\mathrm{Hz}}} \left(\frac{3.5\mathrm{cm}}{w_0}\right)^{\frac{1}{2}} \left(\frac{4.6 \times 10^{11}\mathrm{Pa}}{E}\right)^{\frac{1}{2}}$$
$$\times \left(\frac{\phi_{\mathrm{sub}}}{4.0 \times 10^{-9}}\right)^{\frac{1}{2}} \left(\frac{T}{20\mathrm{K}}\right)^{\frac{1}{2}} \left(\frac{100\mathrm{Hz}}{f}\right)^{\frac{1}{2}} \left(\frac{1-\sigma^2}{1-0.25^2}\right)^{\frac{1}{2}}. \tag{2.80}$$

Second, the displacement power spectrum of coating thermal noise $S_{\mathrm{CTN}}(f)$ can be written as the Eq.(2.81) using $S_{\mathrm{MTN}}(f)$.

$$S_{\mathrm{CTN}}(f) = S_{\mathrm{MTN}}(f) \left(1 + \frac{2}{\sqrt{\pi}} \frac{1-2\sigma}{1-\sigma} \frac{\phi_{\mathrm{coat}}}{\phi_{\mathrm{sub}}} \frac{d_{\mathrm{coat}}}{w_0}\right), \tag{2.81}$$

where ϕ_{coat} and d_{coat} are mechanical loss and the thickness of the coating, respectively [41, 42]. KAGRA will use $\mathrm{SiO_2/Ta_2O_3}$ coating to make a reflectivity of 99.6% for the front mirrors and 99.9945% for the end mirrors [43]. In the same way as the mirror thermal noise, the coating thermal noise of KAGRA can be estimated as

$$\sqrt{S_{\mathrm{CTN}}(f)} = 1.6 \times 10^{-21} \frac{\mathrm{m}}{\sqrt{\mathrm{Hz}}} \left(\frac{100\mathrm{Hz}}{f}\right)^{\frac{1}{2}}, \tag{2.82}$$

where the mechanical loss of coating ϕ_{coat} is assumed to be 4.0×10^{-4}, the thickness of the coating d_{coat} is assumed to be 4.8μm and the other parameters are assumed as shown in Eq.(2.80) [44]. Detailed discussion about the suspension thermal noise will be given in the latter chapters.

Ground based large gravitational wave telescopes in the world

LIGO (the Laser Interferometer Gravitational-Wave Observatory) is a project in the United States of America. This project has three large interferometers. Two of them have 4 km arms located at Hanford and Livingston, the other one has 2 km arms, located at Hanford in parallel with the 4km arm interferometer. The distance between these two sites is about 3000 km. Since these two sites are far from each other, coincidence analysis reduces the false alarm ratio drastically. LIGO project is developing and constructing the advanced LIGO, which will have 10 times better strain sensitivity than the initial LIGO [3].

Nearby Pisa in Italy, there is a 3 km arm interferometer called VIRGO. This interferometer was developed by the Italy and France groups mainly. This interferometer is also being upgraded. The advanced VIRGO will have 10 times better strain sensitivity than the initial VIRGO [45].

At last, KAGRA is being developed and constructed in Japan. This will be a 3 km interferometer which is located underground to have a quiet seismic vibration and stable temperature fluctuation, and the main mirrors will be cooled down to 20 K to suppress the thermal noise. Details are described in the next subsection.

2.4 Large-scale Cryogenic Gravitational wave Telescope -KAGRA-

The Large-scale Cryogenic Gravitational wave Telescope in Japan named KAGRA is under construction at the Kamioka mine in Gifu prefecture. An image view of KAGRA is shown in Fig.2.5.

Figure 2.5: Image view of KAGRA in the Kamioka mine. KAGRA which has 3 km length arms is under construction in the Kamioka mine.

KAGRA is a Michelson interferometer which has 3 km arm Fabry-Perot cavities. There are two stages for KAGRA which is called initial KAGRA (iKAGRA) and baseline KAGRA (bKAGRA). The iKAGRA is scheduled to have an observation run at the end of 2015 in order to gather experience of a large interferometer with a simple configuration. In this stage the main mirrors are at room temperature. Moreover the power recycling and signal recycling technique will not be used. bKAGRA will start the science run in 2017. Cooled mirrors and recycling technics will be used in this stage to have the goal sensitivity.

The final configuration of KAGRA is shown in the Fig.2.6.

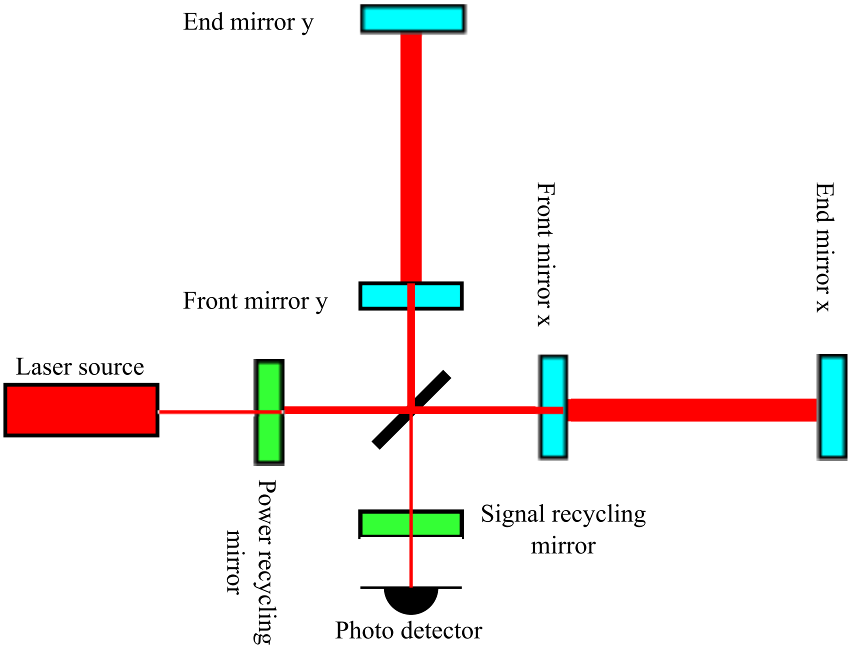

Figure 2.6: Simplified final configuration of KAGRA. All of the mirror in this figure will be suspended to suppress the seismic vibration. Blue mirrors are the cryogenic mirrors.

The blue mirrors in the figure will be cooled. The one of the green mirrors nearby the laser source is called a power recycling mirror. This mirror reflects the light back to the interferometer coherently with the incident light to effectively increase the laser power in the arm cavities. In the result, shot noise is suppressed. Signal recycling mirror nearby the photo detector reflects laser light which has the gravitational wave signal in order to enhance the amplitude of a gravitational wave signal. These mirrors are suspended to be a free mass in the observation frequency range of the gravitational waves and also to decrease the vibration coming from the ground. Cryogenic payload, which includes a sapphire mirror, will be suspended from the excellent vibration isolation system, type A Seismic Attenuation System (SAS). The total height of the suspension is $\sim$ 13m. Figure 2.7 shows the conceptual diagram.

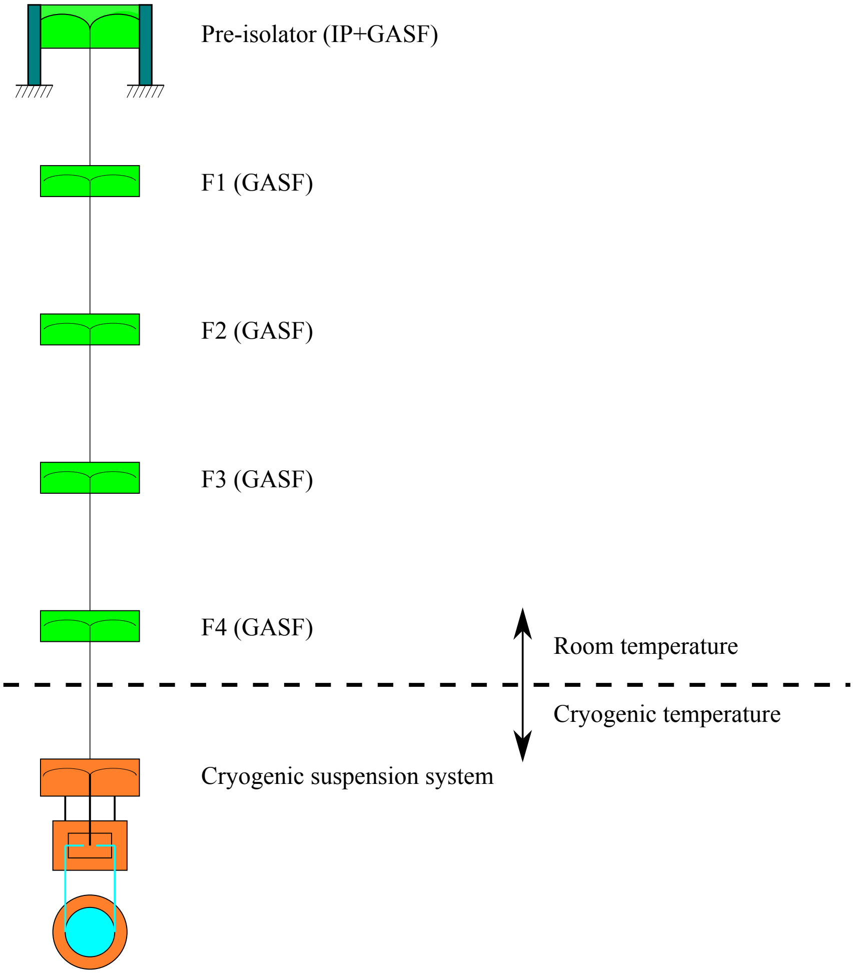

Figure 2.7: Seismic Attenuation System (SAS) for a main mirror and a cryogenic suspension system suspended below it. All of the components will be in the same vacuum system. The total length of this multi-suspension system will be $\sim 13\,m$.

Inverted pendulums (IPs) and Geometric Anti-Spring Filters (GASFs) are in the SAS to reduce the horizontal vibration and vertical vibration from the ground, respectively [46].

All of the mirrors in Fig.2.6 will be in the vacuum chamber. The pressure is $\sim 10^{-7}$Pa. The four main mirrors are in each cryostat which are made by Toshiba [47] to be cooled down to 20K in order to reduce the thermal noise. Cooling systems for the main mirrors are shown in the later chapters. Figures of the vacuum chamber and cryostat for the cooled main mirrors are shown in Figs.2.8 and 2.9. In order to make tall systems like SAS, KAGRA has the 2nd floor in the region of the front rooms and the end rooms.

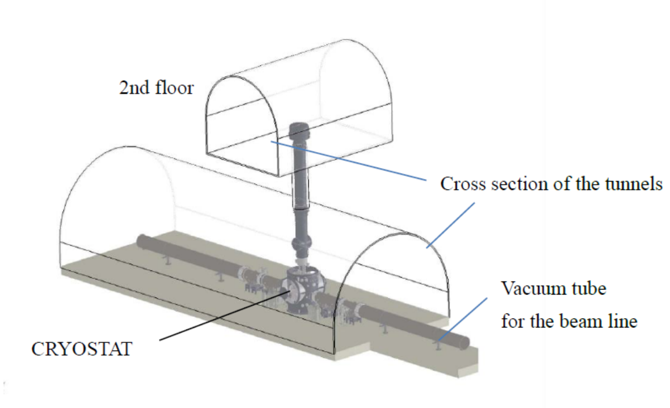

Figure 2.8: View of a vacuum chamber around the main mirror. Top of the suspension for the main mirror is fixed on the second floor. Vacuum tubes for the main beam are connected with the cryostat.

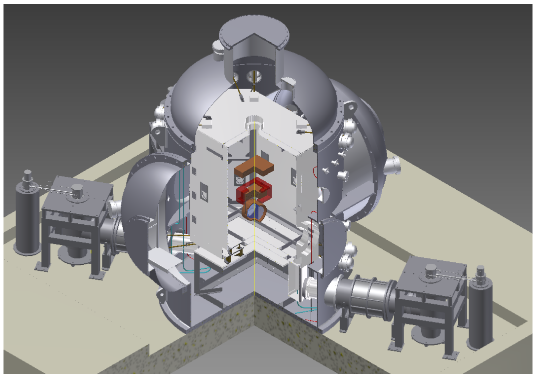

Figure 2.9: KAGRA cryostat for the main mirror. Four cryocoolers will be used to cool one cryostat including the system inside.

The KAGRA final sensitivity will be limited by the seismic vibration at very low frequencies and quantum noise at the most sensitive region. At the most sensitive frequency region, the coating thermal noise also will affect slightly. A realistic design sensitivity is shown in Fig.2.10.

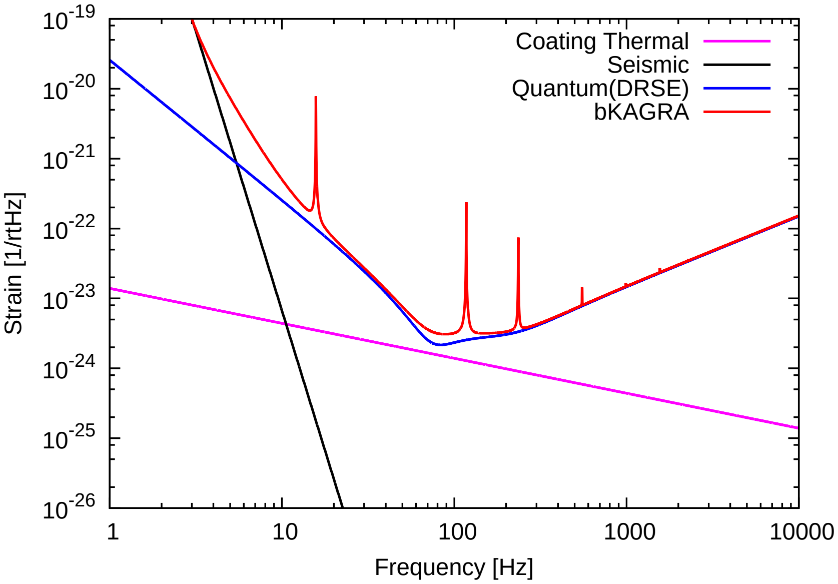

Figure 2.10: Design sensitivity of KAGRA. In this graph only the main noises are plotted. "bKAGRA" is a realistic bKAGRA design sensitivity including other noises, which is used in this thesis as the design sensitivity [75]. The suspension thermal noise or the displacement noise from the cooling system, which are described in this thesis should be below the "bKAGRA" curve in this graph.

The noise by the cryogenic payload should be smaller than this sensitivity, which is the main topic of this thesis. Two kinds of noise sources were investigated in this thesis. The first one is the suspension thermal noise. The second one is the vibration noise via the heat links from the cooling systems. The details are described in the next chapter.

Chapter 3

Outline of cryogenic suspension of KAGRA

The main mirror of KAGRA should be suspended in order to be a free mass for the gravitational waves and suppress the vibration from outside like seismic vibration and vibration via heat links. For keeping the stable operation of the main interferometer, it is necessary to control the position and the alignment of the mirrors. For the KAGRA suspension of the main mirror, the mirror should be cooled without significant vibration noise. Also the thermal noise from the suspension should be kept at a low level. In this thesis two points of them are mainly reported: vibration noise from the cooling system and thermal noise from the suspension.

3.1 Cryogenic suspension system

The cryogenic suspension system consists of five parts, including the mirror to suspend, and control the mirror; Platform (PF), Intermediate Mass (IM), Recoil Mass for the intermediate mass (IR), Recoil Mass for the main mirror (RM), and sapphire suspension system including the main mirror (or Test Mass: TM). The schematic views of the cryogenic suspension system are shown in the Fig.3.1.

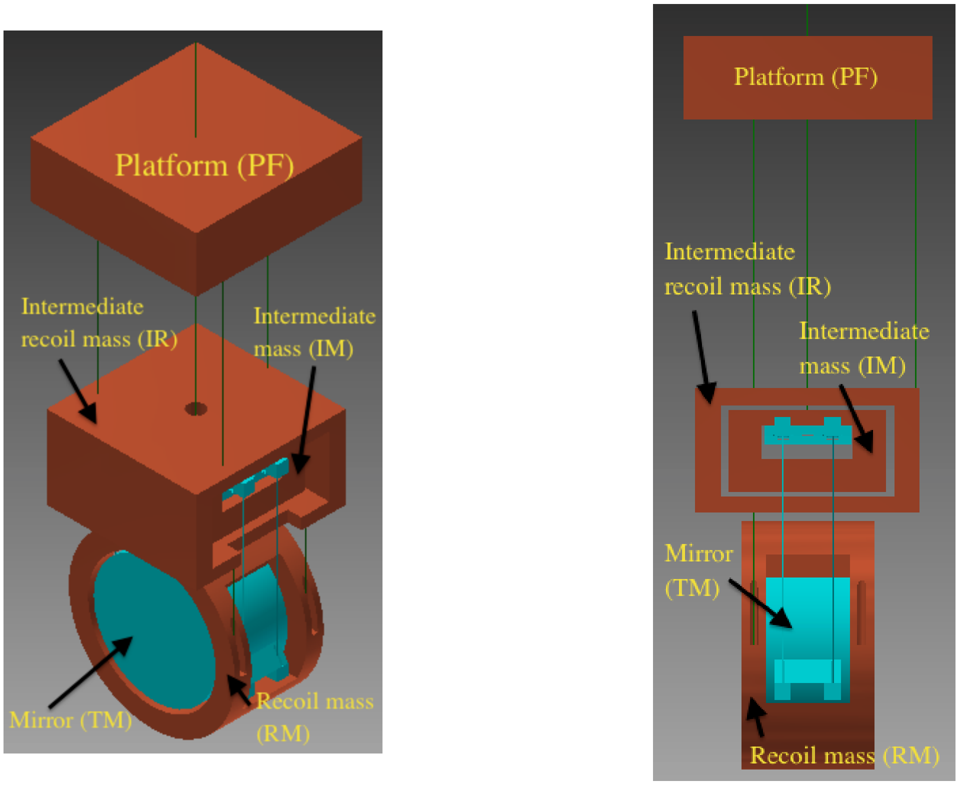

Figure 3.1: Cryogenic suspension system. The light blue components are called the cryogenic sapphire suspension system.

The top of the cryogenic suspension system is so-called platform suspended from a seismic attenuation system (SAS) by a single metal wire. On this platform there are mass shifters which adjust the tilt of PF and IR for the initial alignment. Moreover, in the platform, there is a vertical spring system (GASF) made of metal to reduce the vertical vibration entering the intermediate mass and the main mirror. The intermediate mass is suspended using a metal wire from the platform. This intermediate mass also has mass shifters to adjust the tilt of the intermediate mass and the main mirror for the initial alignment. During the main interferometer operation, the position and tilt of this intermediate mass will be controlled by sensors and coil magnet actuators on the intermediate mass and the intermediate recoil mass suspended from the platform using three metal wires. These sensors for sensing the differential position between intermediate mass and intermediate recoil mass are planned to use shadow sensors. A recoil mass of the main mirror is suspended from the intermediate recoil mass by four metal wires. This mass is to control the alignment of the main mirror as a recoil mass like intermediate recoil mass. There are coils on the recoil mass to apply force on the magnets attached on the mirror. A sapphire suspension system consisting of sapphire blades, sapphire fibers, and sapphire ears and the main sapphire mirror is suspended from the intermediate mass. The reason why sapphire is used for these components is that sapphire has high thermal conductivity and low mechanical loss at low temperatures. There is another important function except those described above, which is to reduce the vibration of the cooling system. This topic is described in the latter section.

3.2 Sapphire suspension system

To reduce the thermal noise, Advanced LIGO and Advanced VIRGO will use monolithic suspension systems for the main mirror. In the case of Advanced LIGO, fused silica mirrors which have 40 kg will be suspended by four fused silica fibers which have 0.4 mm diameter of the thinnest part [48]. In the case of Advanced VIRGO, 42 kg fused silica mirrors will be suspended by 0.4 mm fused silica fibers [49]. HCB is used for the connection between the fiber heads and the mirror.

The purposes of the sapphire suspension system of KAGRA are holding the mirror and keeping the mirror at a low temperature during the main interferometer operating. We also have to take care of the suspension thermal noise of this system because this system is the nearest part of the main mirror. Therefore, the thermal noise from each part in there will directly affect the output of the interferometer. The reason why sapphire is used to build a suspension system around the mirror is that the sapphire has a good thermal conductivity to extract heat from the mirror and low mechanical loss, thus low thermal noise in a broad frequency band. The requirements for the strength, thermal conductivity and mechanical loss of each part in the sapphire suspension are shown in the next chapter. In this section the functions of each part are explained.

The designed sapphire suspension system is shown in Fig.3.2.

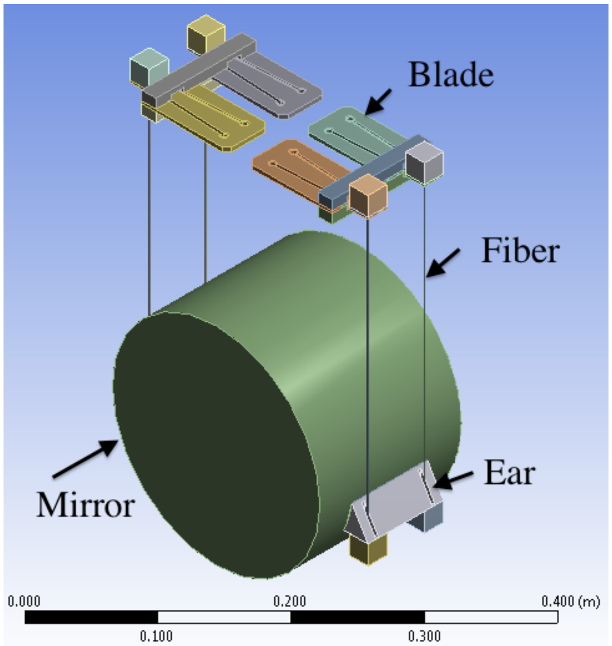

Figure 3.2: Cryogenic sapphire suspension system. This system contains a mirror, two ears, four fibers, four blades and four clamps. The ears will be bonded on the side of the mirror by a strong bonding technique like HCB. Also the lower fiber head will be bonded with the ear and the upper head will be bonded with the blade by a detachable bonding technique like indium bonding.

This system consists of the main mirror, two ears, four fibers, four blades and four clamps. In this suspension there are two kinds of bonding technique will be used. One of them is Hydroxide-Catalysis Bonding (HCB) which has extremely strong strength. The other one is indium bonding which is not so strong as HCB, but it is easy to remove using heat or acid.

In the following, the functions of the each part in the cryogenic sapphire suspension system are described.

3.2.1 Mirror

The sapphire mirror has 220 mm diameter, 150 mm thickness, therefore the mass is 22.6 kg. There are flat cuts on both the lower sides for bonding ears. Because the bending length of the fiber is $\sim 5\,\mathrm{cm}$ as described in the following, these flat cuts are not located at the center of the mirror side. Sapphire crystal has three axes which are m, a, and c-axes. To reduce the effect of the birefringence, c-axis of the crystal should be along the main laser line. The profile of the laser spot on the mirror coating surface is given by

$$P(r) = \frac{2}{\pi w_0^2} \exp\left(\frac{-2r^2}{w_0^2}\right), \tag{3.1}$$

where w_0, r are the radius of the laser ($1/e^2$ radius) and the distance from the center of the mirror surface. In the case of KAGRA, $w_0 = 3.5\,\mathrm{cm}$ [43].

3.2.2 Ear

The ears will be bonded by HCB on the side cut flat surfaces of the mirror to have surfaces for hooking in the fiber. The shape of the ears is a triangle pole shape and it has slits for the fibers like the Fig.3.4. In order to decrease the thermal noise, the size of the ear is chosen as small as possible as described latter. The surface of the ears against the mirror should be around or less than $\lambda(= 632\,\mathrm{nm})/10$ in terms of flatness. This flatness is always required for HCB to make a reliable bond [58].

3.2.3 Sapphire fiber

For suspending the mirror with sapphire fibers, the fibers should not be just a cylinder, but should have heads on the ends for connection. Our sapphire fibers with head(s) for experiments were produced by Impex which is one of the companies producing the sapphire fibers [53]. There are three kinds of requirement for this fiber, which will be described later: strength, heat conduction and mechanical loss.

To determine the length and diameter of the fiber, there are four issues to be considered. The first one is the violin mode of the fiber, which is described later in this subsection. The second is the size of the mirror and the recoil mass. Because the mirror has to be held in the limited space of the cryostat, the fiber length should be not only longer than the radius of the mirror but also long enough to make a space for the recoil masses. The third point is the heat path: the diameter should not be too thin. The last is the bending point on the fiber, which is explained in the latter part. We cannot use too thick fiber because the bending point will be away from the connection point. The detail of the first point and the last point are described in the following.

Violin mode of a fiber

The frequency of the first violin mode of a thin fiber can be written as the following.

$$f_{1st} = \frac{1}{2L}\sqrt{\frac{\sigma}{\rho}}, \tag{3.2}$$

where L, σ and ρ are the length, stress and density of the fiber, respectively. If four fibers which have radius r suspend the mirror mass M, the Eq.(3.2) can be rewritten like the following.

$$f_{1st} = \frac{1}{4Lr}\sqrt{\frac{Mg}{\pi\rho}}, \tag{3.3}$$

where g is the gravitational acceleration of the earth. In the case of KAGRA, because the sapphire fiber has a large diameter, the equation should be used is

$$\begin{aligned} f_{1st} &= \sqrt{\frac{Mg}{4\rho'}}\frac{1}{2L}\left[1+\frac{2}{k_eL}+\frac{1}{2}\left(\frac{\pi}{k_eL}\right)^2\right] && (3.4) \\ k_e &\sim \sqrt{\frac{Mg}{4YI}}, && (3.5) \end{aligned}$$

where ρ' and Y are the mass per unit length and Young's modulus [51, 52]. I is the inertial moment of the area:

$$I = \pi\frac{r^4}{4} \tag{3.6}$$

because the fibers are cylinder shape. As the most sensitive frequency range of KAGRA is around 100 Hz, if this violin mode appears nearby this frequency, observation of NS-NS binaries will be influenced. For instance, if the frequency of the first mode is 120 Hz, the inspiral range will decrease to about 80 % for the most observable NS-NS binaries [50]. Here the inspiral range means the distance of a NS-NS binary which KAGRA can observe. Moreover, there are many expectative observable gravitational waves from pulsars in the most sensitive frequency range (100-200 Hz) like J0537-6910 which is at the center of a supernova remnant NGC 2060 in the Large Magellanic Cloud. In terms of the heat extraction, the radius of the fiber should not be too small. The length of the fiber should be long enough to make a space of the recoil masses for the mirror and intermediate mass and for having a low resonance frequency of the pendulum mode. Because of the above situation, the current design of the fibers is 1.6 mm diameter and 300 mm length. In this case, the first violin mode frequency is ∼210 Hz.

Bending length

If very thin wires are used to suspend the mirror, the bending point of the wires are very close to the fixing points of the wire. In the case of the thick wire like 1.6 mm diameter sapphire fiber, the bending point appears significantly far from the fixing point. A schematic figure of the bending length b is shown in Fig.3.3.

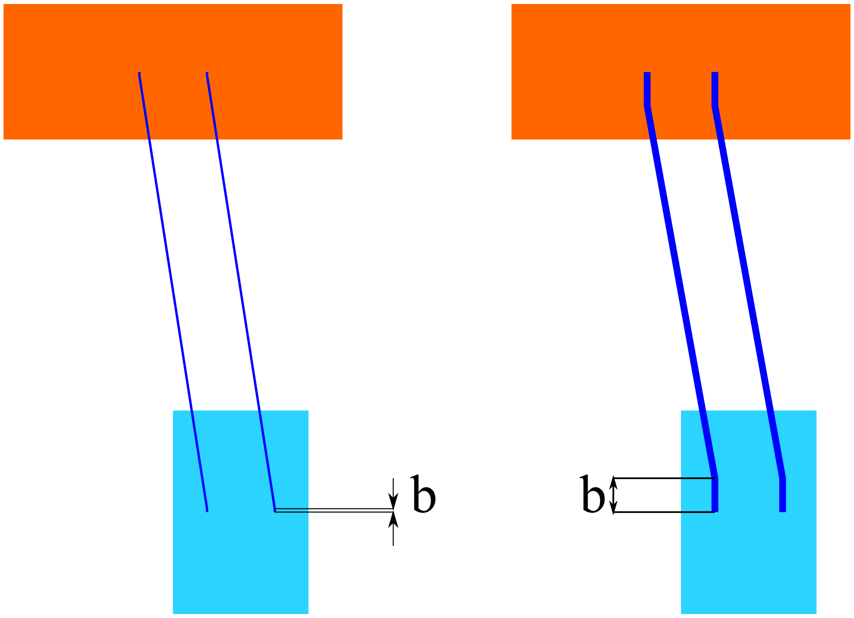

Figure 3.3: Bending length of the fibers. If the fibers are thin, the bending point will be very close to the fixing point of the fiber like the left figure. If the fibers are thick like KAGRA sapphire fiber, the bending point will be away from the fixing point like the right figure. b is the distance between the bending point and fixing point, which is called bending length.

If the fixing points of the wires on the mirror are the same horizontal plane as the center of mass of the mirror, the mirror rotates counterclockwise when a force is applied from the left side through the center of the mass of the mirror. This means the coupling between the translational motion along the beam line and the angular motion (pitch mode). In order to decrease this coupling, the bending point should be closer to the center of the mass of the mirror[1]. This is why the ears are designed to be attached on the lower sides instead of the right besides.

In the case of one wire and a point mass, G. Cagnoli et al. showed the bending length can be written as the following in their paper about damping dilution factor for a pendulum [55]. This equation also can be used for the KAKGRA fiber because the calculated bending length by this equation is much smaller than the total length of the fiber.

$$b = \sqrt{\frac{YI}{T}}, \tag{3.7}$$

there Y, I, T are the Young's modulus, the inertia moment of area of the wire and the tension in the wire. Here $L/b \gg 1$ is assumed. In the case of KAGRA, because the fibers are cylinder shape which has radius r,

$$I = \pi\frac{r^4}{4}. \tag{3.8}$$

---

[1] Of cause if the bending point and the center of mass are on the same horizontal plane, it would be unstable when one of the fibers is broken.

Therefore, the bending length b is,

$$b = r^2 \sqrt{\frac{Y_{sa}\pi}{Mg}}, \tag{3.9}$$

there $Y_{sa}(= 400\,\mathrm{GPa})$ is the Young's modulus of sapphire. If KAGRA parameters are assigned, $b = 4.8\,\mathrm{cm}$.

According to the above conditions, the size of the fiber is decided: 1.6 mm diameter and 300 mm length. Figure 3.5 shows the fiber shape. (15 years ago, because the thermal conductivity of the sapphire fiber was not clear, thinner fibers were assumed to be used. $\sim$ 1mm diameter or thinner [57].)

This sapphire fiber is a very important part in the cryogenic sapphire suspension because the suspension thermal noise from the fibers is thought to be the main noise. Also the fiber will limit the heat extraction from the mirror. Therefore, a study of the impact from the sapphire fiber on the suspension thermal noise and measurements of thermal conductivity of the sapphire fibers are performed. The details are reported in the later chapters.

3.2.4 Sapphire blade

The maximum difference of the length of ten sapphire fiber samples (10 cm fiber) provided by Impex was 0.45 mm. Four of them were in similar lengths within 0.1 mm. Therefore, 300 mm length fibers can have a 0.3 mm length difference, according to a rough estimation. To compensate for this length difference, sapphire blade springs will be used. In the case of a single spring system under the earth gravity, the displacement x and the resonance frequency f have a relation as,

$$x = \frac{g}{4\pi^2 f^2}. \tag{3.10}$$

In order that the displacement x can reach 0.6 mm which is double the length difference of the fibers, the frequency should be lower than 20.3 Hz. On the other hand, there is a pulsar at 22.5Hz, which is famous as the Vela pulsar. Below 15 Hz is chosen for the frequency of the sapphire blade spring, so as to keep away from the Vela pulsar frequency. The length of the blades should be shorter than the radius of the mirror because of the limited space. To reach such low frequency in the limited space, the blade shape is fixed to a folded plate as shown in Fig.3.6.

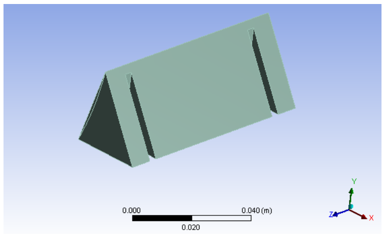

Figure 3.4: Ear. The reason why it is triangle shape is to reduce the mass.

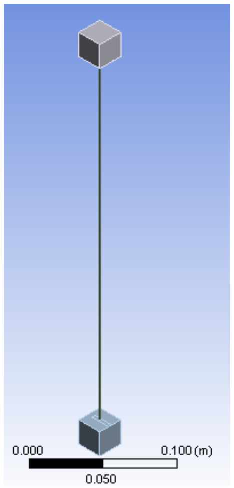

Figure 3.5: Fiber. Two heads on the both ends to be able to connect with other components. The head is 20 mm cubic.

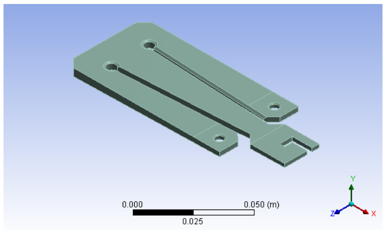

Figure 3.6: Blade. In order to save space, this blade is design as a folded shape.

3.2.5 Bonding

Two kinds of bonding will be used in the cryogenic sapphire suspension. One will be used between the mirror and the ear to hold the mirror, which should be a strong bonding. The other will be used between the fiber head and the ear, and between the fiber head and the blade, which should be a detachable bonding technique. What should be checked are the heat extraction and the impact on the suspension thermal noise. In this subsection, the bonding techniques are explained.

Hydroxide-catalysis bonding

The connection between the sapphire mirror and the ear should be strong enough to hold the mirror which has 22.3 kg weight and also the impact on the thermal noise from this bond should be smaller than the design sensitivity of KAGRA. There were three candidates for the bonding for this connection, which were indium bonding, diffusion bonding and Hydroxide-catalysis bonding (HCB) [58]. Among these three candidates HCB was the best possible candidate because the strength was thought to be good enough and any heat and high pressure are not necessary during the curing process like diffusion bonding. In the case of diffusion bonding, the bonding surface needs to be at $\sim 1000°\mathrm{C}$ and high pressure $\sim 100\mathrm{MPa}$ [56]. The strength of the indium bonding is the weakest in these three candidates.

HCB is a bonding technique used in the Gravity Probe B [61, 62, 63], which is one of the projects to verify the General theory of Relativity by observing the geodetic effect and frame-dragging of the gravity from the earth. The interferometer gravitational wave telescopes like LISA Pathfinder and GEO600, advLIGO, advVIRGO other than KAGRA also (will) use this bonding technic to connect optics. The merit of the HCB is that it forms a strong and thin bond. Moreover, the bond is suitable for high vacuum and low temperature. The strength test at low temperature is reported in a later chapter.

HCB can be applied to any material which has silicate structure. For the HCB between silica-based materials is studied well by including the University of Glasgow. In the case of silica-based materials, hydroxide ions in the solution erode silicon from the bulk bonding surface then create $Si(OH)_4$ in the bonding solution. After $Si(OH)_4$ forms siloxane chain as shown in Fig.3.7. Once the chains are formed, the connection is fixed. In the sapphire case, not only siloxane chain, but also aluminate chain can be formed in the bonding depending on the solution [60].

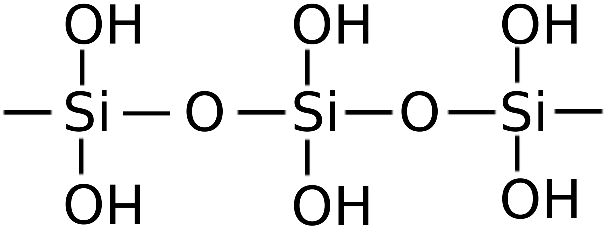

Figure 3.7: Siloxane chain formed in the bonding.

What should be tested for this bond is the strength after thermal cycles at low temperature, heat extraction and mechanical loss. The requirements and results are reported in the later chapters.

Indium bonding

One of the reasons why HCB is the best possible candidate to connect the ears to the mirror is that HCB can form a strong connection. Therefore, it is difficult to remove it. If the fibers or blades are broken by some accidents, we would have to discard also the mirror. Therefore, a bonding technique which is easy to be removed should be used between the mirror and fragile parts such as sapphire fibers or blades. Bonding using a metal which has low melting point like indium or gallium is a candidate. The melting point of gallium is 30 °C which is a bit too low in atmospheric pressure. Moreover, aluminum which is used in many parts in the cryostat can be corroded by the gallium. In the case of indium, the melting point is 157 °C and no special reaction with other metals. Furthermore, indium can be soluble in acids. Because of these reasons, the indium bonding is the most possible candidate for the detachable bonding.

3.3 Cooling system

The cryogenic suspension system will be cooled down to 20 K [64]. Figure 3.8 shows a schematic view of the cooling system.

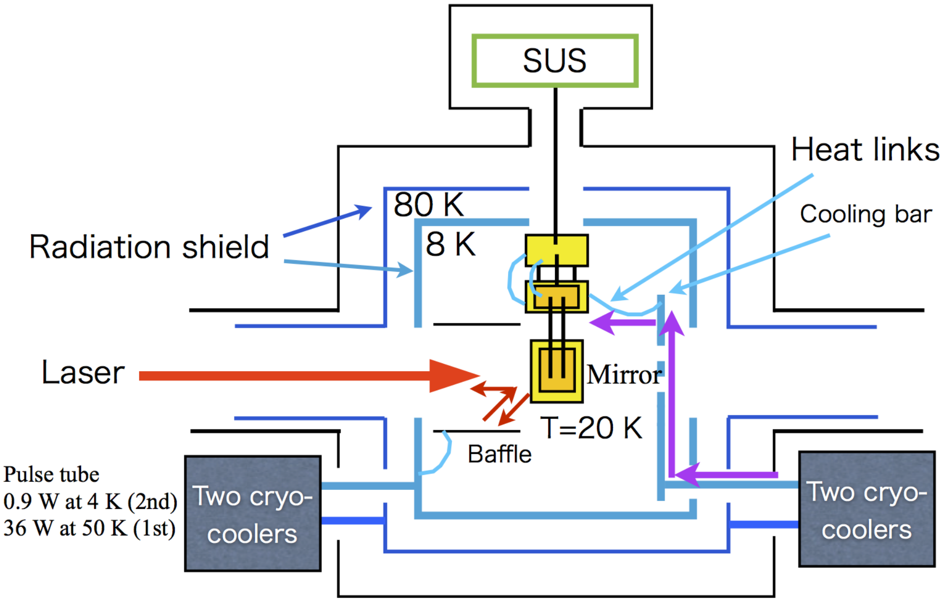

Figure 3.8: Cooling system of KAGRA. One cryogenic mirror will be surrounded by a double radiation shield to be protected from the thermal radiation coming from the chamber at room temperature. Two cryogenic coolers will be connected with the suspension to cool it through heat links.

A large cryostat which has four cryocoolers will cool one cryogenic system, including one sapphire mirror. Figure 3.9 is a picture of the cryostat manufactured by the Toshiba Keihin Product Operations [47] in Yokohama city.

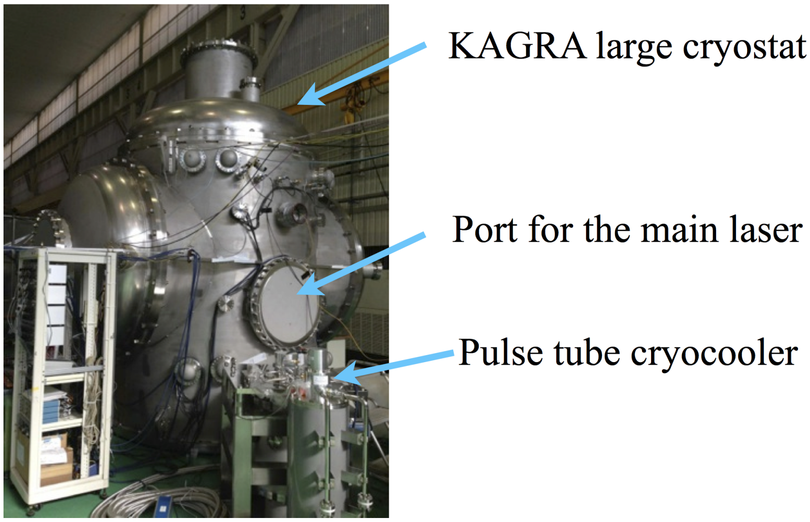

Figure 3.9: Picture of the cryostat of KAGRA in the factory of Toshiba in Yokohama city. Four pulse tube cryocoolers are connected.

Pulse tube cryocoolers will be used because cryogen of liquid helium cannot be used in the tunnel for safety. Also, if cryogen is used, connections pipes for the cryogen can be the vibration path from the outside. The principle of the pulse tube cryocoolers is given in the following. Helium gas in the cryocooler is compressed in a compressor which has a cooling system with water, and this compressed gas is carried into the cooling part, then the gas expands at the cooling part to extract heat. Pulse tube cryocooler repeats this process with a period of 1.6 Hz. Each cryocoolers has two cold stages. The 1st stage cannot reach a very low temperature, but it has a high cooling power to cool (30 W at 50 K). The 2nd stage can reach a very low temperature, but it does not have a high cooling power (0.9 W at 4 K). The KAGRA cryostat has double radiation shields which are called the 80K shield and 8K shield, respectively. The 1st stages of all of the cryocoolers are connected with the 80 K shield to keep this shield cold. The 2nd stages of two cryocoolers are connected with the 8 K shield. The 2nd stages of the other cryocoolers are connected with the cryogenic suspension using soft heat links made of metal wires. This is to separate the cooling path of the cryogenic suspension from the other components in order to keep the mirror at a low temperature. The best possible candidate of the material of the heat links is pure aluminum because of the high thermal conductivity, low Young's modulus and small density.

The cooling time of the cryogenic suspension is about one month [65]. The temperature change of a test mass can be written like the following.

$$\frac{\mathrm{d}T}{\mathrm{d}t} = \frac{Q(T)}{MC(T)}, \tag{3.11}$$

where Q, T, M and C are the flow of the heat, the temperature, the mass and the specific heat of the test mass, respectively. The cryogenic suspension will be cooled mainly by thermal radiation process down to $\sim$ 150K, and below this temperature the main contribution becomes a mechanical heat transfer because the heat transfer by the radiation is proportional to the difference of the fourth power of the temperature and the thermal conductivity of the heat links (pure metal) at a cryogenic temperature is higher than that at room temperature. The heat flow by the thermal radiation Q_r between the heat bath which has a temperature T_b and the test mass which has a temperature T_t can be written as

$$Q_r(T_b, T_t) = \epsilon_t A_t \sigma (T_t^4 - T_b^4), \tag{3.12}$$

where ϵ_t, A_t and σ are the emissivity, the effective surface area of the test mass and the Stefan-Boltzmann constant. On the other hand, the heat flow by the mechanical path Q_m is described by

$$Q_m = \frac{NS}{l} \int_{T_t}^{T_b} \kappa(T')\mathrm{d}T'. \tag{3.13}$$

At the last several tens Kelvin in the cooling process of the cryogenic suspension, the temperature goes down very rapidly because the specific heat goes down in proportion to the cubic of the temperature.

As described above, two cryocoolers are mechanically connected with the cryogenic suspension through the heat links to cool it down by thermal conduction. In order to reduce the vibration of the heat links, connecting the heat links against the cryostat or radiation shield which is massive is planned. This means the vibrations of the cryocoolers and the radiation shield are also transferred to the cryogenic suspension and the main mirror. In the case of the Cryogenic Laser Interferometer Observatory (CLIO) in Japan, which is a 100 m cryogenic interferometer [14, 15], the cryostat increased vibration by 100 times [16]. Because of these reasons, the vibration in the KAGRA cryostat needs to be estimated in the early stage to make measurements in the case of that the vibration of the cryostat is too large. Measurement of the vibration in the KAGRA cryostat was performed in 2013 in a factory of the Toshiba company which produced the cryostats to estimate the vibration of the radiation shield in Kamioka mine. The detail is described in the later chapter.

Chapter 4

Requirement of KAGRA sapphire suspension

In order to design the cryogenic sapphire suspension, the mechanical loss related to the thermal noise and the thermal conductivity related to the heat extraction have to be taken into account. In this chapter the requirements of the mechanical loss and thermal conductivity or heat extraction are described.

4.1 KAGRA sapphire suspension model

A 3D CAD model of the cryogenic sapphire suspension is designed by using an Inventor software produced by Autodesk. In order to calculate the elastic energy U_{max} closely related to the thermal noise, ANSYS workbench v15.0 was used. The model is shown in Fig.4.1. To put the center of gravity of the mirror close to the bending point of the fibers, the bottoms of the ears are located by 45 mm below the center of the mirror. The reason why the center of gravity of the mirror is below the bending points by 3 mm is to avoid unstable condition even if one of the fiber breaks. The face-on figures of the bondings are shown in Fig.4.2. In order to calculate the energy in the bonds, the author and colleagues calculate the case of thickness 50 μm by ANSYS and scale the energy for the thickness of the real bond.

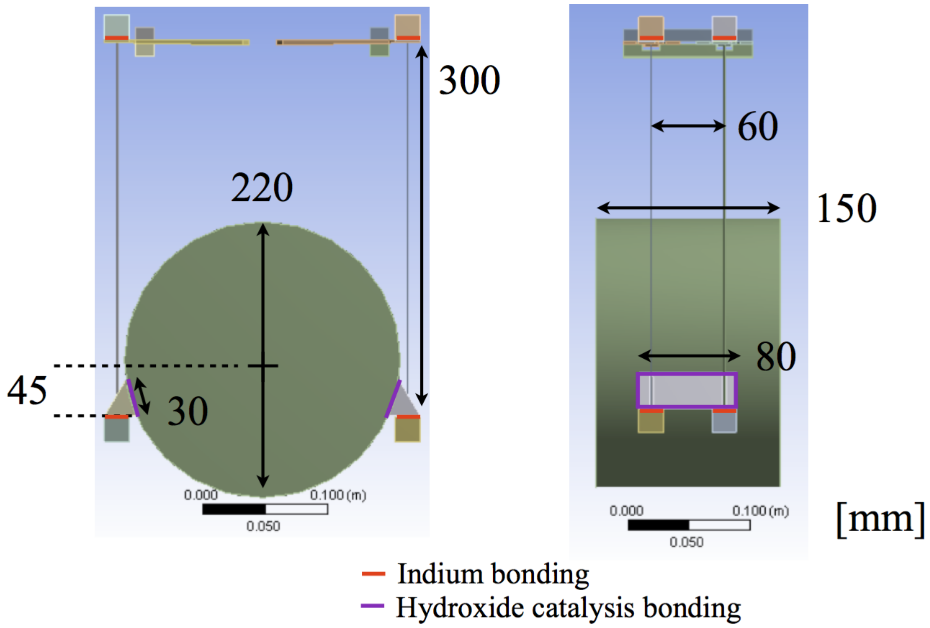

Figure 4.1: Model of the cryogenic sapphire suspension system. Two ears are attached on the side of the mirror by hydroxide catalysis bonding. Four fibers which have heads are suspending the mirror via the ears. The upper head of the fiber is on the blade which is fixed on the intermediate mass. Indium bonding is used between the ear and the fiber head, and between the fiber head and the blade.

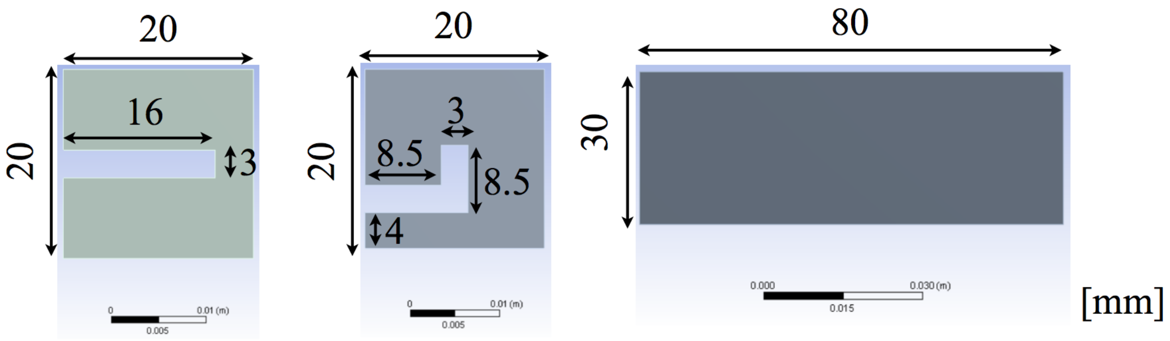

Figure 4.2: Bonding surfaces. Left is the indium bonding for the upper side. Center is the indium bonding for the lower side. Right is the HCB.

4.2 Thermal noise estimation methods

Thermal noise is a fundamental limit in sensitive measurements. For example, voltage thermal noise of resistance is one of the main noises in electrical circuits. Cryogenic techniques enhanced the resolution of electron microscopes. In the gravitational wave telescopes, thermal noise is also a main noise of the telescopes.

There is an important theorem for the thermal noise called the fluctuation-dissipation theorem which joints the thermal noise and the dissipation of the system [66, 67, 68, 69]. At first, a simple model about relationship between thermal noise and the dissipation is described here.

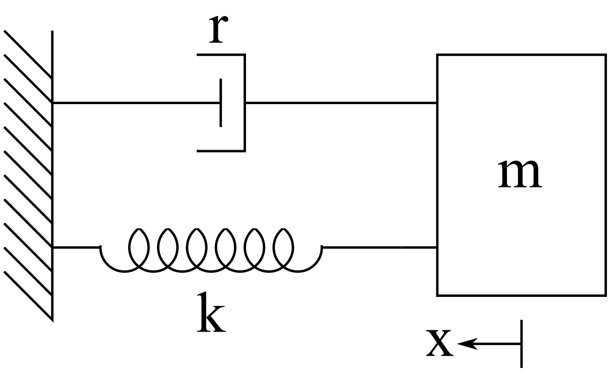

Figure 4.3: One spring with a velocity damping system. A point mass is supported by a spring which has a spring constant k and a damper which has a friction r.

The Langevin equation of a system with a test mass, a spring and a friction source as shown Fig.4.3 is given by

$$m\ddot{x} = F_{th} - r\dot{x} - kx, \tag{4.1}$$

where m is the mass of the test mass, x is the displacement, r is the friction factor, k is the spring constant and F_{th} is a fluctuating force caused by the random impacts of the molecules because of the friction. This F_{th} can be written by

$$F_{th}^2 = 4k_B T r \tag{4.2}$$

This equation can be solved in the frequency domain as

$$x^2(\omega) = \frac{4k_B T r}{(k - m\omega^2)^2 + r^2\omega^2}. \tag{4.3}$$

This gives a power spectrum of the thermal noise of a one spring with a damper which has a friction proportional to the velocity.

The fluctuation-dissipation theorem indicates that if the thermal driving fluctuating force F_{th} is written by

$$F_{th}^2(\omega) = 4k_B T R(\omega), \tag{4.4}$$

where $R(\omega)$ is the mechanical resistance which is the real part of the impedance Z:

$$Z \equiv \frac{F}{\dot{x}}, \tag{4.5}$$

then the power spectrum of the test mass is given by

$$x^2(\omega) = \frac{4k_B T\sigma(\omega)}{\omega^2}, \tag{4.6}$$

where $\sigma(\omega)$ is the mechanical conductance:

$$\sigma(\omega) = \mathrm{Re}\left[Y(\omega)\right]. \tag{4.7}$$

In this equation, $Y(\omega)$ is the admittance, which is the inverse of the impedance:

$$Y(\omega) = \frac{1}{Z(\omega)}. \tag{4.8}$$

Equation (4.6) is called the first fluctuation-dissipation theorem [68]. If Eq.(4.6) is used to calculate the thermal noise in the case of the one spring with a damping system described by Eq.(4.1), Eq.(4.3) can be derived naturally.

In the case of gravitational wave telescopes, internal damping is more natural than the damping proportional to the velocity. See Fig.4.4.

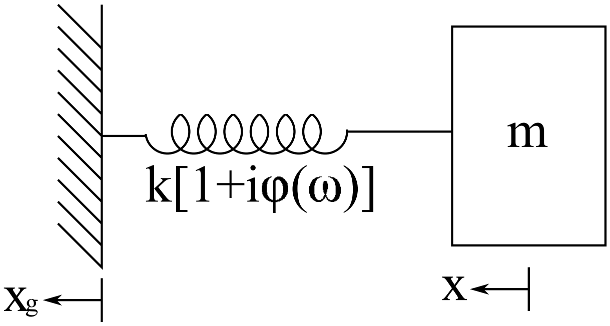

Figure 4.4: One spring with internal damping system. A point mass is supported by a spring which has a complex spring constant $k(1+i\phi(\omega))$.

For the internal damping the spring constant can be assumed to be complex:

$$F_{spring} = -k\left[1 + i\phi(\omega)\right]x. \tag{4.9}$$

The equation of motion becomes

$$m\ddot{x} = -k(1+i\phi)(x - x_g) + F. \tag{4.10}$$

Then the transfer function H and the mechanical impedance Z are given by

$$\begin{aligned} H &\equiv \frac{x}{F} = \frac{1}{-\omega^2 m + k(1+i\phi)}, & (4.11)\\ Z &\equiv \frac{F}{\dot{x}} = i\omega m + \frac{k}{i\omega} + \frac{k\phi}{\omega}. & (4.12)\end{aligned}$$

Because of the fluctuation-dissipation theorem the thermal noise power spectrum can be written like the following.

$$\begin{aligned} x^2(\omega) &= \frac{4k_BT\sigma(\omega)}{\omega^2} && (4.13) \\ &= \frac{4k_BTk\phi(\omega)}{\omega\left[(k-m\omega^2)^2+k^2\phi^2\right]} && (4.14) \end{aligned}$$

This is the thermal noise of a spring which has internal damping.

The most common function of the loss $\phi(\omega)$ is that the value is constant over a broad frequency band. Sometimes the loss depends on the frequency. One of the important example is thermoelastic damping. This is significant especially in some thin structure of wires or fibers. Because the coefficient of thermal expansion is not zero, the temperature of the sample depends on the strain. When non-isotropic strain occurs in the sample, heat flows from the high temperature part to the low temperature part to restore equilibrium. During this process, the elastic energy dissipation occurs. The detail is explained in the paper of Zener [73, 74]. The loss of this thermoelastic damping ϕ_{ED} is described as the following.

$$\phi_{ED} = \Delta\frac{\omega\tau}{1+\omega^2\tau^2}, \tag{4.15}$$

where Δ is called the relaxation strength, τ is called relaxation time, which can be written as the following respectively in the case of a cylinder shaped wire or fiber.

$$\begin{aligned} \Delta &= \frac{Y\alpha^2T}{c} && (4.16) \\ f_r &= \frac{1}{2\pi\tau} = 2.16\frac{D}{d^2} && (4.17) \end{aligned}$$

Y, α, T and c in the equation are the Young's modulus, the linear coefficient of thermal expansion, the temperature of the sample and the specific heat per unit volume. D is called the thermal diffusion coefficient, which satisfies $D = \frac{\kappa}{c}$, where κ is the thermal conductivity, and d is the diameter of the wire or fiber. The mechanical loss of the sapphire fibers at the room temperature is thought to be dominated by this damping.

In order to calculate complex systems, a direct approach which is described in the next section indicated by Levin in his paper can be used [18].

4.3 Suspension thermal noise

4.3.1 Thermal noise estimation by a direct approach

The paper written by Levin showed a direct method to calculate the thermal noise of a system for a gravitational wave telescope. His method is calculating the thermal noise from the stored energy in the system under a beam shaped force applying to the surface of the mirror.

Let's assume a force which has a frequency f on the mirror surface:

$$F(t) = F_0\sin(2\pi ft). \tag{4.18}$$

Then, because the mechanical admittance $Y(f)$ is

$$Y(f) = \frac{\dot{x}(f)}{F(f)} = \frac{2\pi i f x(f)}{F(f)}, \tag{4.19}$$

the displacement $x(f)$ can be written as the following,

$$\begin{aligned} x(f) &= \frac{Y(f)F(f)}{2\pi i f} && (4.20) \\ &= \frac{\mathrm{Re}\,[Y]\,F_0 \sin(2\pi f t)}{2\pi i f} + \frac{\mathrm{Im}\,[Y]\,F_0 \sin(2\pi f t)}{2\pi f}. && (4.21) \end{aligned}$$

The time derivative of x is

$$\frac{\mathrm{d}x(f)}{\mathrm{d}t} = \mathrm{Re}\,[Y]\,F_0 \sin(2\pi f t) + \mathrm{Im}\,[Y]\,F_0 \cos(2\pi f t). \tag{4.22}$$

The power W and the force should have a relation as

$$\begin{aligned} W &= f \int_{\text{one cycle}} F \mathrm{d}x = f \int_0^{\frac{1}{f}} F \frac{\mathrm{d}x}{\mathrm{d}t} \mathrm{d}t && (4.23) \\ &= F_0^2 \mathrm{Re}\,[Y] \int_0^{\frac{1}{f}} \sin^2(2\pi f t) \mathrm{d}t && (4.24) \\ &= \frac{F_0^2 \mathrm{Re}\,[Y]}{2}. && (4.25) \end{aligned}$$

Therefore,

$$\begin{aligned} \sigma(\omega) &= \mathrm{Re}\,[Y] && (4.26) \\ &= \frac{2W}{F_0^2}. && (4.27) \end{aligned}$$

If the fluctuation-dissipation theorem is applied, the thermal noise power spectrum can be estimated:

$$\begin{aligned} x^2(f) &= \frac{4 k_B T \sigma(\omega)}{(2\pi f)^2} && (4.28) \\ &= \frac{2 k_B T}{\pi^2 f^2} \frac{W}{F_0^2}. && (4.29) \end{aligned}$$

If the Young modulus E depends on the mechanical factor as in Eq.(4.9):

$$E = E_0 \left[1 + i\phi(f)\right]. \tag{4.30}$$

There, W can also be described as the following.

$$W = 2\pi f U_{max} \phi(f), \tag{4.31}$$

where U_{max} is the elastic energy when the test mass is at the maximum displacement.

From the above, in order to calculate the thermal noise $x^2(\omega)$, we can apply a force whose profile is the same as the beam profile in a simulation and calculate the elastic energy U_{max} stored in the system [18].

4.3.2 Thermal noise of KAGRA sapphire suspension

Requirements for mechanical loss values

The requirements are decided based on the design sensitivity of KAGRA [75]. See Fig.2.10. Thermal noise because of each part is calculated using an appropriate mechanical loss value, then we compare the calculated result with the design sensitivity to determine the mechanical loss for each part. Basically, the requirements of the thermal noise from each part are set to be lower than the design sensitivity by a factor of 2 in terms of strain. But in the low frequency band, the thermal noise from the fiber is thought to be around the required value according to the previous measurement for the thin fiber [17]. So the requirements of the other components were set to be lower than the required thermal noise of the fiber by a factor of 3 between 10 Hz and 50 Hz. This means if there are nine components which create the required thermal noise, the sum of them will finally reach the noise level because of the fiber.

It is the first estimation of thermal noise of a suspension under load using the Levin's method in this frequency band.

First, the requirements of mechanical loss for the clamps, blades, fibers and ears are shown in Table 4.5.

Table 4.1: Mechanical loss requirements

Component	ϕ_{req}
Ear	1.0×10^{-4}
Fiber	2.0×10^{-7}
Blade	7.0×10^{-7}
ClampU	8.6×10^{-4}
ClampB	8.6×10^{-4}

Figure 4.5 shows the thermal noise from each sapphire part with the required mechanical loss.

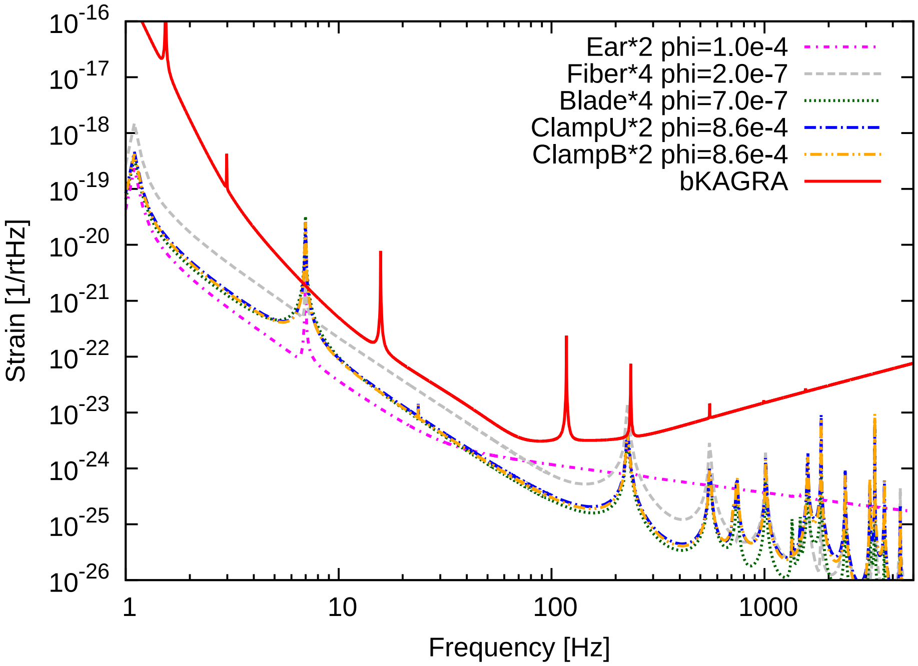

Figure 4.5: Thermal noise spectrum of sapphire parts calculated from the required mechanical loss. The red line is the design sensitivity of KAGRA. Other lines are thermal noise from each part of the sapphire suspension when each parts have the required mechanical loss.

Next, the requirements for bonds are shown in Table 4.6. The thickness of the indium bonding is $\sim 1\mu$m because this thickness is needed to smooth the sapphire surface and there is no difficulty to use an evaporation technique to make such layer. Moreover, foils of indium are also available for purchase. The thickness of HCB is $\sim$ 60nm reported by L. Cunningham et al in their paper [70]. Because the thickness of the bonds is much thiner than the other structures, the energy in the bonding can be assumed to be proportional to the thickness. This means if 10 times thicker bond is used, the requirement will be 10 times lower for the mechanical loss of the bond to cancel.

Table 4.2: Mechanical loss requirements

Component	Thickness	ϕ_{req}
Bond between a blade and a fiber	1μm	1.5×10^{-2}
Bond between a fiber and a ear	1μm	1.5×10^{-2}
Bond between a ear and the mirror	60nm	1

Figure 4.6 shows the thermal noise from each bonding which has required mechanical loss.

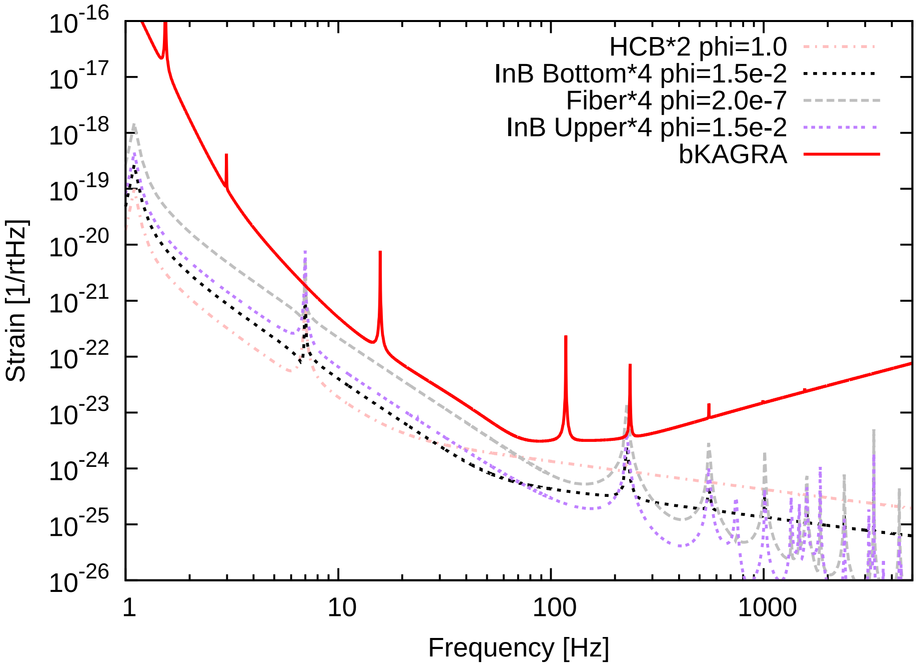

Figure 4.6: Thermal noise spectrum of bonding parts calculated from the required mechanical loss. KAGRA design sensitivity is the red line. The thermal noise from bonds and fibers are plotted in this graph when the bonding and fiber have required mechanical loss.

Normally, the parts closer to the mirror than the fiber create higher thermal noise in the high frequency range. For example, the thermal noise from the indium bond between the ear and the fiber (InB Bottom in Fig.4.6) is higher than that of the indium bond between the fiber and the blade (InB Upper in Fig.4.6) in the high frequency range in the case of the same mechanical loss. This is due to the suppression by the fiber pendulum.

Table 4.3 shows the physical properties used in the thermal noise calculation.

Table 4.3: Physical properties used in the thermal noise calculation

Material	Young's modulus [GPa]	Poisson's ratio	Reference
Sapphire	460	0.25	[71]
HCB	7.9	0.25	[58]
Indium	19	0.3	[72]

The way to reduce the requirement

When we look at the thermal noise from HCB carefully, we can find that the curve is straight above 30 Hz and the noise at 80 Hz is the closest point to the design sensitivity of KAGRA. This noise at 80 Hz is still acceptable, but it can be reduced even if the mechanical loss vales are the same. The way is to reduce the mass which is attached on the bond at the ear and the sapphire fiber heads because the noise level above 80 Hz depends on the reaction mass on the bond.

The principle of the thermal noise calculation is to calculate the elastic energy in the bond under applying a force on the mirror. Therefore, a simple model shown in Fig.4.7 can be used.

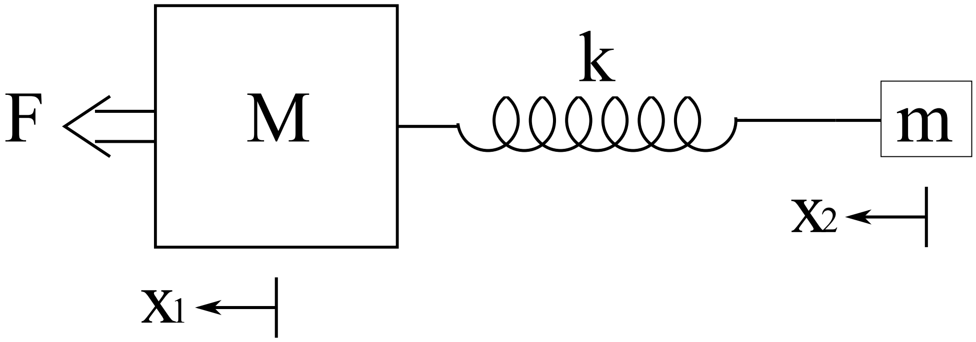

Figure 4.7: A simple model of a reaction mass. Two masses are connected with each other by a spring which has a spring constant k.

Equations of moment for each mass in this model can be written by

$$M\frac{\mathrm{d}^2 x_1}{\mathrm{d}t^2} = F - k(x_1 - x_2) \tag{4.32}$$

$$M\frac{\mathrm{d}^2 x_2}{\mathrm{d}t^2} = k(x_1 - x_2) \tag{4.33}$$

By applying Fourier transformation:

$$-\omega^2 M x_1 = F - k(x_1 - x_2) \tag{4.34}$$

$$-\omega^2 m x_2 = k(x_1 - x_2) \tag{4.35}$$

Therefore, the energy E_e in the spring can be described as

$$E_e = \frac{1}{2}k(x_1 - x_2)^2 \tag{4.36}$$

$$= \frac{1}{2}\left(\frac{Fm}{kM}\right)^2, \tag{4.37}$$

where $\omega \ll \sqrt{\frac{m+M}{mM}k}$ and $m \ll M$ are assumed. The higher energy value means the higher thermal noise from the spring which is a bond in the case of KAGRA if the spring has a mechanical loss. This equation means the energy in the spring is proportional to m^2 which is the mass attached to the bond. Because the thermal noise power spectrum density is proportional to the square root of the energy, the noise is proportional to the mass m.

In the case of HCB in the KAGRA cryogenic sapphire suspension, the attached masses are the ear and two fiber heads. Each mass of them is

$$m_{\text{ear}} = 111[\text{g}] \tag{4.38}$$

$$m_{\text{head}} = 32[\text{g}]. \tag{4.39}$$

Therefore, if the size of the fiber head or ear is decreased, the thermal noise from the HCB can also be decreased at high frequencies. The thermal noise with big fiber heads ($tickness = 20$mm: base design) and that with small fiber heads ($tickness = 10$mm) are calculated for comparison. The thermal noise of HCB, the ear and the indium bonding around 100 Hz with a small and large head is shown in Figs.4.8, 4.9 and 4.10.

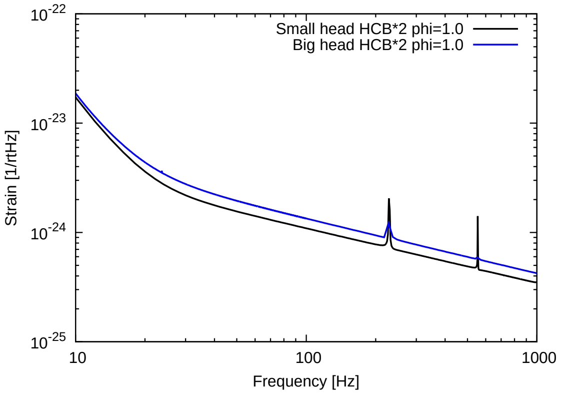

Figure 4.8: Thermal noise from HCB in the case of small/big head. In the case of the small fiber head, the thermal noise is smaller.

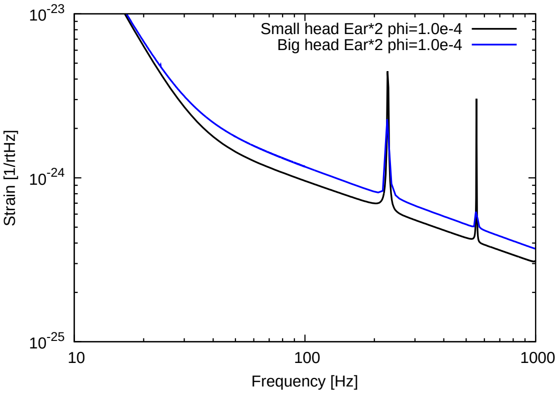

Figure 4.9: Thermal noise from the ear in the case of small/big head. In the case of the small fiber head, the thermal noise is smaller.

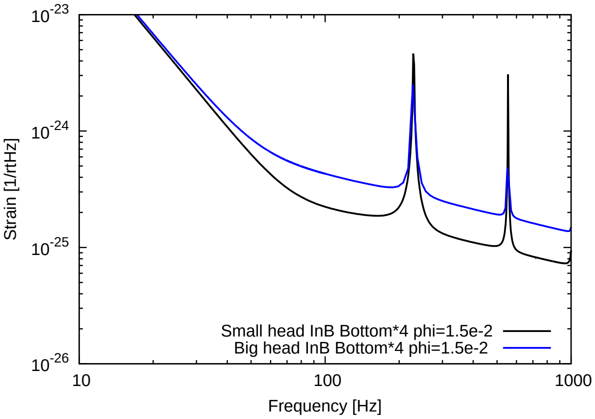

Figure 4.10: Thermal noise from the indium bonding(InB) on the ear in the case of small/big head. In the case of the small fiber head, the thermal noise is smaller.

From the calculated results, the thermal noise with small heads is 82% (HCB), 85% (ear), 49% (indium bonding bottom side) of the noise with big heads in the straight region.

The mass ratios are:

$$\frac{m_{\mathrm{ear}} + 2m_{\mathrm{small\,head}}}{m_{\mathrm{ear}} + 2m_{\mathrm{big\,head}}} = 0.82 \tag{4.40}$$

$$\frac{m_{\mathrm{small\,head}}}{m_{\mathrm{big\,head}}} = 0.50. \tag{4.41}$$

These values are consistent with the thermal noise calculation.

As just described above, in order to decrease the thermal noise on the bonding under the same mechanical loss, decreasing the mass on the bond is an obvious choice. This also indicates that if a heavy mass is attached on the mirror via HCB in place of the ear shown above, the thermal noise could exceed the design sensitivity of KAGRA.

4.4 Thermal conductivity

During the operation of KAGRA, a high power laser passes through the front mirrors, then a part of the power is absorbed into the mirrors. So as to keep the mirrors at 20 K, this absorbed power should be extracted from the mirror through the cryogenic sapphire suspension. Because sapphire is known as a very high thermally conductive material at low temperatures, sapphire bulk parts of ears, blades and clamps should not cause any problems. But thin elements of the fibers and non-sapphire parts of bonds are the points that should be investigated.

The input laser power into the power recycling cavity is planned to be 80 W at the maximum [76]. The power in the power recycling will be $P_{\mathrm{INm}} = 800\,\mathrm{W}$ because of the gain 10 of the power recycling and this power also penetrates into the inside of the front mirror. Thus, a part of this power will be absorbed by the sapphire mirror bulk with the absorption coefficient α_m. The mirror coating which faces toward the main arm cavity also absorbs the power of the laser. The laser power in the arm cavity will be $P_{\mathrm{Inc}} = 400\,\mathrm{kW}$ because of the cavity gain. Therefore, a part of this main cavity power is absorbed by the coating with the absorption coefficient α_c. In order to estimate the power that should be extracted from the mirror, the information of the absorption is necessary. The lowest absorption in the samples measured by the KAGRA mirror group was $\alpha_{\mathrm{m}} \sim 30\mathrm{ppm\,cm^{-1}}$ although the measured samples have a spread $(30 \sim 70\mathrm{ppm\,cm^{-1}})$ [77]. In the case of the coating, $\alpha_{\mathrm{c}} \sim 0.5\mathrm{ppm}$ is used here [78]. Because the thickness of the mirror is $t_{\mathrm{m}} = 0.15\mathrm{m}$, the power P_{i} which should be extracted during operation from the mirror is

$$\begin{aligned} P_{\mathrm{i}} &= P_{\mathrm{INm}} t_{\mathrm{m}} \alpha_{\mathrm{m}} + P_{\mathrm{INc}} \alpha_{\mathrm{c}} && (4.42) \\ &= 560[\mathrm{mW}]. && (4.43) \end{aligned}$$

4.4.1 Fibers

The KAGRA cryogenic mirror will be suspended by four sapphire fibers, which are 300 mm in length and 1.6 mm in diameter. Because the intermediate mass will be kept at 16K during the operation, the difference of temperature between the mirror and the intermediate mass is $\Delta T = 4\,K$ if the temperature of the mirror is kept at 20 K. Then the requirement for thermal conductivity of the fiber $\kappa_{\mathrm{f\_Req}}$ can be determined by the equation of heat transfer

$$\Delta P = \frac{A}{l}\kappa_{\mathrm{f\_Req}}\Delta T, \tag{4.44}$$

where ΔP is the power, which should be transferred by one fiber, A, l are the cross section and the length of a sapphire fiber, respectively. Therefore, the requirement can be given by

$$\kappa_{\mathrm{f\_Req}} = 5000[\mathrm{W/mK}]. \tag{4.45}$$

4.4.2 Bondings

The requirement of the heat transfer of the bond can be determined easily. Because the temperature difference between the mirror and the intermediate mass is 4 K, the required temperature difference through each bond is set as 0.1 K. As explained in a later chapter, measurement of the thermal conductivity of bonded sapphire samples was performed. See Fig.4.11.

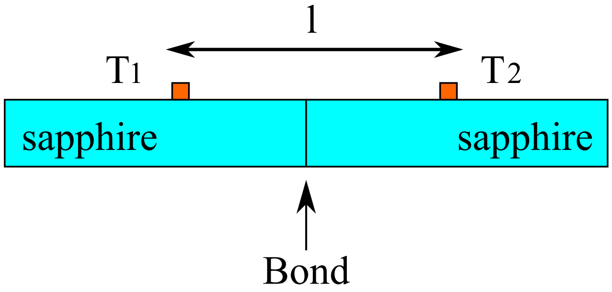

Figure 4.11: Schematic view of the thermal conductivity measurement of a bonded sample. Temperature gradient through the bonded sample can be measured by the two thermometer T_1 and T_2.

The value of $\frac{\kappa}{l}$ of the samples which include a bond can be estimated from the experiment. Here the requirement for this value can be determined using the following equation.

$$\Delta P = A\frac{\kappa}{l}\Delta T, \tag{4.46}$$

where ΔP is the power, which should be transferred to each bond, A is the cross section of each bond and $\Delta T = 0.1\mathrm{K}$ is the required temperature difference through the bond. In order to be on the safe side, the heat conductivity of the sapphire blocks are assumed to be high enough. Therefore, the temperature difference between the sensors is assumed to be caused by the bond. Therefore, in the case of HCB, the requirement is

$$\begin{aligned} \frac{\kappa}{l}_{\mathrm{HCB\_Req}} &= \frac{\Delta P}{A\Delta T} && (4.47) \\ &= 1000\left[\frac{\mathrm{W}}{\mathrm{m^2K}}\right], && (4.48) \end{aligned}$$

where ΔP is 0.25 W and A is $80\times 30\mathrm{mm}^2$. (Because the total power needs to be extracted is ~0.5 W and a mirror has two faces of HCB, ΔP =0.25 W.) In the case of indium bonding,

$$\frac{\kappa}{l}_{\mathrm{InB\_Req}} = \frac{\Delta P}{A\Delta T} \tag{4.49}$$

$$= 3000 \left[\frac{\mathrm{W}}{\mathrm{m^2K}}\right], \tag{4.50}$$

where ΔP is 0.12 W and A is assumed to be $20\times 20\mathrm{mm}^2$. (Because the total power needs to be extracted is ~0.5 W and a mirror has four faces of the indium bonding, ΔP =0.12 W.)

4.5 Strength

The fragile parts in the cryogenic sapphire suspension are the fiber and the bonding between the mirror and the ear.

4.5.1 Sapphire fiber

Because 5.7 kg weight will be loaded for each sapphire fiber, a maximum tolerable weight of 17 kg is the requirement for each fiber with a safety factor of 3. The strength test for the fiber has been performed by Giles Hammond (Glasgow University) and Ettore Majorana (the University of Rome). They tested three short fibers (~10 cm), one of them is a monolithic fiber (this fiber is called "type A fiber") and another is a "non-monolithic" fiber (this fiber is called "type B fiber"), and the other one is so called "type C fiber". All of them were produced by Impex [53]. The "monolithic" fiber (type A fiber) is a thin monolithic fiber part with heads, which they produced by shaping from one piece of sapphire crystal. The "non-monolithic" fiber (type B filer) is a fiber with heads, which is not monolithic, but connected by plasma-welding to make a quasi-monolithic joint (alumina brazing). This type B fiber is called HEM fiber, which stands for Heat Exchanger Method fiber. This method can control the growth process by the heat exchanger gas. The fiber part of the type B was thermo-polished, which is a technique to reduce defects on the surface by a high temperature gas flow through the surface [54]. Type C fiber is a fiber with monolithic head and a welded head. At first, one head with a neck (~ 10 mm) was produced, then a fiber was grown from the neck as a seed. The pictures of the fibers for the breaking test are shown in Fig.4.12.

Figure 4.12: Sapphire fibers for the strength test. The left figure is a Type C fiber. The center figure shows a Type A fiber. The right figure is a Type B fiber.

“S1” is the type C fiber, and “S2” is the type A fiber, and “S3” is the type B fiber. They were loaded with 6.5 kg and 15 kg then were shaken by 5-7 mm amplitude. In the result all of the fibers survived. After the vibration test, static load test was performed. Table 4.4 shows the result.

Table 4.4: Strength test result

Sample number	Type	specialty	Maximum load
S1	C	Monolithic head and neck, no polish	$> 90\,\mathrm{kg}$
S2	A	Monolithic, no polish	56 kg
S3	B	Non-monolithic: plasma-welding, HEM, thermo-polish	35 kg

The sample “S1” could not be broken because of the apparatus. All of the fibers were found to be strong enough.

4.5.2 Bond

The bonding (HCB is the strongest candidate) between the mirror and the ear has to hold the weight of the mirror. The author and colleagues determined that the bonding surface should have a 30 mm × 80 mm area, to have a safe margin for the strength of HCB and keep enough space between blades. According to a simple calculation below, the strength of HCB should be

$$\begin{aligned} T &= \frac{F}{S} && (4.51)\\ &= \frac{Mg}{S} && (4.52)\\ &= 92\,[\mathrm{kPa}], && (4.53) \end{aligned}$$

where $M = 22.6\,\mathrm{kg}$ is the mass of a main mirror, $g = 9.8\,\mathrm{m/s^2}$ is the acceleration of gravity, $S = 30\,\mathrm{mm} \times 80\,\mathrm{mm} \times 2 = 4.8 \times 10^{-3}\,\mathrm{m}^2$ is the sum of the bonding area between the mirror and the ears.

Calculation of the stress on the bonding surface by a FEM simulation was also done. In this simulation, we used the real KAGRA sapphire suspension model where the ear is attached a little bit lower than the gravity center of the mirror. While this position of the ear minimizes the size of the ear, tearing stress on the surface can also be reduced. Only the standard gravity is applied to the sapphire suspension in this simulation. The result is shown in Fig.4.13.

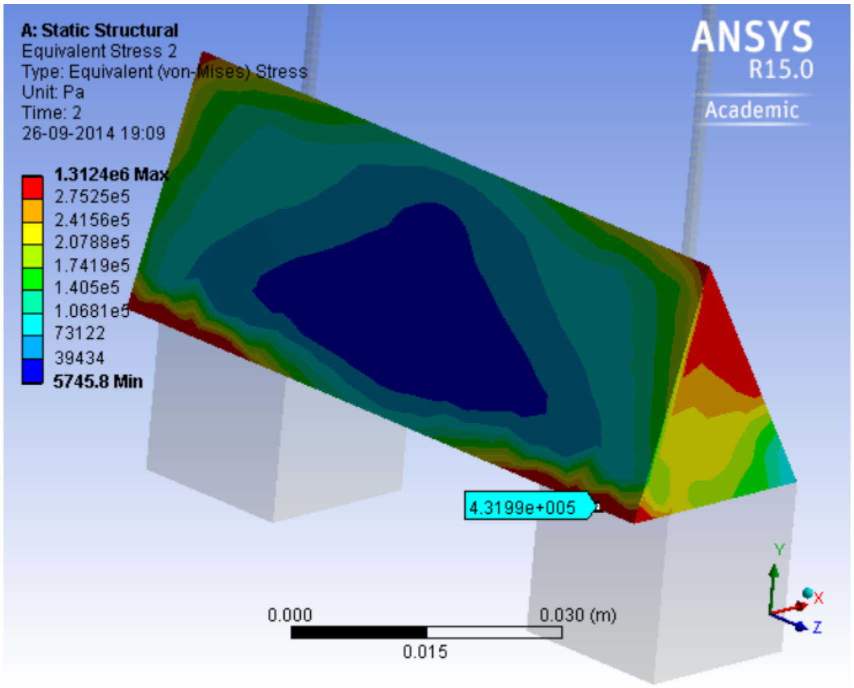

Figure 4.13: Stress on the HCB surface. The maximum value is 0.43 MPa which is higher than what is given by a simple calculation.

According to this simulation, the maximum stress on the bonding surface is 0.43 MPa. 1 MPa can be set as the strength requirement adapting a safety factor of 2. This is the requirement at temperatures from 10 K up to room temperature.

In addition, normally a large-scale interferometer needs to be adjusted many times at many points including main mirror suspension. Therefore, the cryogenic system will experience thermal cycle several times until the stable operation is reached. According to the current cooling system, it takes 40 days to cool down and also 10 days to warm up. If the maintenance takes one month or more at room temperature, one thermal cycle takes three months. This indicates that the cryogenic suspension should experience <2 times of thermal cycle per year to secure a sufficient observation time. If the first cryogenic payload will be used for ten years, the HCB on the mirror should experience 20 thermal cycles. From this assumption, the strength test at liquid helium temperature was performed after 10 or 20 thermal cycles. The result is shown in a later chapter.

Chapter 5

Mechanical loss measurement

In this chapter, mechanical loss measurement experiments are reported. As described above, in order to achieve low thermal noises, each part in the cryogenic sapphire suspension should have low mechanical loss. Even sapphire is known as a low mechanical loss material at low temperatures, thin sapphire parts, and bonding can be noise sources. Therefore, the mechanical loss of sapphire fibers, HCB and indium bonding were measured.

There are two popular methods to estimate the mechanical loss. One is to measure the decay time of the eigenfrequency. In the case of inertial damping, the impulse response of an oscillator can be given by

$$x(t) = \frac{F}{m\omega_0^2\phi} \exp\left(-\frac{\omega_0}{2}\phi t\right) \sin(\omega_0 t), \tag{5.1}$$

where ω_0 is the resonance angle frequency. The mechanical loss ϕ can be estimated from the exponential fitting of the decay curve after an excitement of the resonance mode. The amplitude of this signal will be $\frac{1}{e}$ of the initial value when

$$t = \frac{2}{\omega_0\phi}. \tag{5.2}$$

This value is called the decay time.

The other way to estimate the loss is to measure the spectrum around the resonance frequency. When the angular frequency $\Delta\omega$ satisfies the condition

$$\left|H\left(\omega_0 \pm \frac{\Delta\omega_0}{2}\right)\right|^2 = \frac{|H(\omega_0)|^2}{2}, \tag{5.3}$$

where $H(\omega)$ is described by Eq.(4.11), the value of $\Delta\omega_0$ should be

$$\Delta\omega_0 = \omega_0\phi. \tag{5.4}$$

This $\Delta\omega_0$ is the so-called half width. Therefore, the loss can be estimated from this half width if the spectrum of the resonance frequency is measured.

Usually, the decay time measurement method is used for the measurement because a very high frequency resolution is necessary in the case of very low loss for the spectrum measurement. As described above, the resonance frequency also affects the decay time: the higher resonance frequency has a shorter decay time. Therefore, when the decay time was too short to measure because of the high loss or high resonance frequency, the spectrum measurement method was performed.

5.1 Sapphire fiber

In this section the measurement of the sapphire fibers is described. As reported by T. Uchiyama in their paper [17], the mechanical loss of a sapphire fiber which has 250 μm diameter without any head was measured, and showed that the mechanical loss value was acceptable for KAGRA. But there were no any measurements of a thick fiber like 1.6 mm diameter and a fiber with heads which are designed for KAGRA cryogenic sapphire suspension.

Short fibers (~ 10 cm) were measured for brevity. The diameter of the fibers is 1.6 mm. The requirement of the mechanical loss is 2×10^{-7} as shown in the previous chapter. The pictures of the fibers the author and colleagues measured are shown in the Fig.5.1.

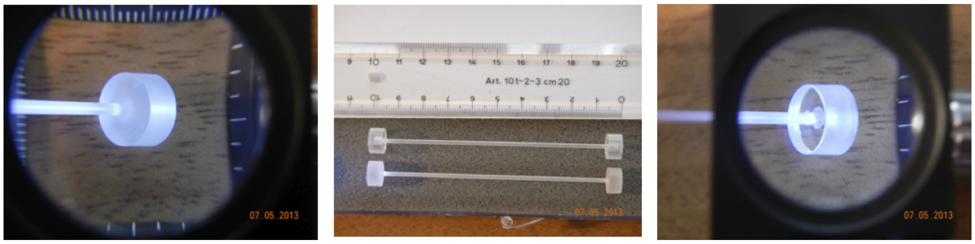

Figure 5.1: Fibers of which we measured the mechanical loss. On the left side is type A fiber and on the right side is type B. The total length of a fiber is 10 cm. The diameter is 1.6 mm. Both heads on the end of the fibers have 10 mm in diameter and 5 mm thickness.

Two kinds of fiber were measured. One of them is a monolithic fiber whose heads and fiber part are monolithic (Type A fiber). The other fiber is a non-monolithic fiber whose connection points between heads and fiber are brazed through alumina (Type B fiber). The type B fiber was manufactured by HEM and experienced a thermo polish.

5.1.1 Experimental setup

In order to measure the mechanical loss, we need an actuator to excite the resonance frequencies or resonance modes and a sensor to monitor the vibration of the fiber.

The electrostatic actuator used for the exciting is a common contact-less actuator.

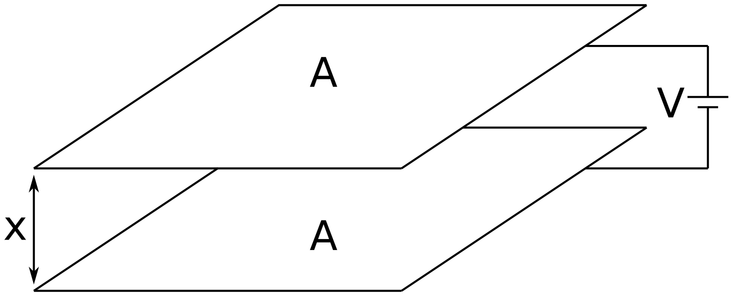

Figure 5.2: Principle of an electrostatic actuator. When a voltage is applied between two plates, attractive force arise between the plates.

If we assume a condenser like Fig.5.2 in vacuum, the electrostatic energy U_{es} in the condenser can be written as

$$U_{es} = \frac{1}{2}CV^2 = \frac{1}{2}\frac{\epsilon_0 A}{x}V^2, \tag{5.5}$$

where ϵ_0 is the permittivity of a vacuum, A, x and V are the area, the distance and the voltage difference between the two plates. Then the force between the two plates is an attracting force F_{es}, which can be described as,

$$F_{es} = \frac{\partial U_{es}}{\partial x} = -\frac{\epsilon_0 A}{2x^2}V^2. \tag{5.6}$$

In order to have enough excitement, the actuator plate should be close to the sample according to this equation.

On the other hand, the sensor we used is an optical sensor which is called a photon sensor. This sensor emits light and estimate the distance between the sensor and the target from the light reflected by the surface of the target. If the distance is long, the detected reflection light is faint. The model number is “Fiberoptic Sensor Model D63” produced by PHILTEC Inc [79]. An optical fiber was used to lead the light into a vacuum chamber or a cryostat to sensing a target in there.

In order to measure a very low mechanical loss, a system which has very good vibration isolation system was used to prevent the energy in the sample escaping from the measurement system. Figure 5.3 shows a picture of the cryostat we used.

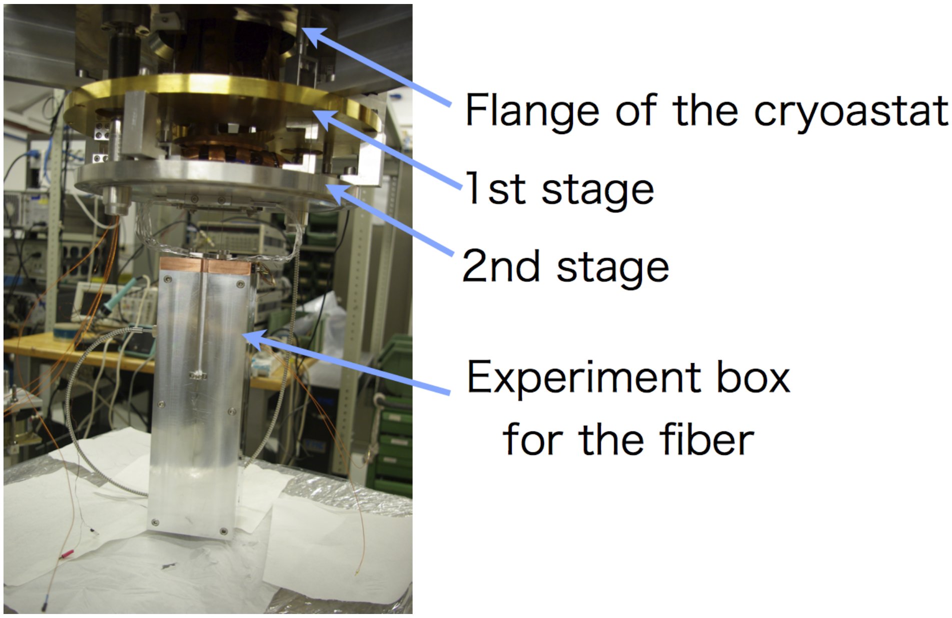

Figure 5.3: Experimental part of the cryostat we used for the mechanical loss measurement of sapphire fibers. Experiment box is suspended by three stages. The 1st stage in the picture is suspended from the top flange of the cryostat by three metal wires. The 2nd stage is suspended from the 1st stage by three metal wires. And the experiment box is suspended from the 2nd stage by two metal wires. In order to cool the experiment box, heat links made of pure aluminum are connected between the 2nd stage and the experiment box.

This cryostat originally has two stages for vibration isolation: the 1st stage is suspended from the flange of the chamber by three metal wires, and the 2nd stage is also suspended from the 1st stage by three metal wires. The stages are connected with a pulse tube cryogenic cooler by many soft copper heat links. The experiment box which holds not only the fiber but also the actuator and the sensor are suspended from the 2nd stage by two metal wires. The pictures of the box and the inside are shown in Fig.5.4. A schematic figure of the measurement system is shown in Fig.5.5.

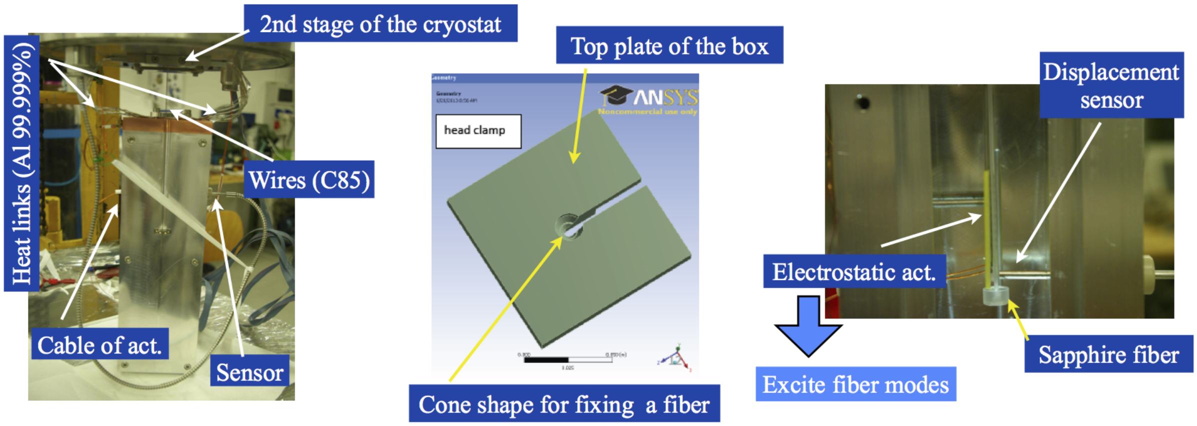

Figure 5.4: Experiment room for the mechanical loss measurement of the sapphire fibers. The left picture shows the view out of the experiment box which is suspended from the 2nd stage of the cryostat. The center figure is the drawing of the top plate of the box which holds the fiber. The right picture is the inside of the box. A fiber, an actuator and a sensor are there. The actuator and the sensor are not touched on the fiber.

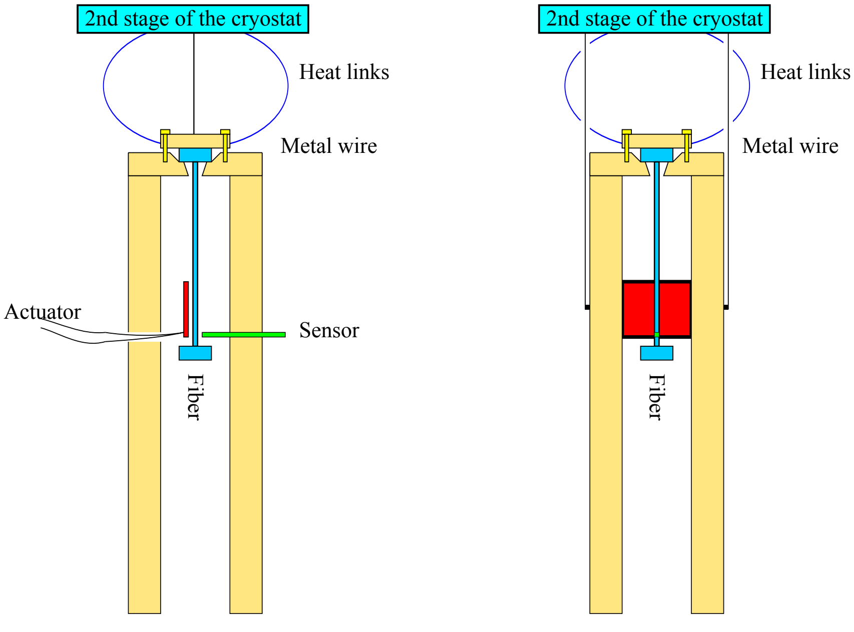

Side view

Front view

Figure 5.5: Schematic view of the fiber mechanical loss measurement setup. The experiment box is suspended from the 2nd stage of the cryostat. The heat links for cooling the sample is fixed between the sapphire head and the metal plate. The sapphire fiber is fixed at the upper head. An electrostatic actuator and a optical sensor are fixed in the experiment box.

The sapphire fiber was fixed on the copper top plate which has a cone shape part to put the fiber by a flat plate from the upper side. The actuator and the sensor were fixed on the wall of the box made of aluminum. In order to cool down this experiment box, the heat links were attached on the top of the box to connect with the 2nd stage of the cryostat. A temperature sensor was attached on this box to monitor the temperature.

5.1.2 Experiment

In this experiment, we excited the modes of the fiber by the electrostatic actuator and monitored the decay line of the motion by the sensor. We measured the mechanical loss from the cryogenic temperature to the room temperature. The lowest temperature was 18.5 K (for the type A fiber) and 16.5 K (for the type B fiber) which are in the operating temperature range (16 K - 20 K) of the fibers in the KAGRA cryogenic sapphire suspension.

Three modes were measured by the experiments. All of these modes could be predicted by a FEM simulation using ANSYS. Figure 5.6 shows the mode shapes calculated using ANSYS.

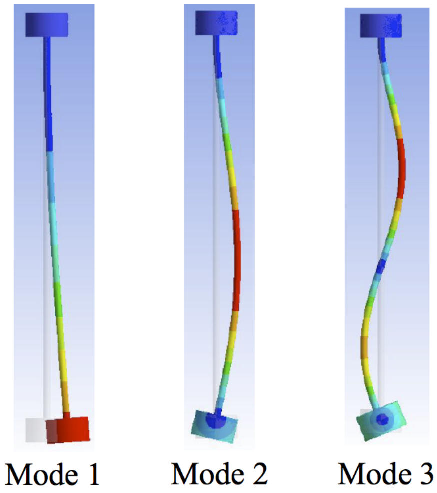

Figure 5.6: Mode shapes of a sapphire fiber. The 1st mode is 95 Hz, the 2nd mode is 1327Hz, and the 3rd mode is 3871Hz in the simulation.

The resonance frequencies of the simulation were 95 Hz, 1327 Hz and 3871 Hz, which are consistent within several percent with the measured frequency. The mechanical loss at room temperature is known to be dominated by the thermoelastic damping. (Equation (4.15))

An example of the decay curve is shown in Fig.5.7.

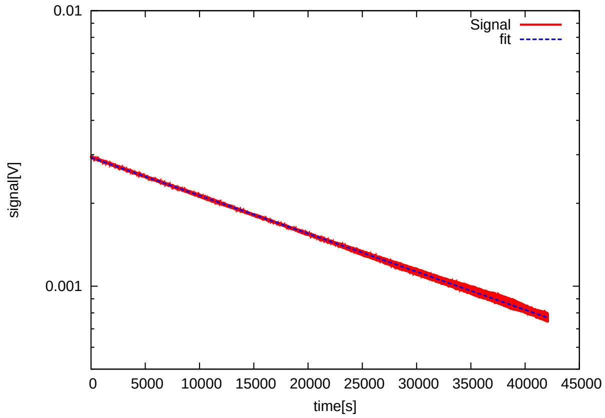

Figure 5.7: Example of the decay curve. The fiber of this data is non-monolithic fiber (type B fiber), the temperature was 16 K, the frequency was 88 Hz and the fitting result was $\phi = 1.2 \times 10^{-7}$. The fitting residual error was 0.02 %

The measurement only recorded the amplitude changes of the sine wave because if all data of the sine wave decay had been recorded, the storage would have been huge and the recording speed could have been slow.

The measurement result of the type A fiber which is the monolithic fiber is shown in Fig.5.8.

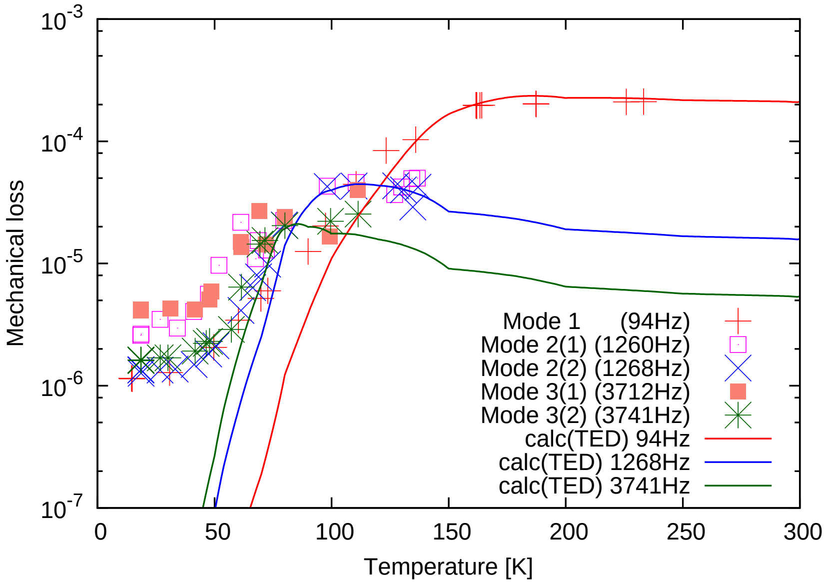

Figure 5.8: Measured mechanical loss of the type A fiber. Solid lines are calculated mechanical loss based on the thermoelastic damping (TED) which is considered to limit the mechanical loss at high temperatures.

The resonance frequency split was found in the second mode and the third mode.

These splits can be explained by the non-circular cross section of the fiber and the connection between the observation direction and the vibration directions. In this graph the calculated mechanical loss due to the thermoplastic damping are also plotted, which are consistent with the measurement results at the high temperature range. This fiber does not achieve the required value of the mechanical loss of the fiber which is $\phi_f < 2.0 \times 10^{-7}$.

In Fig.5.9, the measurement result of the type B fiber which is a non-monolithic fiber is shown.

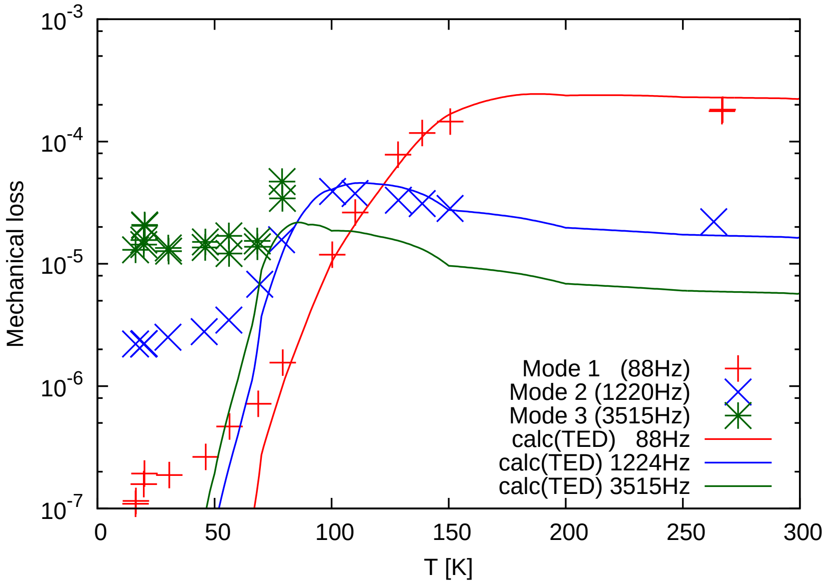

Figure 5.9: Measured mechanical loss of the type B fiber. Solid lines are calculated mechanical loss based on the thermoelastic damping (TED) which is considered to limit the mechanical loss at high temperatures.

At room temperature or in the high temperature range, the measurement result is consistent with the calculated result from the thermoelastic damping. This fiber could achieve the required value at low temperatures. The lowest mechanical loss was 1.1×10^{-7} at 16 K for the fist mode. We measured the loss value twice at this temperature, then the difference was $\sim 5\,\%$.

At the low temperature range, where the effect of the thermoelastic damping is low, other un-know effects appear to limit the mechanical loss. Effects from the measurement setup such as the reaction mass effect, explained in the section 4.3.2 and the loss at the fixing point of the fiber are the candidates. In a way these measurements give an upper limit for the mechanical loss. In the result of the type B fiber (non-monolithic fiber), the dependence on the frequency was observed in low temperatures. Because the frequency band of KAGRA is around 100 Hz, we can focus on the first mode.

The differences between these two fibers are the connection points between the thin fiber part and the heads, HEM or not and the polish (with thermo polish or without). From these measurement results, we can say the connection between the fiber and the heads of this type B fiber can not raise the mechanical loss above the requirement value around the most sensitive frequency band of KAGRA. Because the monolithic fiber had higher loss than that of the non-monolithic fiber, the manufacturing method HEM or the thermal polish or both can reduce the mechanical loss. The most emphasized points from these measurements is that the fiber which can achieve the required mechanical loss is manufacturable.

5.2 Indium bonding

Indium bonding will be used between the ear and the fiber head, and also between the blade and the fiber head to make a contact which can be debonded easily in the case that parts are broken. In order to measure the mechanical loss of bonding, the author and colleagues made a bonded sapphire sample and measure the mechanical loss of the sample.

To produce indium bonding we used two methods. One is to use the vacuum deposition technique to coat the bonding surface of the sapphire samples and put indium foil between the coated samples, and then heat it up to $\sim 200\,^{\circ}\mathrm{C}$ (indium bonding method 1). The other is just putting a piece of foil between the sapphire samples and heat it up to $\sim 200\,^{\circ}\mathrm{C}$ (indium bonding method 2). Using method 1 should be better because of the better contact between indium and sapphire. But even we use method 2, the heat extraction (and the strength) is enough, which is reported in latter chapters.

In order to measure the mechanical loss of indium bonding, we made a bonded sapphire sample and compared the mechanical loss with the reference sample which has the same shape as the bonded sample measured by the Jena group using the same apparatus as we used for the bonded samples. We measured the mechanical loss of the indium sample bonded by methods 1 and 2. For the HCB mechanical loss measurement, we used the same experimental setup.

5.2.1 Experimental setup

We procured three sapphire samples for this measurement from Impex [53]. Figure 5.10 is a picture of the samples.

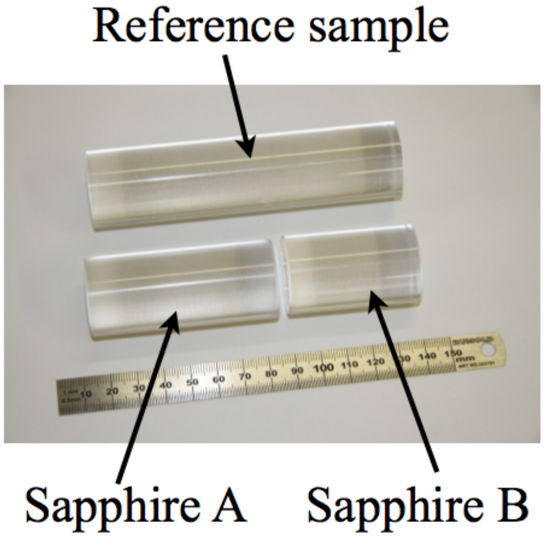

Figure 5.10: Sapphire samples for the mechanical loss measurement of bonding. The reference sample is 30 mm in diameter and 120 mm in length. Sapphire sample A has the same diameter and 70 mm length. Sapphire sample B has the same diameter and 50 mm length.

In order to estimate the mechanical loss, we need a measurement of a reference sample to compare the measured mechanical loss. The reference sapphire sample has 30 mm diameter and 120 mm length. The sapphire sample A and B have the same diameter, but 70 mm and 50 mm in length, respectively.

First we bonded the sapphire A and B together by indium bonding. In the case of bonding method 1, we deposited indium (∼300 nm) on the surface of the samples in advance. For bonding method 2, we did not deposit indium on the surface. We put the sample B on a heated plate and put an indium foil which had 0.1 mm thickness on the sample B. The sample A and a weight (∼ 1.7 kg was on the bond in total) were put on the indium bond to have a better contact at the bonding surface. Actually, in the case of bonding method 1, we did not need to put a foil between the samples, but in order to make a thicker bond which is easier to be measured, we used the foil. To keep a high temperature, a beaker was put to cover the sapphire. In order to monitor the temperature, we put a temperature sensor on the sapphire just above the indium layer. The picture is shown in Fig.5.11.

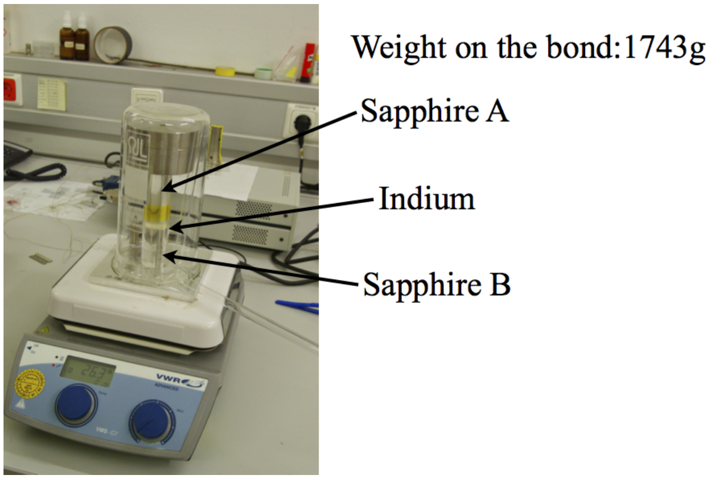

Figure 5.11: Indium bonding for the mechanical loss measurement. There is a temperature sensor on the sapphire A just above the indium layer.

After bonding, we checked the thickness of the bond by a microscope. The pictures taken with the microscope are shown in Fig.5.12.

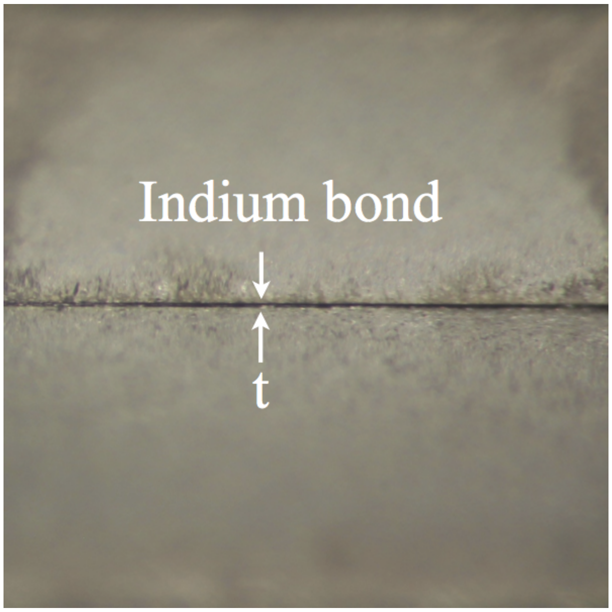

Figure 5.12: Microscopic view of the indium boding. The thickness was measured by counting the number of the pixels and comparing to a picture of a scale. (Bonding method 1)

The thickness of the indium bonding was estimated by counting the number of the pixels and comparing to the scale. In the result, the thicknesses were estimated as 14μm (method 1) and 8μm (method 2).

The cryostat we used was cooled by liquid nitrogen and liquid helium. The bonded sample was suspended in the cryostat. A schematic figure and a picture of the system are shown in Fig.5.13.

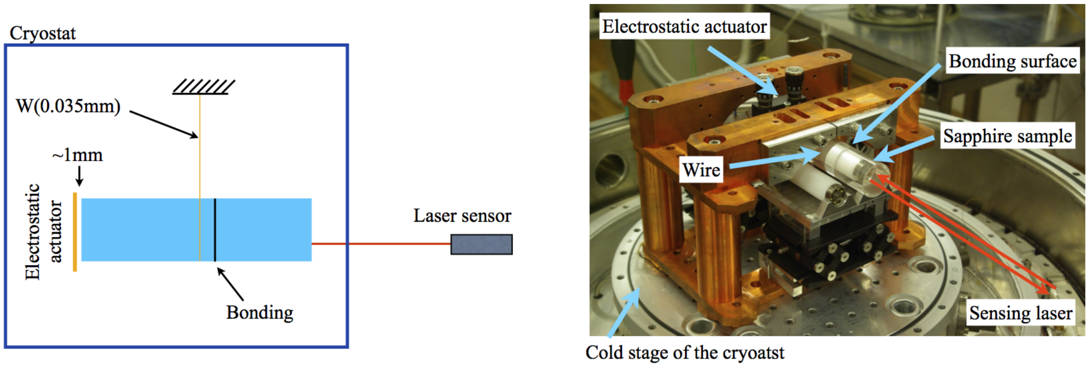

Figure 5.13: Measurement system for the mechanical loss of bonding. The cylinder monolithic (or bonded) sapphire sample is suspended from a rigid structure by a U shape wire. An electrostatic actuator face to the one of the faces of the sample. A laser sensor located outside the cryostat monitors the vibration of the sample.

The bonded sapphire sample was suspended using one tungsten wire whose diameter was 0.035 mm. The reason why the sapphire A and B are not the same size is to prevent this wire from touching the bonding. In order to excite resonance modes, an electrostatic actuator was used. For sensing the vibration, we used an interferometric laser sensor from outside the cryostat. Because this cryostat has double vacuum system, helium gas can be used to be the thermal contact gas in the experiment room. This is why we can cool down the sample which is suspended by only one thin wire.

5.2.2 Experiment

We used the actuator to excite the modes of the sample and monitored the decay curve. The mode we could measure is shown in Fig.5.14.

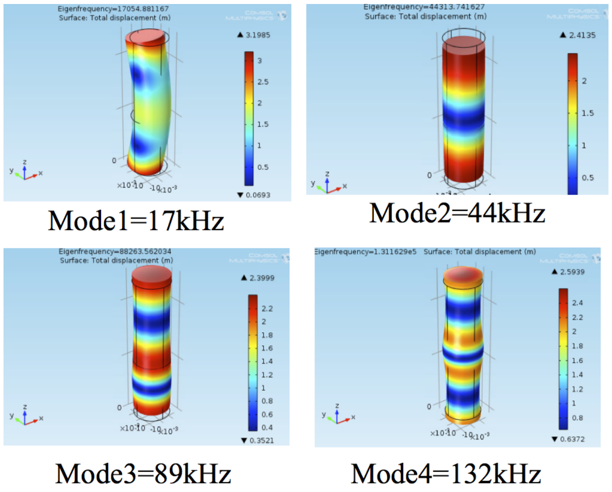

Mode1=17kHz

Mode2=44kHz

Mode3=89kHz

Mode4=132kHz

Figure 5.14: Mode shapes of the cylinder sapphire sample simulated by COMSOL.

In this simulation, we assumed that the effect from the bonding to the resonance frequency is small enough that we just could use a cylinder shape sapphire model to calculate the resonance frequency. The difference in frequency between the simulation and the measurement was several percent.

An example of the decay curve is shown in Fig.5.15.

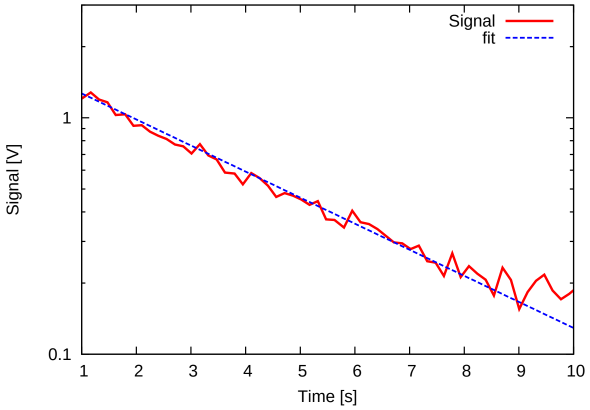

Figure 5.15: Example of the decay curve for the indium bonding.

The measured mechanical loss is shown in the Figs.5.16 and 5.17.

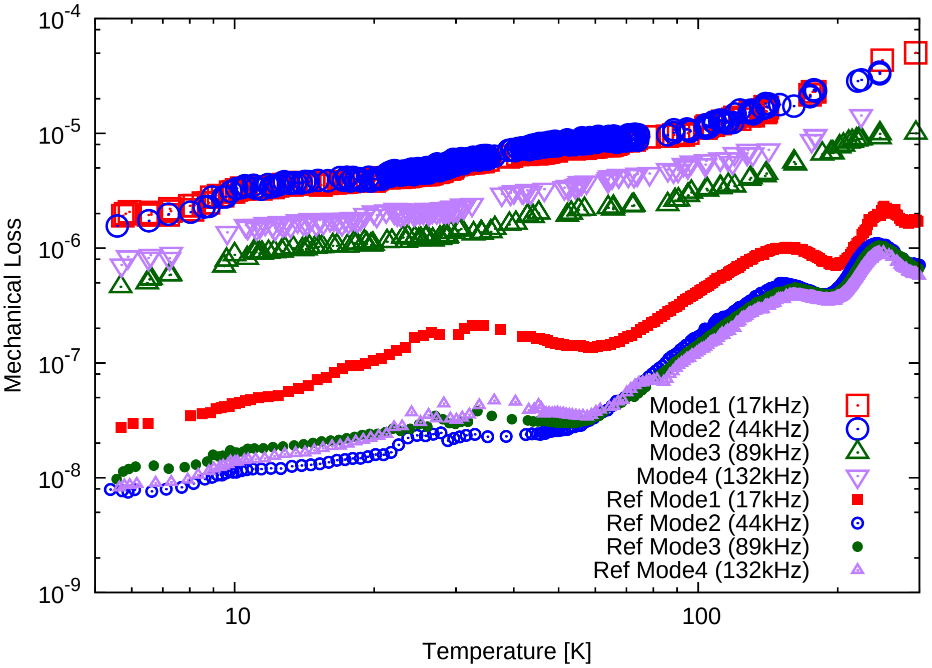

Figure 5.16: Measured mechanical loss of the bonded sapphire sample (bonding method 1) and the reference sample. The losses of the reference sample are much lesser than that of bonded sample. Mechanical loss of the bond can be calculated from this data.

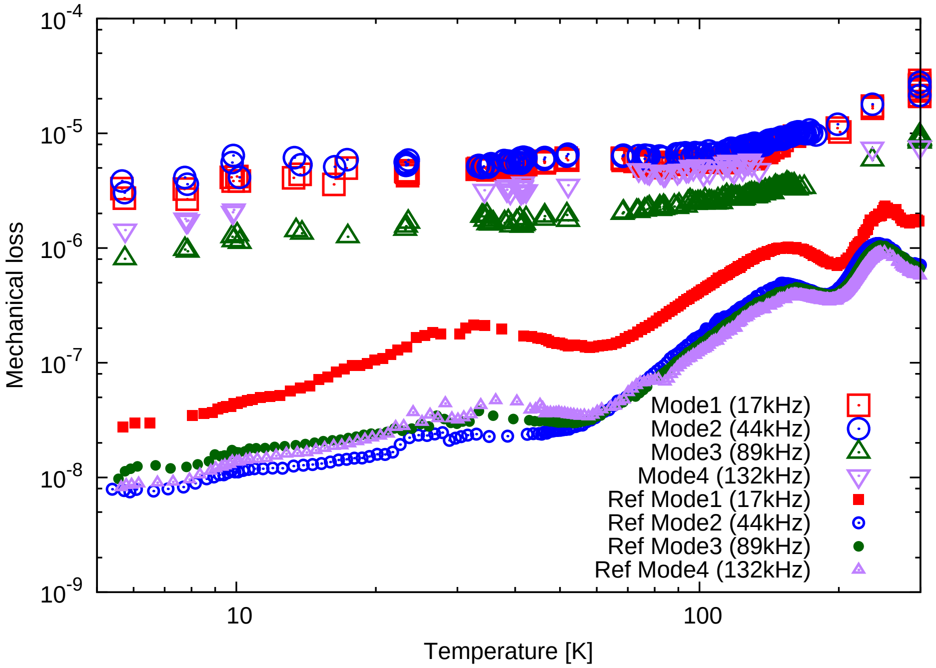

Figure 5.17: Measured mechanical loss of the bonded sapphire sample (bonding method 2) and the reference sample.

The mechanical loss of the reference sample measured by the Jena group is also plotted in the figure. Here the mechanical loss of the reference sample is much lower than that of the bonded samples.

The results shown in Figs.5.16 and 5.17 are only the mechanical loss of the bonded sapphire sample. What should be estimated is the mechanical loss of the bonding. So we needed to estimate the mechanical loss of the bonding from the measured data. The mechanical loss of the substrate $\phi_{\rm sub}$, bonding $\phi_{\rm B}$ and measured loss $\phi_{\rm mess}$ are related as,

$$\phi_{\rm meas} E_{\rm tot} = \phi_{\rm sub} E_{\rm sub} + \phi_{\rm B} E_{\rm B}, \tag{5.7}$$

where $E_{\rm tot}$ is the total elastic energy in the bonded sample under the mode, $E_{\rm sub}, E_{\rm B}$ mean the energy in the substrate and bonding, respectively. This equation indicates that the sum of the lost energy in the substrate and the bond is equal to the total lost energy. If we assume that the energy in bonding is much smaller than the total energy and the mechanical loss of substrate is much smaller than that of the measured value[1]:

$$\frac{E_{\rm B}}{E_{\rm tot}} \ll 1 \tag{5.8}$$

$$\frac{\phi_{\rm sub}}{\phi_{\rm meas}} \ll 1, \tag{5.9}$$

---

[1] Actually, the ratio of the energy in the bond to the energy in the substrate is about 10^{-3} to 1. The measured mechanical loss of the bonded sample is higher than the loss of the reference sample by 2 orders of magnitudes.

the mechanical loss of the bond ϕ_{B} can be written like the following.

$$\phi_{\mathrm{B}} = \frac{E_{\mathrm{tot}}}{E_{\mathrm{B}}}\phi_{\mathrm{meas}} \tag{5.10}$$

In order to estimate the loss of the bonding, the elastic energy ratio between the total and the bonding was calculated by using an FEM software COMSOL.

In the simulation by COMSOL, we assumed a sapphire cylinder and calculated the total energy and the energy density on the plane of the indium bonding. Then we multiplied the thickness of the indium of our sample by the energy density. The simulation results of the energy ratio are shown in Tables 5.1 and 5.2. These calculated ratios are different from the ratio of the length of the sapphire sample and the indium bond because the bond has different Young's modulus from the sapphire.

Table 5.1: Simulated energy ratio between the total and the bonding (bonding method 1)

Mode number	E_B/E_{tot}
1	1.4×10^{-3}
2	1.2×10^{-3}
3	3.1×10^{-4}
4	6.1×10^{-4}

Table 5.2: Simulated energy ratio between the total and the bonding (bonding method 2)

Mode number	E_B/E_{tot}
1	8.5×10^{-4}
2	7.1×10^{-4}
3	1.9×10^{-4}
4	3.7×10^{-4}

The mechanical loss values of the indium bonding were estimated based on this energy ratio. The result is shown in Figs.5.18 and 5.19.

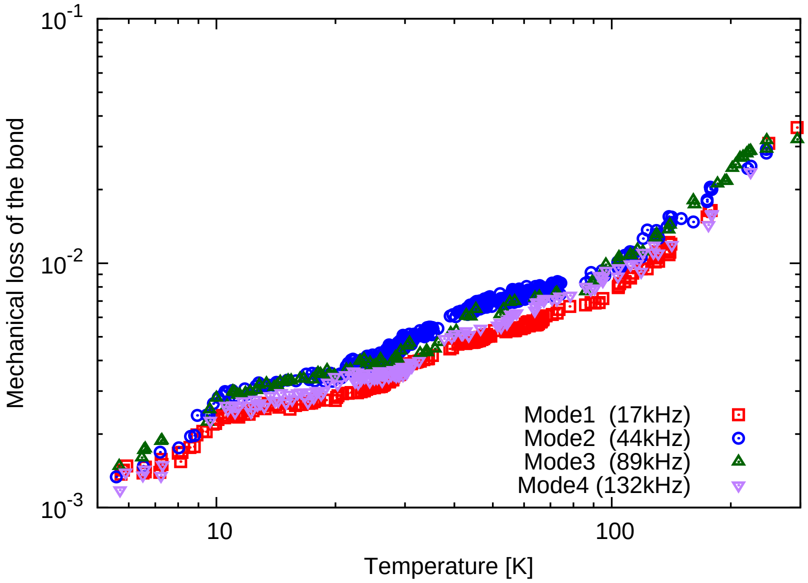

Figure 5.18: Mechanical loss of indium bonding (Bonding method 1). At the 20 K, the measured mechanical losses are smaller than the requirement of the mechanical loss of this bond, which is 1.5×10^{-2}.

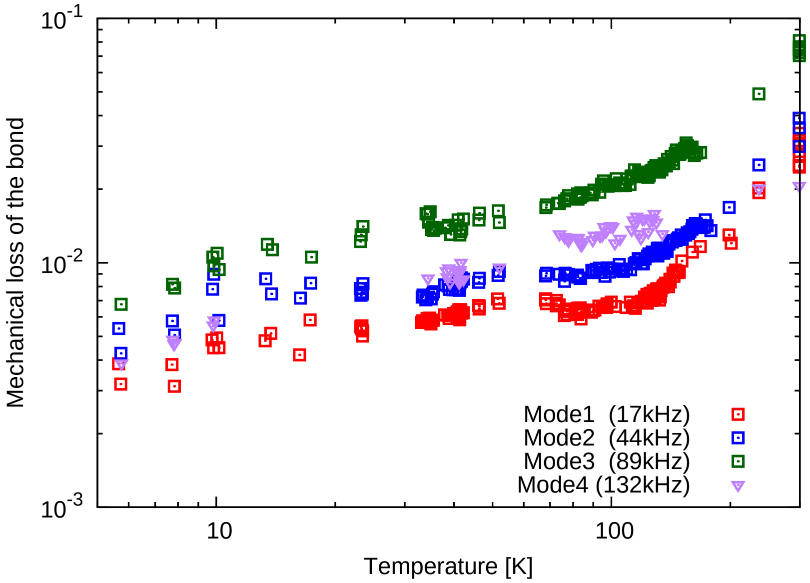

Figure 5.19: Mechanical loss of indium bonding (Bonding method 2). Even if initial evaporation coating was not used, the mechanical loss of the indium bond is smaller than the requirement of $1.5 \times 10^{(} - 2)$ at 20K.

As the result, the mechanical losses of the indium bonding at 20 K $\phi_{\mathrm{In\_meas1}}$ and $\phi_{\mathrm{In\_meas2}}$ are

$$\phi_{\mathrm{In\_meas1}} = (3.1 \pm 0.6) \times 10^{-3} \tag{5.11}$$

and

$$\phi_{\mathrm{In\_meas2}} < 1.4 \times 10^{-2}. \tag{5.12}$$

The requirement of this bond is 1.5×10^{-2}. Therefore, both of them satisfy the requirement. The present result shows, however, that it is better to use the evaporation technique with the objective of being on the safe side. In order to make a 1 μm thickness indium bonding, the evaporation technique can be used. Using a foil is also possible in principle, even though the handling is not easy. Method 1 is assumed in the following discussion.

5.3 HCB

In order to connect the ear against the mirror to hold the mirror, a bonding technique named Hydroxid Catalysis Bonding (HCB) will be applied. There are no measurements of the mechanical loss for this HCB at low temperatures. Thus the author and colleagues measured it using the same method as the indium bonding measurement.

To measure the mechanical loss, we bonded two sapphire samples which are exactly the same samples with the indium bonding using the same mount of solution reported in the reference paper [80] which shows the thickness of the bond is ~ 60 nm. Here we assume that the thickness of our bonded sample also has 60 nm thickness. If the thickness is thicker than this value, it indicates that we overestimate the loss of the bond. So we are on the safe side if we use 60 nm thickness for the energy calculation explained below.

In order to form a strong bonding of HCB, we need to wait for ∼four weeks to evaporate H_2O in the bonding after the attaching process. This curing time affects its strength. In the case of silica-silica bonding, the maximum strength was measured after bonding for ∼four weeks [59]. The strength behavior depending on the curing time for the case of sapphire has not yet been studied. We also waited for at least ∼four weeks tentatively for every bonding we did. In the previous studies, like the one by T. Suzuki et al. [20], KOH solution was used for the sapphire bonding. As R. Douglas et al. reported on their paper [60], Na_2SiO_3 solution has a much high strength for the sapphire sample. In their paper they measured the tensile strength at 77 K and room temperature without any thermal cycles. Therefore, bonding solution we used is sodium silicate solution whose chemical formula is $Na_2O(SiO_2)_x \cdot xH_2O$ produced by SIGMA-ALDRICH, which is reported as a high strength solution for the sapphire sample in their paper.

Our bonding procedure is the followings.

1. Clean the sapphire surface using abrasive soap (Refre Clin made by Neo Star Co.).
2. Use purified water to rinse the soap off.
3. Repeat 1 and 2.
4. Clean the sapphire surface using Sodium Hydrogen Carbonate ($NaHCO_3$).
5. Use purified water to rinse the soap off.
6. Repeat 4 and 5.
7. Put diluted solution (Volume ratio; solution : $H_2O = 1 : 6$) on the bonding surface.
8. Put the other sapphire on the surface

We used $0.4\,\mu$l diluted solution for each cm^2.

5.3.1 Experiment

The experimental setup for this HCB mechanical loss measurement is the same as the one for the indium bonding. So, in this section the description of the measurement system is skipped.

The modes we observed are shown in Fig.5.20.

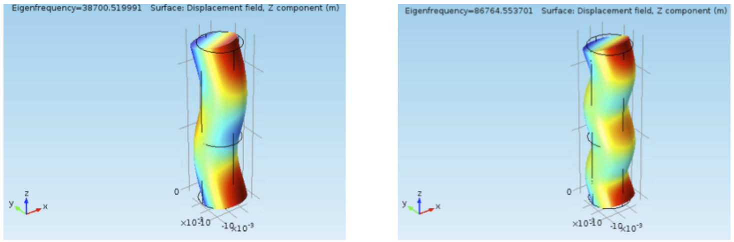

Mode1=38kHz Mode2=87kHz

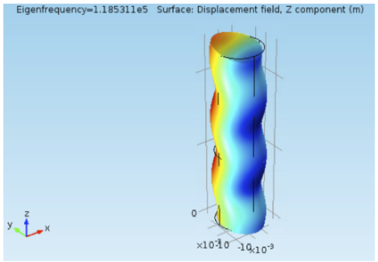

Mode3=118kHz

Figure 5.20: Mode shapes of the sample simulated by COMSOL.

The frequency difference between the measurement and this simulation was several percent.

This time, because the decay curve went down quickly, the method to estimate the mechanical loss using spectrum measurement was also applied. Examples of the spectrum and the decay curve are shown in Fig.5.21 and 5.22.

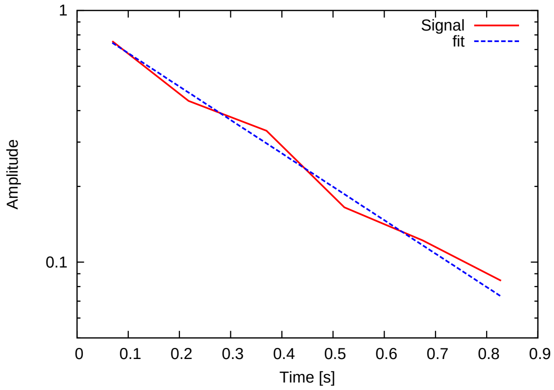

Figure 5.21: Measured decay curve and the fitting result for HCB sample.

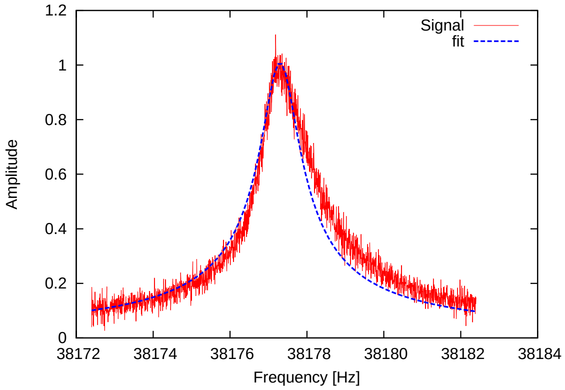

Figure 5.22: Spectrum and the fitting result for HCB sample.

These example data in Figs.5.21 and 5.22 were measured at 20.1 K and 20.2 K. The fitting results of the mechanical loss are $(2.6 \pm 0.2) \times 10^{-5}$ in the case of decay curve and $(2.58 \pm 0.03) \times 10^{-5}$ in the case of spectrum measurement. These two methods are consistent with each other within the uncertainties

The measured mechanical loss of the bonded sapphire sample is shown in Fig.5.23.

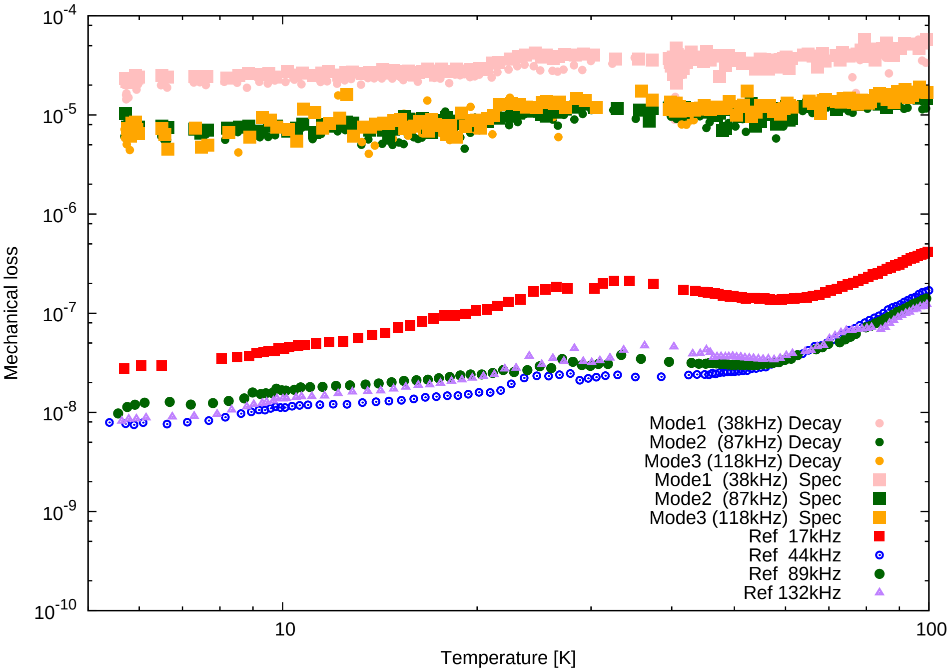

Figure 5.23: Measured mechanical loss of the HCB sample and the reference sample. The mechanical losses of the reference sample are much smaller than that of the bonded sample. The mechanical loss of the bond can be calculated from this data.

In this case, the condition of Eqs.(5.8) and (5.9) can also be applied and we calculated the energy ration for the measured resonance modes by COMSOL:

Table 5.3: Simulated energy ratio between in the total and in the bonding (HCB sample)

Mode number	E_B/E_{tot}
1	1.8×10^{-5}
2	1.3×10^{-5}
3	2.4×10^{-5}

The mechanical loss of the HCB was estimated. The result is shown in Fig.5.24.

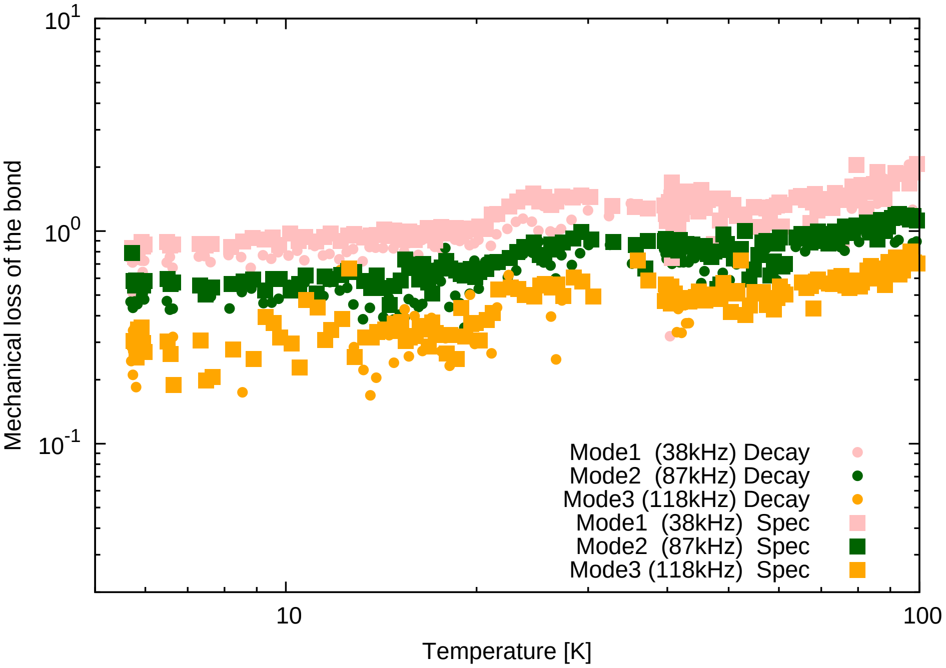

Figure 5.24: Mechanical loss of the HCB. The requirement is 1.0 for this bond. The maximum mechanical loss at 20K is same as this value.

According to this result, the mechanical loss of the HCB at 20 K is 1.0 at most. As described in Chapter 4.3.2, the requirement of mechanical loss of HCB is 1.0. So the HCB barely satisfies the requirement even if we take the safe side for KAGRA.

Chapter 6

Thermal conductivity measurement

In order to keep the main mirror of KAGRA at low temperatures during the interferometer operation, the heat from the mirror and coating that absorb the main laser beam should be extracted. The heat will be extracted through the sapphire suspension, which contains not only sapphire bulk, but also the bondings and the sapphire fibers. These can be heat resistances. In this chapter, the heat extraction test of the sapphire fibers and the bonding techniques are reported.

6.1 Sapphire fiber

The thinnest part of the cryogenic sapphire suspension system is the sapphire fibers. As described by T. Tomaru et al. in their paper [81], the size effect on the thermal conductivity of sapphire fibers exists. Therefore, the thermal conductivity of the sapphire fibers for KAGRA should be measured. There were not any reports about the heat extraction using a sapphire fiber whose diameter is 1.6 mm with heads. The contents in this section are published in a scientific journal, Class. Quantum Grav. [78].

6.1.1 Sapphire fiber samples

The author and colleagues measured three kinds of the fiber: type A fiber, type B fiber and type C fiber [1]. Type A fiber is a monolithic fiber manufactured from one sapphire crystal and without any surface treatment like thermo-polish. (This fiber is addressed as (1)-(4) in this section.) Type B fiber is a fiber manufactured by Heat Exchanger Method (HEM) and thermo-polished. The fiber heads are connected by plasma-welding. (This type of fibers is addressed as (i)) Type C fiber is the first-generation fiber for us, which was manufactured from the monolithic head with 10 mm neck. Thin fiber part was grown from the neck. Finally the other head was jointed by the plasma-welding same as the type B fiber. (This type fibers are addressed as (a) and (b))

---

[1] Data analysis and simulation for this fiber heat extraction measurement were performed by collaborators of the Jena group and a collaborator in ICRR.

6.1.2 Experimental setup

A schematic view of the experiment setup is shown in Fig.6.1.

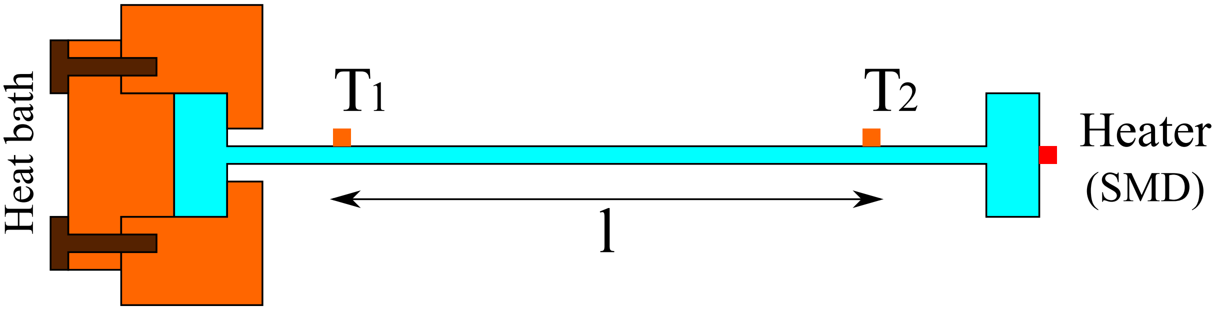

Figure 6.1: Thermal conductivity measurement setup for the sapphire fibers. The total length of the fiber sample is 10 cm. A small resistor is attached on the one head of the fiber. Two thermometers are attached on the fiber to monitor the temperature gradient wrong the fiber.

One of the heads was fixed against a copper heat bath whose temperature was controlled. Two temperature sensors (Lakeshore, DT-670) were attached on the fiber using copper blocks whose contact length with the fiber was 3 mm. The distance between the sensors were in a range between 47 mm and 51 mm. A small heater which was a Surface Mounted Device (SMD) resistor with 1 kΩ was attached on the free head to produce a heat load to the fiber. The heat power ΔP through the fiber and the temperature difference ΔT can be described by

$$\Delta P = \frac{A}{l}\kappa\Delta T, \tag{6.1}$$

where A, l and κ are the cross area, the length and the heat conductivity of the fiber. We applied several different powers, and then measured the temperature difference between the two sensors and estimate κ from the gradient of this equation. The measurement error of κ was estimated to be a maximum value of ±10 % mainly from the fiber diameter of ±0.05 mm and the distance between the temperature sensors of ±0.5 mm.

6.1.3 Measurement result

The measurement results are shown in Fig.6.2.

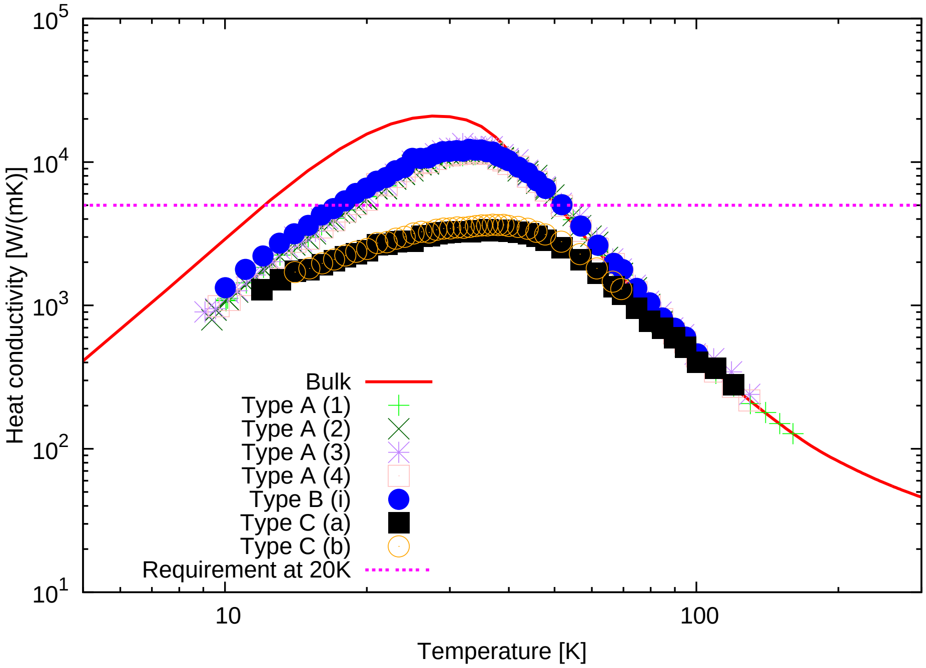

Figure 6.2: Measured thermal conductivity of sapphire fibers. Three kinds of fiber were measured. The requirement at 20 K is 5000 W/m/K. Type A and B had enough thermal conductivity but the type C fibers did not have enough conductivity.

At 20 K, type A fibers were in a range between 5400 and 5850 W/m/K and type B was 6600 W/m/K, which are over the requirement value 5000 W/m/K. The type C fibers did not have enough conductivity. Therefore type A or B fibers are suitable for the fibers of KAGRA sapphire suspension in terms of heat conductivity.

6.1.4 Heat extraction test

The author and colleagues also had a heat extraction test for the fiber. We kept the temperature of the heat sink at 16 K which is the same temperature as the intermediate mass. Then we increased the small heater power up to 1 W to demonstrate the power by the KAGRA mirror. The measured temperature on the top of the head, which the small heater was attached to, are shown in Fig.6.3.

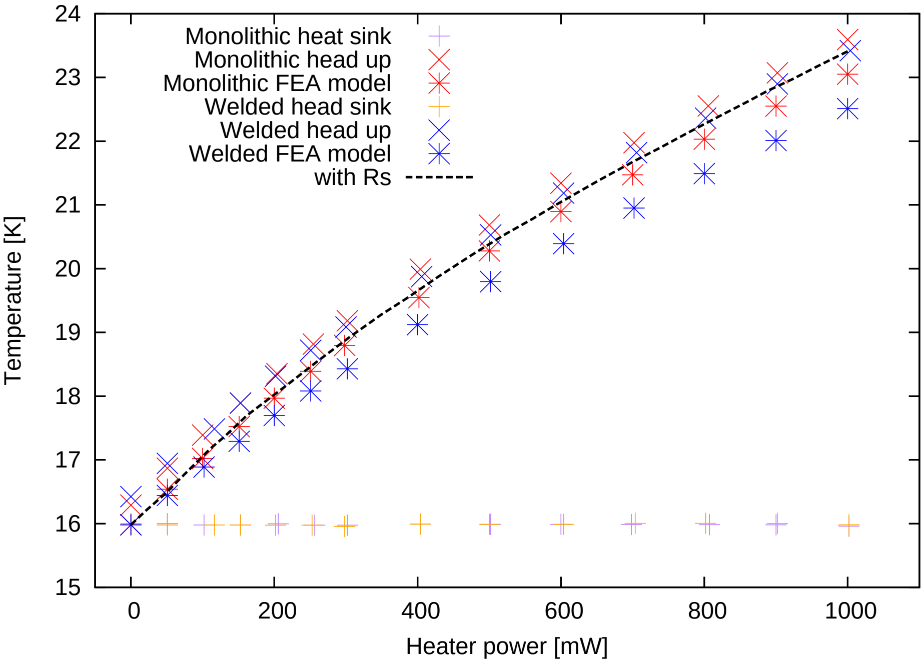

Figure 6.3: Temperature at the head of the fiber when power was applied on the head. “Monolithic” indicates the type C fiber and “welded” corresponds to the type B fiber. The results of Finite Element Analysis (FEA) are also shown in the figure. A simulation with a thin thermally resistive layer $R_s \sim 0.1...0.2\,\mathrm{K\,cm^2/W}$ between the fiber and the head is also plotted in this graph.

In this figure, the result calculated by a Finite Element Analysis is also plotted. The dashed line in the graph shows a simulation with a thin thermally resistive layer $R_s \sim 0.1...0.2\,\mathrm{K\,cm^2/W}$ between the fiber and the head. Since the thin fiber length was 85 mm for the measurement, we have to look at 490 mW point because one real fiber of KAGRA should transfer 138 mW with the 300 mm length. Both of the fiber heads showed about 20 K at this heating power. This suggests that in the real KAGRA case, the mirror would be 20 K during the operation. This also shows that the mirror absorption should be lower than 30 $\mathrm{ppm\,cm^{-1}}$ and the absorption of the coating should be lower than 0.5 ppm in order to keep the mirror temperature at 20 K.

6.2 Indium bonding

In order to estimate the influence on the heat extraction caused by the indium bonding, the heat conductivity of bonded sapphire samples was measured. The sapphire samples are 5 mm × 5 mm × 50 mm in size. The author and colleagues bonded two samples together to make a 100 mm long bonded sample. Here we measured the thermal conductivity of the bonded sapphire samples by two temperature sensors on the sample, then to judge the heat extraction, we calculated the value of κ/l, where κ is the thermal conductivity of the bonded sample and l is the distance between temperature sensors. This ratio can be given by

$$\frac{\kappa}{l} = \frac{1}{A}\frac{\Delta P}{\Delta T}, \tag{6.2}$$

which is the same as Eq.(4.49).

6.2.1 Experimental setup

In order to measure the heat conductance κ, we attached two temperature sensors on the bonded sample. A schematic figure of the setup and a picture of the assembled sample are shown in the Fig.6.4.

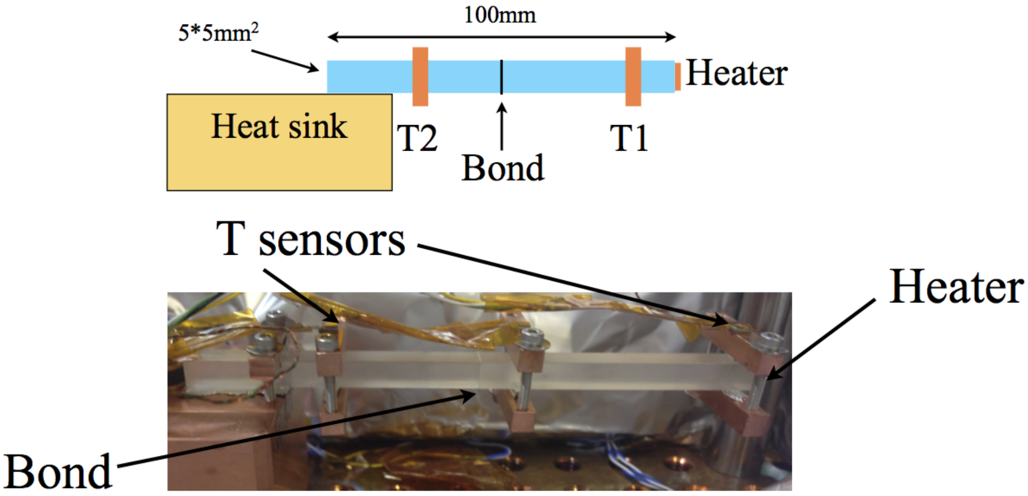

Figure 6.4: Setup for the thermal conductivity measurement of the bonded sapphire sample. A small resistor heater is attached on the end of the bonded sample. Two thermometers are on the sample to monitor the thermal gradient.

There is a heater attached on the end of the sample to make some heat flow. The thermal conductivity of this bonded sample can be written like the following.

$$\kappa = \frac{l}{A}\frac{\Delta P}{\Delta T}, \tag{6.3}$$

where A and l are the cross area ($5\,\mathrm{mm} \times 5\,\mathrm{mm}$) and the distance between the temperature sensors. We used a small heater (SMD resistance) on the top of the sample to change ΔP and measured the temperature difference ΔT by the two sensors. Actually we changed the input power[2] by three or five steps and measured the temperature differences, and estimated κ. The other end of the sample was attached on the copper block which was connected with a pulse tube cryocooler. A heater was also attached on the copper block to control the sample temperature in order to measure κ at several temperature points.

The temperature sensors were Cernox thermometers from Lake Shore [82]. While these sensors were calibrated by a diode temperature sensor, the error of the reading temperature was assumed to be $\sim 10\,\mathrm{mK}$. For this measurement, the absolute temperature value is not important, but the readout behavior between the two sensors are important. Figure 6.5 shows the error, which we assumed.

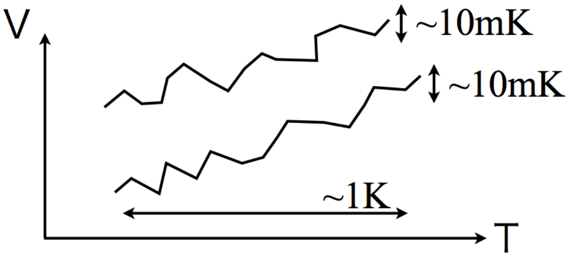

Figure 6.5: Schematic diagram of the temperature measurement error. We assume the following: the baselines of the readout voltage from two thermometers are parallel to each other but the readout fluctuation around the baseline is ~10 mK in terms of temperature.

In an ideal case, two thermometers should show exactly the same voltage at the temperature: the two lines must be straight (in a small temperature range) and identical. In the reality, it will not happen. But even if the two straight lines have some offset relative to each other, the measurement will not be affected by the offset error. If the readout has an error indicated in Fig.6.5, the measurement will have uncertainties in the estimate of κ. In the analysis, we assumed this uncertainty to be $\sim 10\,\mathrm{mK}$.

---

[2] The maximum input power should be changed at each measurement temperature because the thermal conductivity changes depend on the temperature.

6.2.2 Experiment

The measured result of κ of the sapphire sample with bonding is shown in Fig.6.6

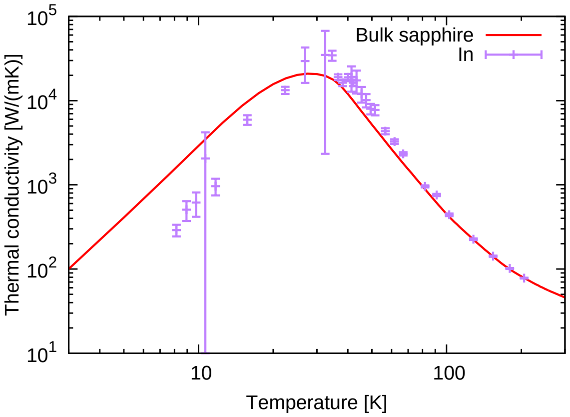

Figure 6.6: Thermal conductivity of the indium bonding sapphire sample. Data points at 13.5K and 32.2K have large error bar because the input power was small then the temperature gradient was small.

In Fig.6.6, the thermal conductivity of a bulk sapphire is also plotted [83]. At the highest thermal conductivity point, $\Delta T \sim 30\,\mathrm{mK}$ was measured in the case of $\Delta P =$ 1.3W at 30 K. This suggests that even if a very high power like 1 W was input, the temperature difference between the ends of the sample would be only 30 mK. Because in the KAGRA cryogenic sapphire suspension, the area of the indium bonding will be much larger (∼16 times) and the power which has to be extracted is much lower (∼10 %) , the temperature gradient would be much smaller. Finally, the value of κ/l is shown in Fig.6.7. ($l = 66.0\,\mathrm{mm}$)

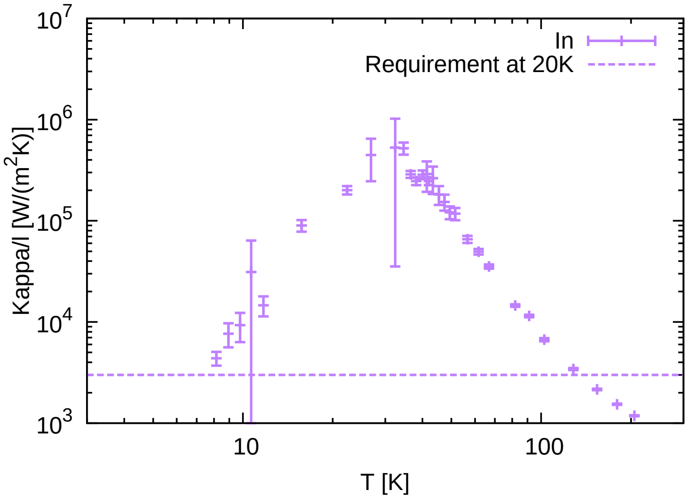

Figure 6.7: κ/l in the case of the indium bonded sample. A requirement value at 20 K is also plotted. The measured value has much higher value than the requirement.

The requirement of this κ/l, which is $3000\,\mathrm{W/m^2/K}$, is also shown in this graph. According to this result, the indium bonding can be applied without any problems in terms of the heat extraction.

6.3 HCB

The same measurement and analysis of HCB sample as the indium bonding was performed. In this section, the experimental setup is skipped because it is the same as the indium bonding.

6.3.1 Experiment

At first, the measurement results of the thermal conductivity of the HCB sapphire sample are shown in Fig.6.8.

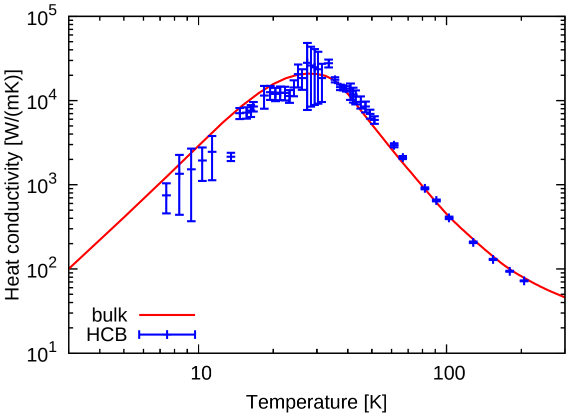

Figure 6.8: Thermal conductivity of the HCB sapphire sample.

According to this graph, the bonded sample by HCB had almost the same thermal conductivity as the bulk sapphire. In the temperature below the 30 K peak, measured values are a little lower than the bulk value. At the highest thermal conductivity temperature, when we entered 1.3 W power into the small heater on the top of the sample, measured temperature gradient was 50 mK. In the same way as the indium bonding sample, for the real KAGRA case, the power, which should be extracted, is only 20 % of this power and the area of the bond is $\sim$ 100 times larger than this sample. Hence, the temperature difference across the HCB in the KAGRA sapphire suspension should not exceed the requirement value 0.1 K during the main interferometer operation.

In order to check the results more clearly, the graph of κ/l is shown in Fig.6.9.

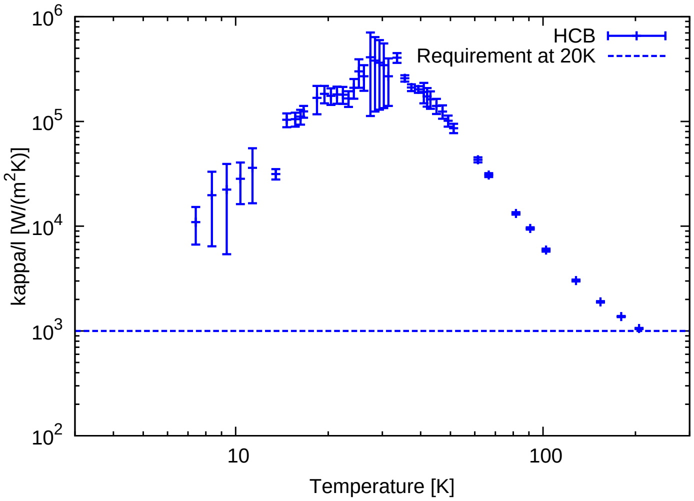

Figure 6.9: κ/l of the HCB sapphire sample and the requirement. The measured value has much higher value than the requirement.

The measured values of κ/l were much higher than the requirement at 20 K.

Chapter 7

Strength test

In this chapter mainly the strength test for the HCB is reported because the strength of this bonding technique after thermal cycling has not been reported. Also a quick strength test at room temperature of indium bonding is reported. It should be noted that because this bonding will not hold anything, a strength requirement is not necessary for this bonding technique.

7.1 Hydroxide-catalysis bonding -HCB-

For the bond between the mirror and the ear, each bond should hold 12 kg because the weight of the mass is 22.6 kg. A FEM simulation was performed to estimate the stress on the bond, suggesting that it was 0.43 MPa. In order to be on the safe side, 1 MPa is set to be the strength required value for HCB. Moreover, the cryogenic payload will experience cooling cycles many times from the installation or maintenances. One thermal cycle takes about three months including the time spent at room temperature. One or two thermal cycles for one year is a realistic or a maximum frequency because the observation also should be performed. If the suspension experiences two thermal cycles per one year and has a ten-year lifetime, the bonding will experience 20 thermal cycles. The strength tests after 10 and 20 thermal cycles were performed.

7.1.1 Samples

30 bonded samples (Fig.7.1) were prepared.

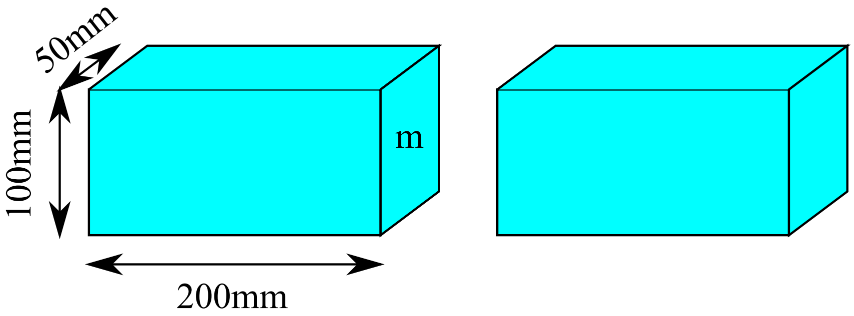

Figure 7.1: Size of the HCB samples for the strength test.

After curing time (two months), 20 bonded samples started the thermal cycle. We used a pulse tube cryocooler to cool down the samples to 20K and warmed it up to room temperature. One cycle takes one day. Moreover, we put some samples on a heated plate to raise the temperature up to 200 °C and kept for 30 min. Table 7.1 summarizes the number of bonded sapphire pairs of each condition.

Table 7.1: HCB strength sample

Cooling cycle	200 degree experience (30 min)	No 200 degree experience
0	3 pairs	7 pairs
10	2 pairs	8 pairs
20	2 pairs	8 pairs

Figure 7.2 shows the temperature change of the HCB sample during the thermal cycle. It took about one month to finish all the thermal cycling.

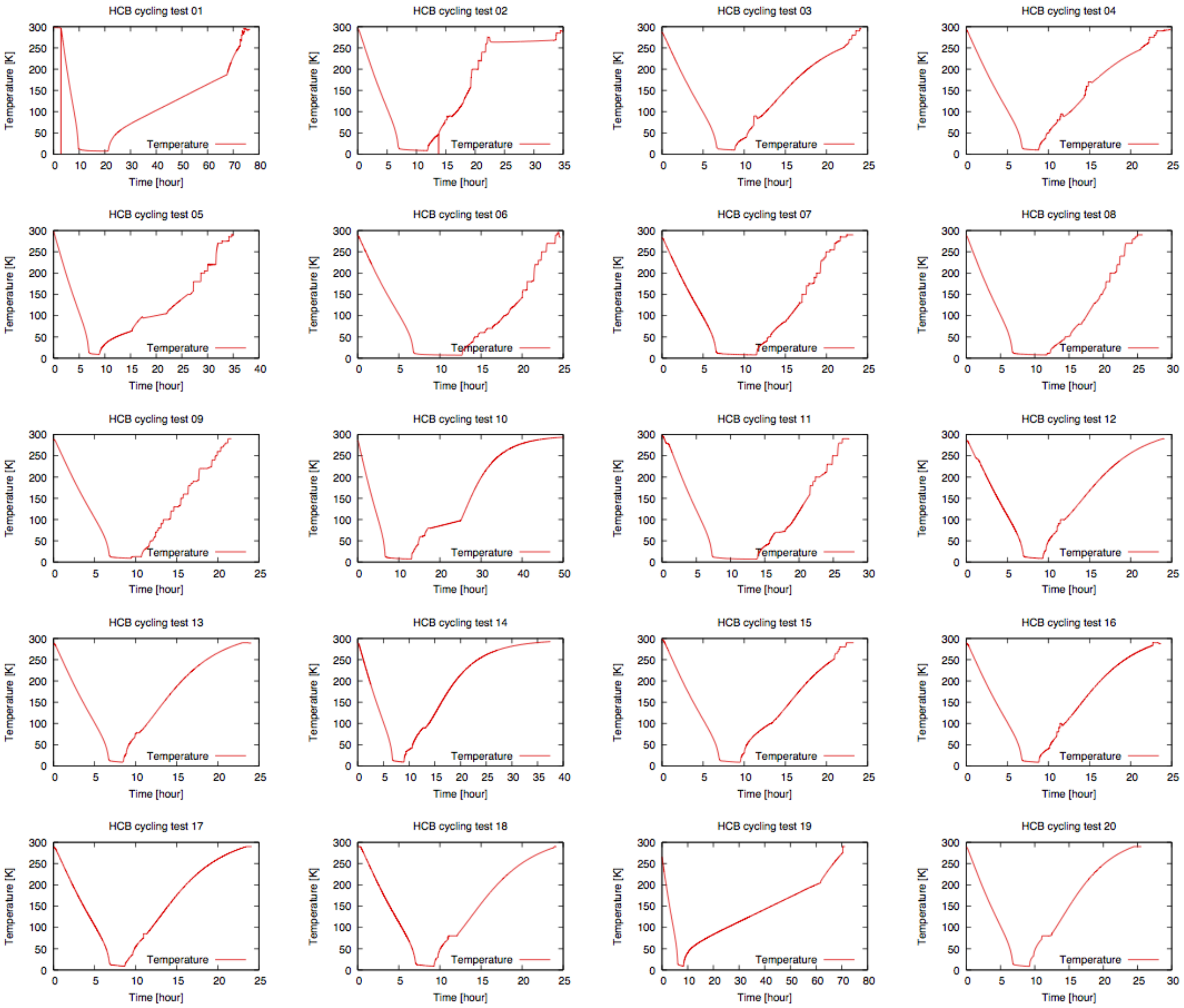

Figure 7.2: Temperature change for every thermal cycle. Normally one cycle took one day.

7.1.2 Experiment

Experimental apparatuses are shown in Figs.7.3 and 7.4. For each sample, we immerse it in liquid He and measured the breaking stress.

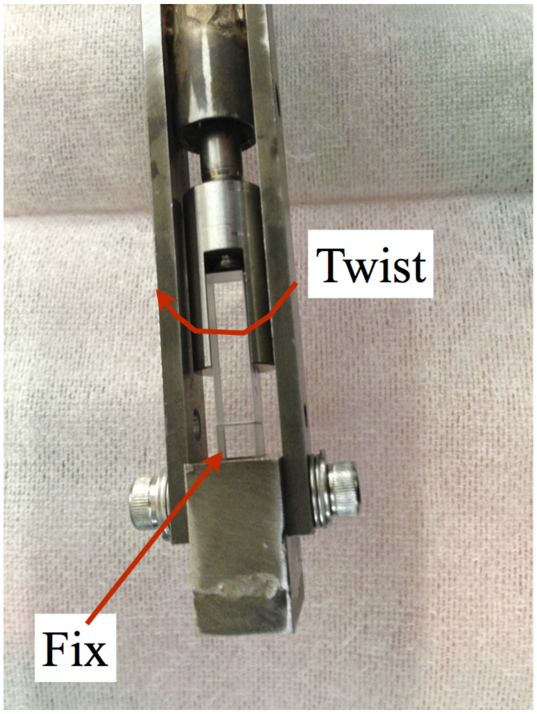

Figure 7.3: Strength test system. Lower sapphire block was fixed, then a torque was applied to the upper block.

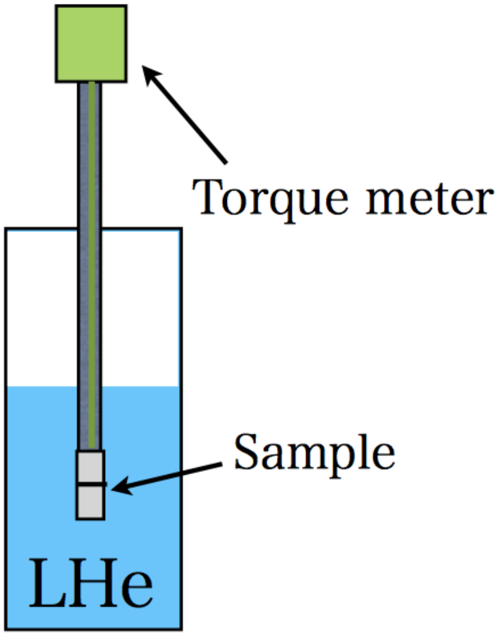

Figure 7.4: Strength test schematic figure. The bonded sample was soaked in liquid helium and tested.

A torque meter (DI-9F-IP5 made by CEDAR: SUGISAKI METER CO.) was used to measure the maximum torque when we twisted the sample. Appendix A shows the method to estimate the maximum shear strength. A schematic view together with the parameters in the measurement are shown in Fig.7.5. τ_{max} is the maximum shear stress at each point on the bonding surface. The corner of the bonding surface was assumed to have the maximum value.

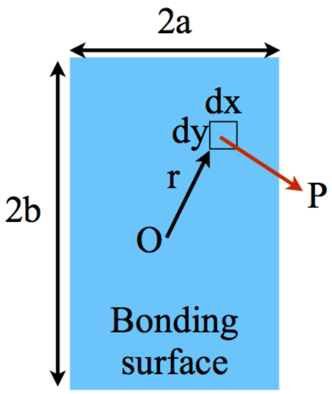

Figure 7.5: Parameters for calculating the maximum stress.

The maximum shear stress on the bonding surface τ_{max} can be expressed like the following. (Appendix A)

$$\tau_{max} = \frac{T}{\int (x^2 + y^2)\mathrm{dxdy}}\sqrt{a^2 + b^2} \tag{7.1}$$

Characters a, b mean the half of the two length of the bonding surface. In the case of our sample, the bonding surface was a square (5mm × 10mm). Therefore,

$$\tau_{max}\,[\mathrm{Pa}] = 1.1 \times 10^7\,[\mathrm{m}^{-3}] \times \mathrm{T}\,[\mathrm{Nm}]. \tag{7.2}$$

The maximum shear strength we could measure was 53 MPa because the maximum torque could be measured by the torque meter was 5 Nm. The result is shown in Fig.7.6.

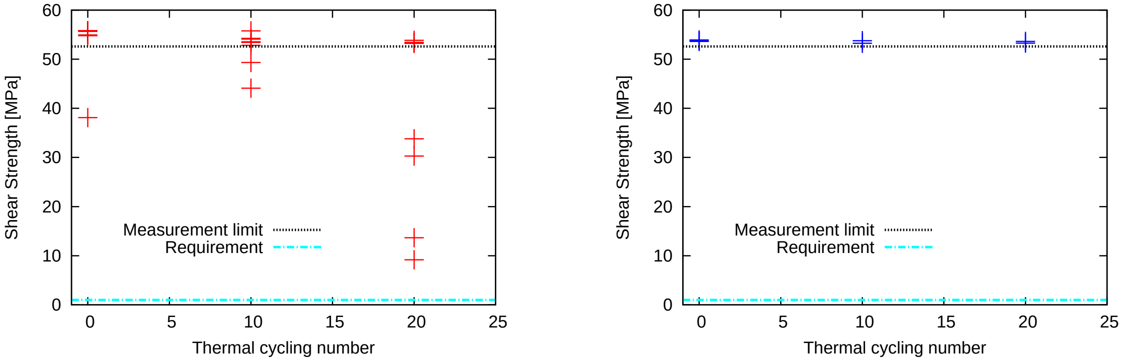

Figure 7.6: Result of the shear strength test of HCB. Black line is the measurement limit (53 MPa) because of the torque meter. Light blue line is the requirement: 1 MPa. Left graph shows the result of samples which have no experience of 200 °C. Right graph is the result of samples which were kept 200 °C for 30 minutes after thermal cycles. All of the samples have enough strength.

The black dashed line in Fig.7.6 shows this lower limit. Many data points are located above the measurement limit line, since those samples survived the strength test. For them, we were only able to evaluate the lowest strength. The data of the broken samples, suggest the degradation of HCB caused by the thermal cycling. Nevertheless, even the weakest sample whose strength was 9.1 MPa has a sufficient margin from the requirement of 1 MPa. Moreover, all of the samples which experienced 200 degree heating survived. Heating may potentially enhance the strength of HCB.

7.2 Indium bonding

Even though there is no strength required value for indium bonding because the indium bonding will not support any mass, a very easy strength test was performed at room temperature to complete the measurement.

The size of the bonded sample was the same as the thermal conductivity measurement sample. The experiment setup is shown in Fig.7.7.

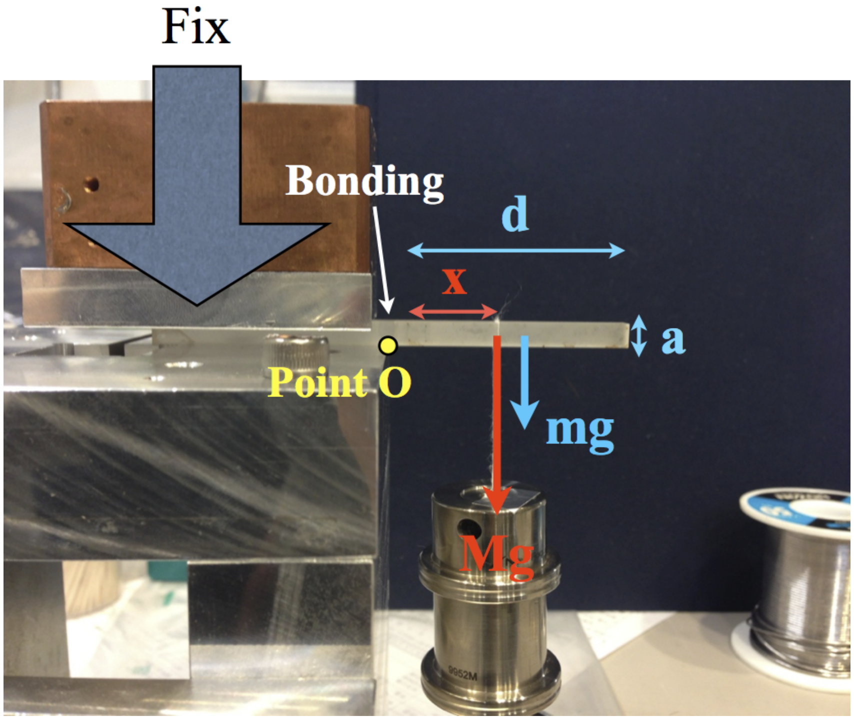

Figure 7.7: Experimental setup for the strength test of indium bonding at room temperature. Left sapphire sample was fixed on a stage. A mass which has a mass M is suspended at a point on the right sapphire sample. The distance between bonding point O and the suspension point is x.

The author and colleagues fixed one side of the bonded sample and put weight on the other side, then checked the maximum torque on the bond face. If we assume the maximum stress P_{max} on the bonding is homogeneous on the surface, the equation of moments around the point O is

$$P_{max}a^2\frac{a}{2} = mg\frac{d}{2} + M_{max}gx, \tag{7.3}$$

where m is the mass of one monolithic sapphire sample whose volume is $a \times a \times d$, M_{max} is the maximum weight the bond could hold and x is the distance between the bonding surface and the suspension point of the weight. So we can get an equation:

$$P_{max} = \frac{mgd}{a^3} + \frac{2g}{a^3}M_{max}x \tag{7.4}$$

to estimate the maximum strength of the bond. The maximum weight was 390 g and x was 35 mm. Therefore, the maximum strength is $\sim$ 2 MPa. This result shows that the indium bonding has a potential to hold the mirror weight in terms of strength.

Chapter 8

Impact of vibration from cooling systems

There are several methods to cool down the system. For KAGRA there were two candidates, one is using liquid helium and the other is using a pulse tube cryocooler which is based on the adiabatic expansion system. Because the cryogen (liquid helium) can not be used in the tunnel for safety, pulse tube cryocoolers will be used to cool down the cryogenic suspension. The principle of the pulse tube is the followings. High pressure He gas expands at the cooling part to absorb heat, then the gas is sent to a compressor in order to be compressed and cooled by coolant water. This cycle cools the cryocooler head and produces pulsing vibration around 1 Hz depending on the types of the cryocooler. KAGRA will use four cryocoolers made by the Jecc Torisha Co. Ltd. [85] per cryostat. This cryocooler has two stages. The 1st stage has 36 W of cooling power at 50K. The 2nd stage has 0.9 W at 4 K. The vibration estimate in the cryostat based on a vibration measurement, the effect on the KAGRA sensitivity and one of the improvement candidates are explained in the latter chapter. The contents of this study of the vibration noise from the cooling system were published in a scientific journal, Class. Quantum Grav. [86].

8.1 Vibration path from cooling systems

Figure 8.1 shows the cooling system of KAGRA for one cryogenic payload.

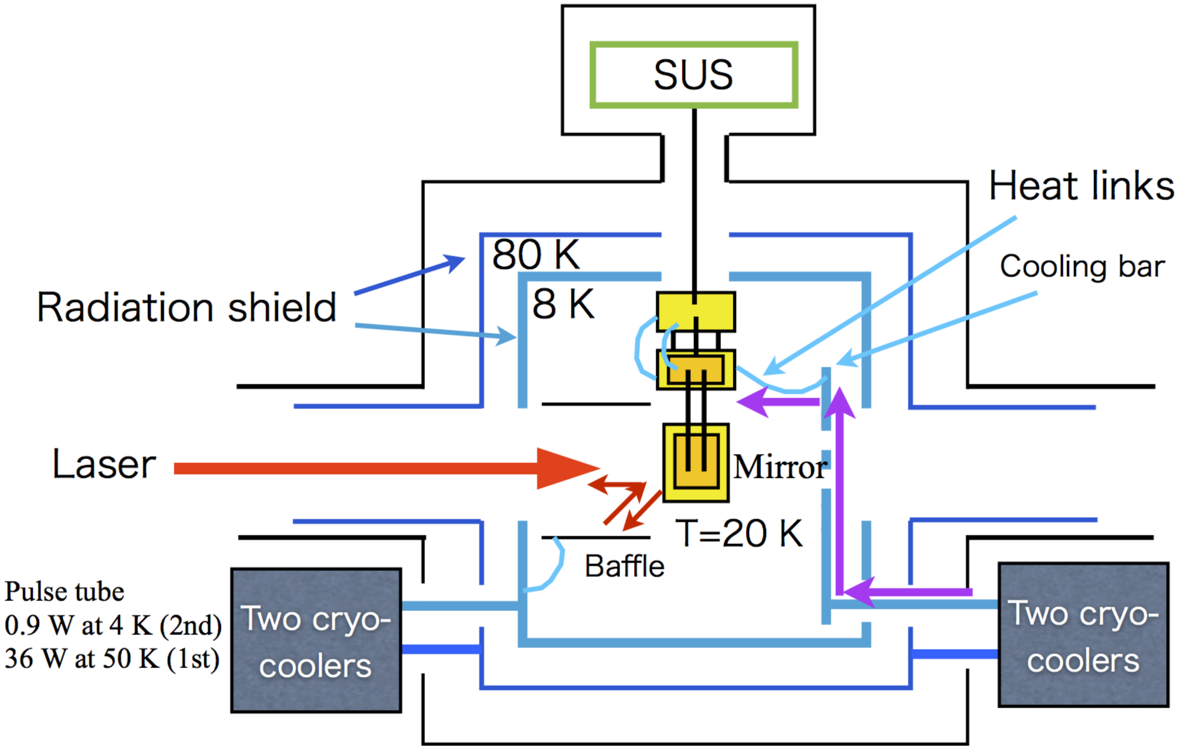

Figure 8.1: Cooling system of KAGRA. The cryogenic suspension system is surrounded by two radiation shields. The heat links are connected between the cryogenic suspension and the cooling bar which is connected to the cryocooler. The vibration of the cryocoolers can transfer through the cooling bar and the heat links. To suppress the vibration, the cooling bar should fixed on the radiation shield mechanically. Therefore, radiation shield vibration can the noise source.

Each cryogenic payloads will be surrounded by double-stage radiation shield (80 K shield and 8 K shield), as shown in Fig.8.1; four cryocoolers will be used to cool one cryogenic system including a cryogenic suspension and two radiation shields. All of the 1st stages of the four cryocoolers will be connected with the 80 K shield which is called the outer shield. The 2nd stage of two cryocoolers will cool the inner shield or the 8 K shield. The 2nd stage of the other two cryocoolers will be connected with the cryogenic suspension to cool it. This heat path is very important for cooling the suspension at low temperatures because the conduct cooling will dominate the cooling power at low temperatures. Vibrations from outside can also pass through this cooling path. The most straightforward design of this path to suppress the vibration is fixing the cooling bar which extends from the 2nd stage of the cryocooler into the inner radiation shield against a massive body like radiation shield and using heat links made of soft material which has high thermal conductivity at low temperatures such as pure aluminum or copper to connect the suspension and the top of the cooling bar. What should be considered is that the connection point between the cooling bar and the radiation shield should be separated thermally in order to separate the cooling system of the cryogenic suspension and the inner radiation shield to keep the suspension at low temperatures. For this purpose, low thermal conductivity material can be placed at an intermediate position between the radiation shield and the cooling path for the suspension. This connection point has not been decided. In this thesis, the cooling bar is assumed to be rigidly fixed on the inner radiation shield. Therefore, the cooling system can be a displacement noise source for KAGRA. In order to learn the influence from the vibration of the cooling system before all the systems are built, the vibration in the cryostat at low temperatures was measured in a factory of the Toshiba company which produced the cryostats in the Yokohama city during the cooling test of the cryostat. Because the seismic motion in this factory is much larger than that in the Kamioka mine, the vibration in the Kamioka mine should be estimated from the measured data. The methods and the results are shown in the following sections.

8.2 Vibration measurement of KAGRA radiation shield

8.2.1 Measurement setup

In order to measure the vibration in the KAGRA cryostat at low temperatures two cryogenic accelerometers were used and a room temperature accelerometer which is a commercial one (RION accelerometer LA-50) [87] was used as a reference. The cryogenic accelerometers were put on the inner radiation shield and put the RION accelerometer outside the cryostat. Figure 8.2 shows the position of the accelerometers.

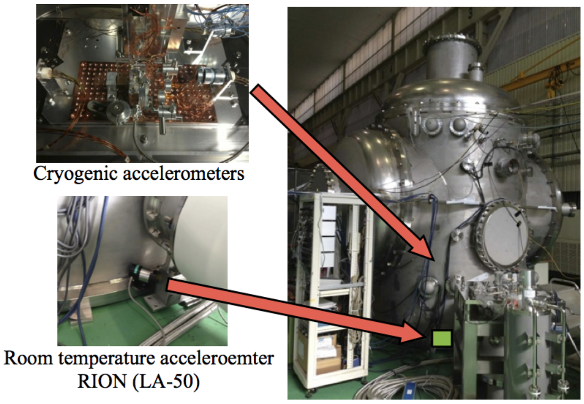

Figure 8.2: KAGRA cryostat and positions of the accelerometers. Two developed cryogenic accelerometers were fixed on the radiation shield in the cryostat. An commercial accelerometer is used to measure the vibration outside the cryostat.

8.2.2 Cryogenic accelerometers

The author and colleagues used two cryogenic accelerometers to measure the vibration at low temperature. One of them, which measured the vertical component of the vibration was developed at the University of Rome *Sapienza* [88], and the other one which measures the horizontal component was developed at the Institute for Cosmic Ray Research of the University of Tokyo [89]. The pictures of the accelerometers are shown in Fig.8.3.

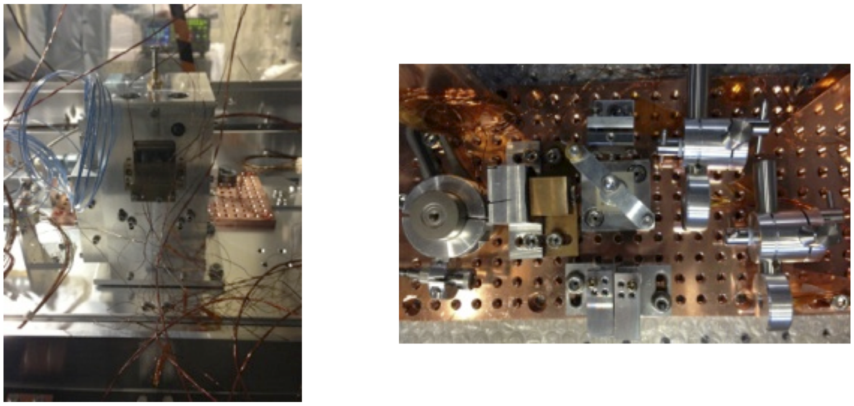

Figure 8.3: Accelerometers we used for the vibration measurement. Left one is the accelerometer for the vertical measurement. Right one is for the horizontal component.

The horizontal accelerometer, whose schematic figure is shown in Fig.8.4, is based on a Michelson interferometer.

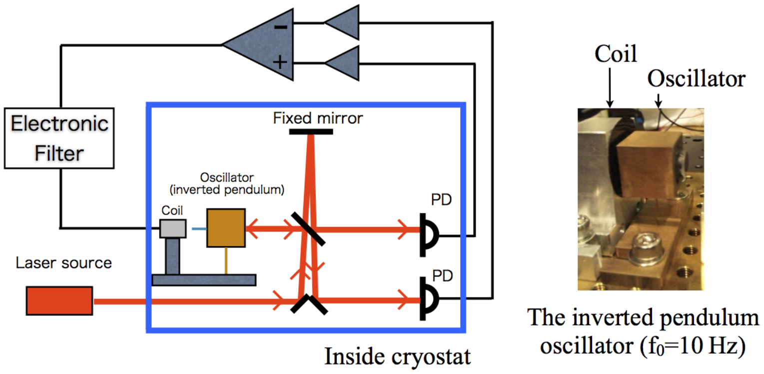

Figure 8.4: Schematic view of the horizontal accelerometer and the pendulum on the accelerometer. This accelerometer is made based on a Michelson interferometer. One of the mirror is fixed on the shield and the other mirror is on an oscillator, which is controlled the possession by a coil-magnet actuator. The signals of the interferometer are monitored by two photo detectors. And the readout circuits and the electronic filter are outside the cryostat.

There is an inverted pendulum ($f_0 = 10\,\mathrm{Hz}$) which has a mirror on a side placed on the optical plate made of copper. When the copper plate moves, the oscillator is applied by an inertial force which can be observed by the Michelson interferometer. The interferometer has two mirrors: one is fixed on the copper plate and the other one is attached on the oscillator. In order to put the laser source outside the cryostat, a single mode optical fiber was used to lead the laser light (10 mW, 1538 nm) from the source to the accelerometer in the cryostat. In order to keep the position of the oscillator in the linear range of the Michelson interferometer, we control the position by a coil magnet actuator using the signal from the two photo detectors (InGaAs type: Thorlabs FGA21[90]) monitored the light power at the symmetric and anti-symmetric ports. Below the unity gain frequency of this control system the provided force on the coil magnet actuator is the same as the inertial force because of the vibration. The acceleration was calculated from this feedback signal.

The vertical accelerometer[1] has a mass suspended by a spring in it. We monitored the inertial force applied to this mass using a linear variable differential transformer sensor and control the position of the mass by a voltage-force transducer. The force we apply to the mass should be the same as the inertial force on the mass below the unity gain frequency as the horizontal accelerometer.

8.2.3 Measurement result

At low temperatures we measured the vibration inside the cryostat and outside the cryostat to compare and evaluate the influence of the cryostat on the vibration. To estimate the influence because of the cryocoolers, we compared the vibration with the coolers on and off.

Measurement results of the vibration inside and outside the cryostat at 10 K are shown in Figs.8.5 and 8.6.

---

[1] This accelerometer is developed by collaborators in the Rome university.

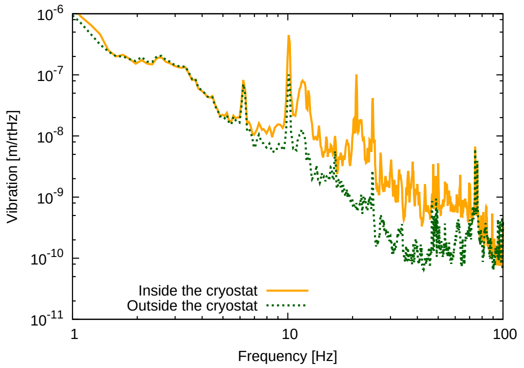

Figure 8.5: Horizontal vibration inside and outside the cryostat (T=10 K). The vibration in the cryostat is higher than that outside the cryostat at high frequency.

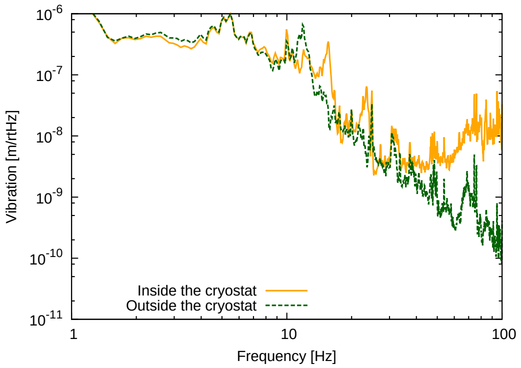

Figure 8.6: Vertical vibration inside and outside the cryostat (T=10 K). The vibration on the radiation shield is higher than the vibration outside the cryostat.

In the low frequency range (up to ∼ 10 Hz) the vibration inside the cryostat and outside the cryostat coincide each other. In the high frequency band the differences between inside and outside become significant. In the case of horizontal component, the vibration inside the cryostat is larger than outside the cryostat in the frequency range between 7 Hz and 80 Hz. As for the vertical component, the vibration inside is larger than that outside the cryostat above 40 Hz. But there are also some differences around 10 Hz. This difference between inside and outside starting around 10 Hz is reasonable because of the cryostat structure. According to a FEM simulation[2] of the cryostat including the vacuum chamber and the radiation shields, there are many resonance modes of the cryostat from this frequency. In the Kamioka mine, we assume this ratio between the outside and inside is the same as these measurements.

Figures 8.7 and 8.8 are the vibration of the inner shield during cryocoolers operating and without operation.

---

[2] This work was done by a collaborator of KEK.

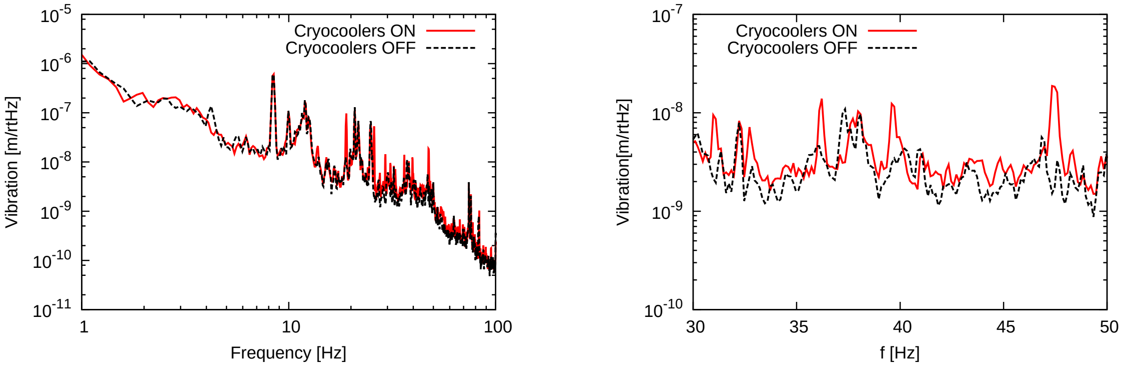

(a) (b)

Figure 8.7: (a)Vibration of the inner shield at 10 K with the cryocoolers switched ON and turned OFF for the horizontal component. (b)Zoom view between 30-50 Hz. Peaks appear when the cryocooler were turned ON.

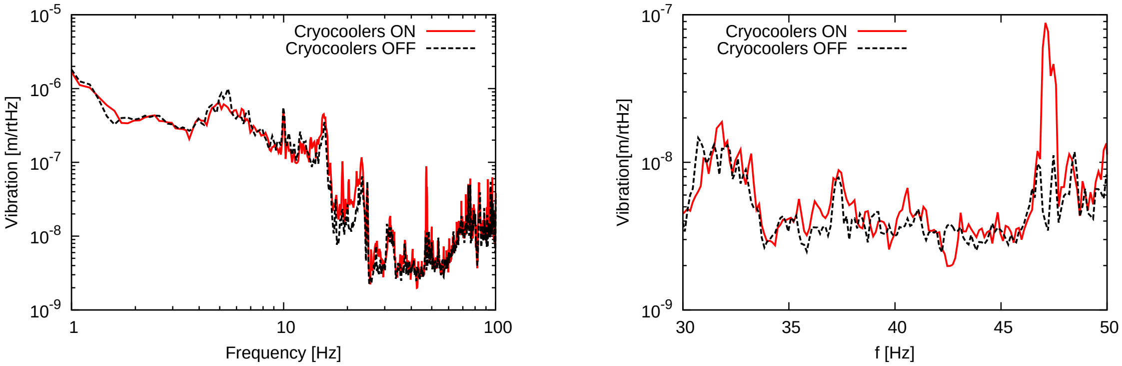

(a) (b)

Figure 8.8: (a)Vibration of the inner shield at 10 K with the cryocoolers switched ON and turned OFF for the vertical component. (b)Zoom view between 30-50 Hz. Peaks appear when the cryocooler were turned ON.

There are not significant changes due to the cryocoolers in the view of the wide frequency range for both horizontal and vertical components. But if we look at the spectrum carefully, there are many peaks due to the cryocoolers operation. We suppose these peaks will appear in Kamioka mine with the same amplitude as in these measurements. In order to estimate the peaks, we set a threshold value for the ratio of the vibration with cryocoolers ON to the vibration with cryocoolers OFF. The threshold values were 1.7 for the vertical component and 2.1 for the horizontal component. These values were 2σ of the deviations of the ratio.

8.3 Estimation of radiation shield vibration in Kamioka mine

In order to estimate the radiation shield vibration in Kamioka mine, we analyzed our data as the following. We calculated the ratio between the vibration inside and outside the cryostat and multiply a vibration in the Kamioka mine. We used the same data set for the horizontal and vertical vibration in the Kamioka mine because their difference is negligible. Then we added the peaks because of the cryocoolers on the calculated vibration. Figure 8.9 shows the estimated vibration of the inner shield in the Kamioka mine.

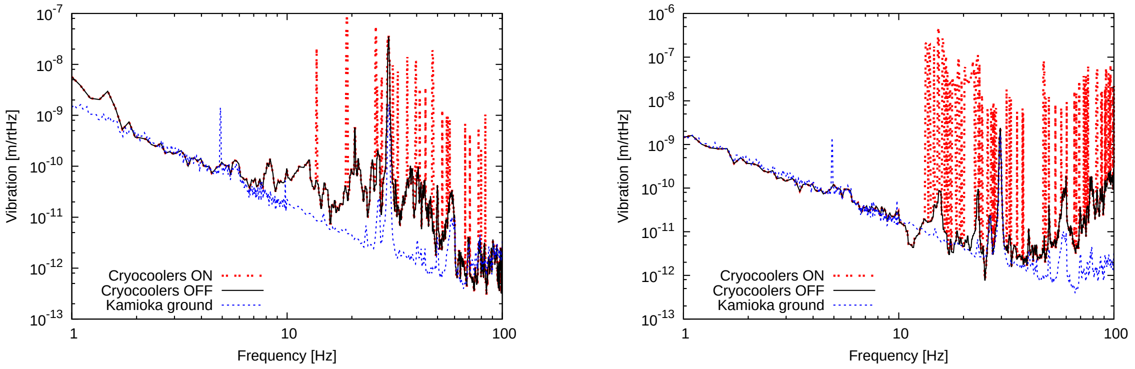

(a) (b)

Figure 8.9: Estimated vibration of the inner shield in Kamioka mine. (a) Horizontal component, (b) Vertical component. Blue lines show the ground vibration in Kamioka mine, black lines are the inner shield vibration without coolers operation and red lines indicates the vibration of the inner shield during the coolers operation.

As the figure shows, many peaks will appear when we turn ON the cryocoolers. In the next section the impact of this inner shield vibration on the KAGRA sensitivity is described.

8.4 Estimated effect on the KAGRA sensitivity

In this section, we assumed the most realistic cryogenic suspension system and estimated the displacement noise on the main mirror due to the inner shield vibration through the cooling path such as heat links and cryogenic suspension. The suspension model we used is shown in Fig.8.10.

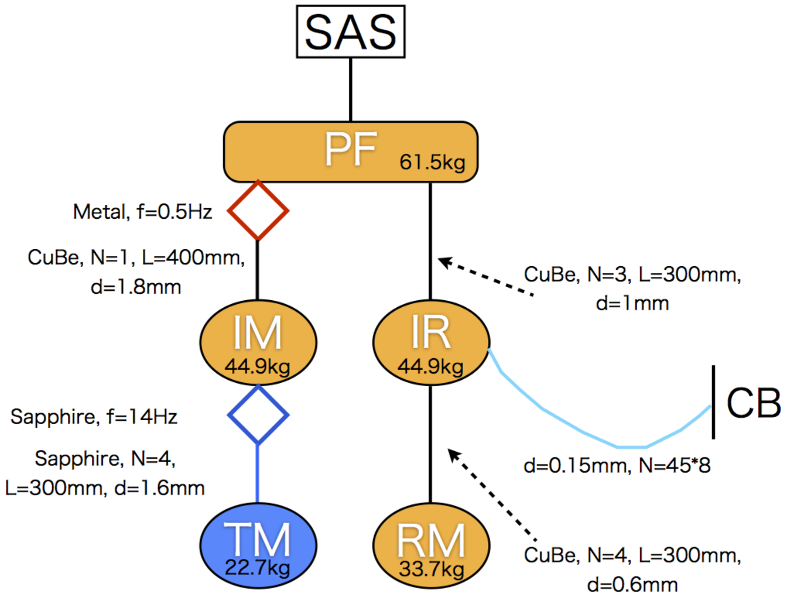

Figure 8.10: Cryogenic suspension system model we used for the vibration calculation. In this figure, where N, L and d mean the number, length and diameter of the cables or fibers. The dark blue parts are made of sapphire: sapphire suspension system. CB is the fixing point of the cooling bar. We assume this point has the same vibration as the vibration of the radiation shield we estimated.

In this figure TM, IM, PF, IR and RM are the test mass or main mirror, intermediate mass, platform, recoil mass for the intermediate mass and recoil mass for the main mirror. Simulation tool we used is a Mathematica code named SUMCON introduced in [46]. From the displacement noise we calculate the strain noise of KAGRA as shown in Figures 8.11.

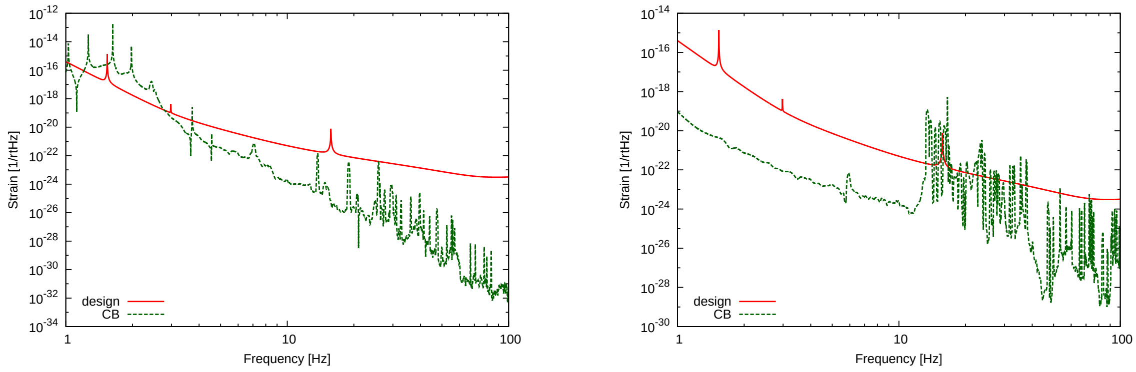

(a) (b)

Figure 8.11: Estimated noise from the cooling system including the vibration of cryocoolers. (a) Horizontal vibration origin, (b) vertical vibration origin. In the case of vertical components, noise from the vibration is over the KAGRA design sensitivity at important frequency range ∼10 Hz.

The result shows that there will be noises over the KAGRA design sensitivity in the region of several ten Hz due to the vertical vibration of the inner shield. In this frequency region, there are important frequencies of known pulsar souses like Vela (22.4 Hz). Therefore an additional system of the vibration reduction for the cooling system is necessary. In the next chapter, as a candidate, an additional vibration attenuator system which can suppress the impact from the inner shield vibration is presented.

Chapter 9

Discussion

In this chapter, the study of the sapphire suspension and the vibration noise from the cooling system are summarized and discussed.

9.1 Sapphire suspension

9.1.1 Thermal noise

In the above chapter, the measurements of the mechanical loss of the fibers, indium bonding and HCB were reported. All of them have lower mechanical losses than the requirements. In the case of sapphire fiber, type B fiber has mechanical loss of 1.1×10^{-7} which is better than the requirement of 2×10^{-7} by a factor of 2 at 16 K. The measured mechanical loss of indium bonding was 3.1×10^{-3} at 20 K, which is also better than the required value of 1.5×10^{-2} by a factor of 5. Finally the mechanical loss of HCB was 1.0 at 20 K which is the same as the requirement. Now these measured data can be used to estimate the total suspension thermal noise of the sapphire suspension system. For the other part of the sapphire suspension, the mechanical loss of a sapphire bulk $\phi_{Bulk} = 4.0 \times 10^{-9}$, which was measured by T. Uchiyama et al. [84] was assumed. The calculated result is shown in Fig.9.1. In this graph the thermal noise from the coating is also included [44]. The thickness of HCB is 60 nm and that of the indium bonding is $1\,\mu$m in this calculation.

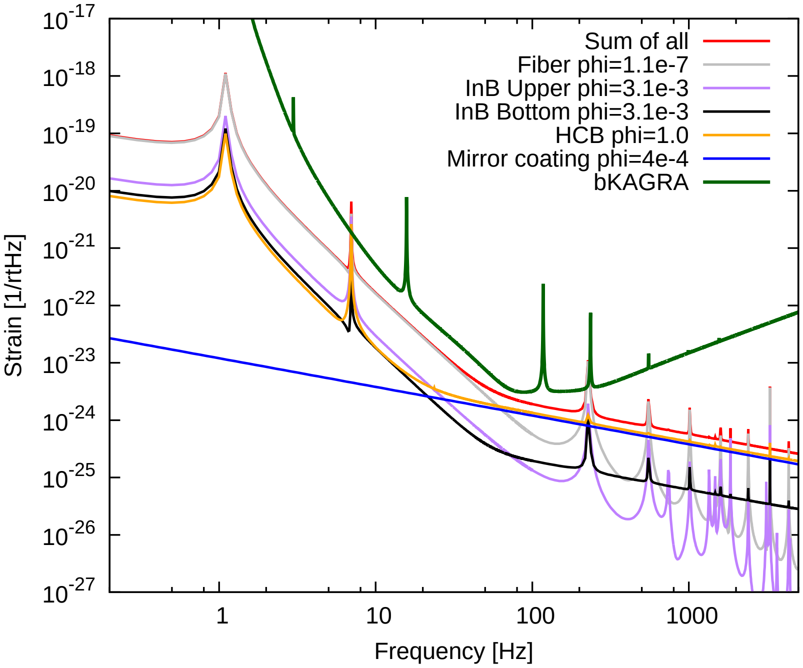

Figure 9.1: Thermal noise of KAGRA cryogenic sapphire suspension system calculated from the measured mechanical loss values. Mirror coating thermal noise is also plotted on the graph. The sum of the suspension thermal noise and the coating thermal noise is shown as a red line, which is lower than the KAGRA design sensitivity: green line.

According to this calculation, in the frequency region below 60 Hz, the thermal noise from the sapphire fibers are dominant. Above this frequency, the coating thermal noise and the noise from HCB will dominate the thermal noise. In all the frequency band the thermal noise does not exceed the target sensitivity of KAGRA. In order to improve the thermal noise of HCB around 100 Hz, the heads of the fibers can be smaller as described in the section 4.3.2.

9.1.2 Heat extraction

During the operation of the KAGRA main interferometer, about 500 mW heat should be extracted by the sapphire suspension system from the mirror. Even if almost all the parts of the sapphire suspension system are made of sapphire whose thermal conductivity is very high at low temperatures, a thin part of the fibers and non-sapphire part of the bonds can have a significant resistance in terms of the heat transfer. The thermal conductivity of the fibers was measured, and we showed that two kinds of fiber satisfied the required value. According to our heat extraction test of the fibers, the mirror would be 20 K during the operation when the mirror absorption is 30 ppm cm^{-1} and the absorption of the coating is 0.5 ppm. This also suggests that the absorption of the mirror and the coating should not higher than the values. Also the measured thermal conductivity of the bonded sapphire samples using the indium bonding and HCB is much higher than the required values. The heat transfer coefficient κ/l of the measured indium bonded sample was

$\sim 1.6 \times 10^5\,\mathrm{W/m^2/K}$ at 20 K, which is higher than the required value of $3000\,\mathrm{W/m^2/K}$. In the case of HCB sample, the measured value at 20 K was $\sim 1.6 \times 10^5\,\mathrm{W/m^2/K}$, which is also higher than the required value of $1000\,\mathrm{W/m^2/K}$. Therefore, the bonds will not make a large temperature difference in the sapphire suspension.

9.1.3 Strength

To hold the mirror, the breaking stress of the each part should be high enough, especially of weak parts or unknown parts of the fiber and HCB.

The fiber strength test was performed by the Glasgow and Roma collaborators. The weight with which a fiber (30 cm in length) will be loaded in the KAGRA suspension will be ∼6 kg. The shaking test of 10 cm fibers with the load of 15 kg and the amplitude of 5-7 mm was performed, then all of the fibers survived. This suggests that the 30 cm fibers will survive even if the fiber is shaken with the load of 15 kg and the amplitude of ∼15 mm. (The stress by the shaking in the fiber is assumed to be inverse proportional to the fiber length.) The static braking test for the three kinds of fiber were performed, then all of them were shown to have sufficient strength for KAGRA. The breaking weight was 56kg (type A fiber) and 35kg (type B fiber). In the case of the type C, the fiber was not broken by the apparatus whose maximum weight was 90 kg.

For the strength of HCB, strength tests at cryogenic temperature after 10 or 20 thermal cycles were performed because the KAGRA sapphire suspension will also experience such thermal cycles. The measured strength were much higher than the required value of 1 MPa.

As above, the KAGRA mirror, which has 22.6 kg, can be suspended by our suspension system.

9.2 Vibration from cooling systems

In order to estimate the vibration from the cooling systems, radiation shield vibration measurements were performed during the cooling test of the cryostat in a factory. Vibration noise of the mirror from the radiation shield was estimated based on the measurement result. In the result this noise is over the design sensitivity of KAGRA. A method to reduce this noise is shown in this section.

9.2.1 Additional vibration attenuator system for the inner shield vibration

In order to suppress the vibration from the cooling system, we proposed an additional vibration attenuator system. This kind of attenuation system has already been proposed for Einstein Telescope [91]. A schematic view of the system is shown in Fig.9.2.

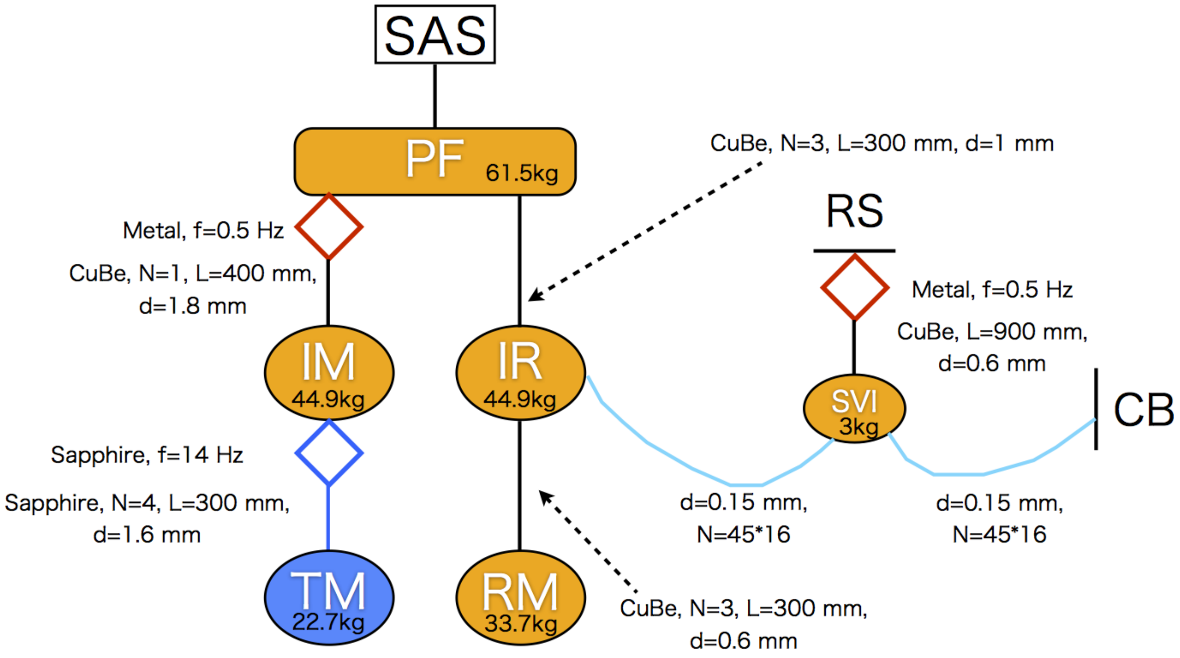

Figure 9.2: Cryogenic suspension system with an additional vibration attenuator system. The additional suspension is assumed to be attached on the radiation shield. This pendulum has a vertical spring to suppress the vertical vibration. Number of heat links are twice times larger than that without this vibration attenuator. Thus, the thermal resistance of total heat links is the same.

The cryogenic suspension system is the same as the previous model, but a pendulum is added. The space for this additional pendulum in the cryostat has already been checked by the CAD file of the cryostat, then there is enough space. Number of heat links are twice times larger than that without this vibration attenuator. Thus, the thermal resistance of total heat links is the same. This additional pendulum is suspended from the top of the inner radiation shield and have a 0.5 Hz vertical attenuation, which can be made by a Geometric Anti-Spring Filter (GASF) and a 900 mm length pendulums. Because we assumed the same vibration everywhere in the inner shield, we input the same vibration into the suspension point of the additional pendulum (RS) and the heat links fixing point (CB).

If we use this additional suspension, we can suppress the vibration as shown in Fig.9.3.

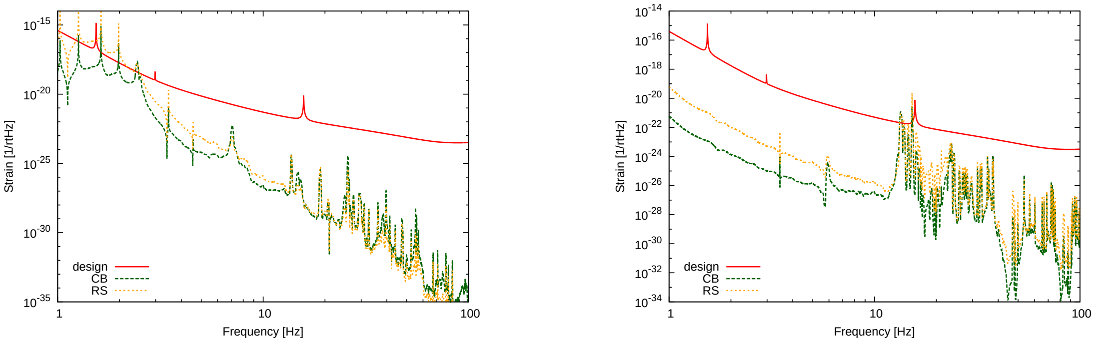

(a) (b)

Figure 9.3: Displacement noise from the radiation shield vibration with an additional suspension. The suspension model for this calculation is shown in Fig.9.2. There are two points the vibration can enter from to the suspension. One of them is the contact point of the heat links (CB). The other one is the suspension point of the additional suspension (RS). (a) Horizontal component. (b) Vertical component.

This figure shows the calculated noise from the radiation shield vibration assuming the suspension model shown in Fig.9.2. The red lines in the figures are the design sensitivity of KAGRA, the orange lines is the displacement noise from the vibration at the fixing point of the additional pendulum and the green lines mean the noise from the connection point between heat links and the radiation shield. In almost all the frequency range the noise can be suppressed below the design sensitivity of KAGRA.

9.3 KAGRA sensitivity

In this section estimated KAGRA sensitivity which contains the thermal suspension noise and the vibration noise from the cryostat is shown.

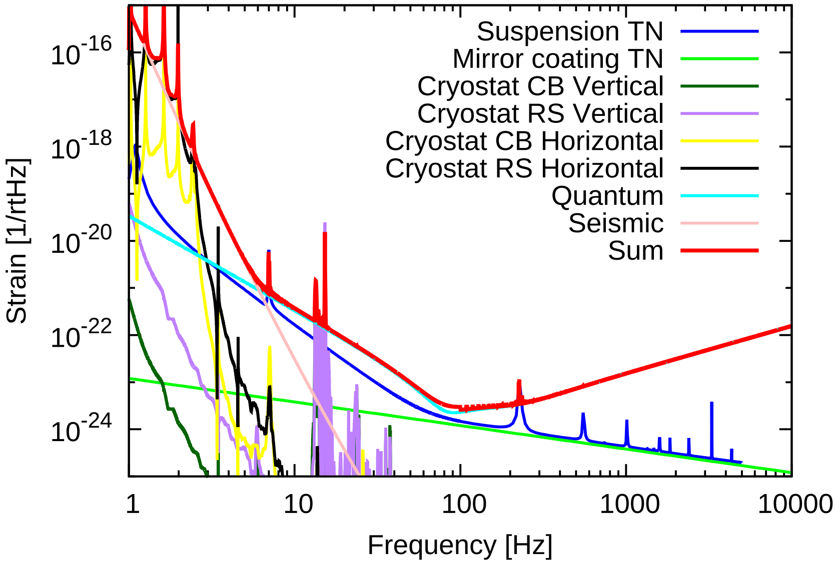

Figure 9.4: Estimated KAGRA sensitivity. Seismic noise, quantum noise, cooling system vibration noise, suspension thermal noise and mirror coating thermal noise are included. Almost all of the region of the frequency band will be limited by the seismic noise and the quantum noise.

Figure9.4 shows the estimated sensitivity of KAGRA. Seismic noise through the large suspension system will limit the low frequency range, and the quantum noise will mainly limit the higher frequency range. Seismic noise and quantum noise are the latest version which are openly available on the web [75]. Noises described in this thesis are lower than the quantum noise in the best frequency band of KAGRA: the influence of the suspension thermal noise and vibration of the cryostat on the sensitivity is enough small.

9.4 Future work

All of the worrisome or unknown components of the sapphire suspension system were studied and found to satisfy the requirements at last, which are reported in this thesis. Based on the results reported in this thesis, the decision to move to the next step was taken: building a complex system. First, a study of the system so called "one fiber prototype" will be proceeded, which consists of a sapphire mass, which is a quarter of the KAGRA mirror, an ear attached on the mass by HCB, a 10 cm sapphire fiber and a blade. Indium bonding will also be used in this prototype between the ear and the fiber, the fiber and the blade. Mechanical measurements of the blade such as the bending distance by the load and the resonance frequency changes depending on the temperature can be fruitful measurements. Bonding and detachment process of the indium bonding for the complex system can be improved by this one fiber prototype. Mechanical loss measurement and heat load measurement at low temperatures can also performed.

Next a real size sapphire suspension using a dummy mirror will be constructed. Cooling test, mechanical loss measurement and heat load test at low temperatures can be performed for this suspension.

At last the the same fabrication process will be applied on the real KAGRA mirror.

The first step has already started: building the one fiber prototype. Pictures of the suspended one type prototype are shown in Fig.9.5.

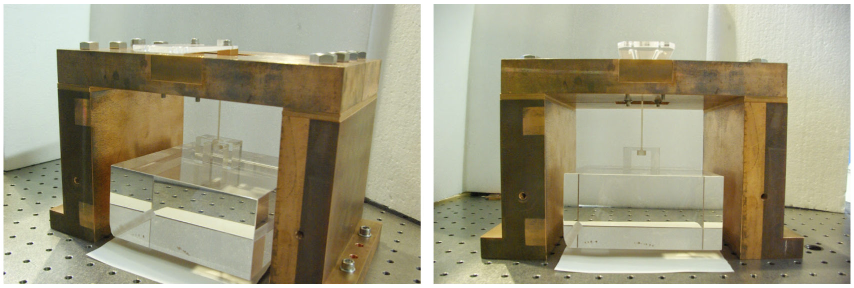

Figure 9.5: One fiber prototype. An ear is attached on a sapphire mass by HCB. The mass is suspended by a 10 cm sapphire fiber, which is hung from a sapphire blade. Cooling test, heat extraction test and mechanical loss measurement are planed.

The strength of the fiber, HCB and blade are sufficient at least under static loading.

Vibration measurement of the cryostat in the Kamioka mine will be performed after the install of the KAGRA cryostats. Same measurements as the measurement reported in this thesis can be performed. The install of the cryostats is on going now in the Kamioka mine.

Chapter 10

Conclusion

The 3 km length laser interferometer gravitational wave telescope KAGRA will cool the main mirrors in order to suppress the thermal noise. This is the first challenge for the km-scale telescopes in the world. The mirror will be suspended to be a “free” mass for the gravitational wave and suppress the seismic vibration influence. The mirror will be suspended by four sapphire fibers in the system. The cryogenic suspension system, including the mirror will be connected with the cryocoolers via metal heat links. The thermal noise of this sapphire suspension system and the vibration noise of the cooling system was described in this thesis.

Sapphire fibers with heads and two kinds of bonding (indium bonding and Hydroxide Catalysis Bonding:HCB) are necessary for the sapphire suspension system. To design the sapphire suspension system and estimate the suspension thermal noise, mechanical loss measurements for sapphire fibers, indium bonding and HCB at low temperatures were performed. As a result, a kind of fiber, which was manufactured by Heat Exchanger Method and thermal-polished was shown to have a lower mechanical loss than the requirement. Also, the bonding satisfied the requirement for the mechanical loss. The heat extraction test for the fibers and bonded samples via HCB and indium were performed. Fibers had high thermal conductivity and we concluded that the bonds will not have significant thermal resistance in the sapphire suspension. All of the worrisome or unknown components of the sapphire suspension system were studied and found to satisfy the requirements, which are reported in this thesis. In other words, according to these measurements in this thesis, the design of the sapphire suspension system including the connections by the bonding techniques is fixed.

Vibration measurement of the KAGRA cryostat was performed in the factory. The displacement noise from the cooling systems was estimated to impair the KAGRA sensitivity slightly in the limited band at low frequencies. However, the investigation in this thesis revealed that adding an attenuation system could solve the problem.

Therefore, we are now quite confident that we can construct a cryogenic sapphire suspension using these components and techniques and also the vibration due to the cooling systems will not make a significant noise.

In order to create new astronomy via gravitational waves, extremely sensitive interferometer gravitational wave telescopes such as Advanced LIGO, Advanced VIRGO, GEO and KAGRA are under upgrading or being built currently. KAGRA will be the first km-scale cryogenic telescope using the cryogenic mirror suspension systems, which will be necessary for the future ground based telescopes including the Einstein Telescope. Cryogenic type interferometers have the possibility to achieve much higher sensitivity, which can observe more gravitational wave events and discover new physics and astronomy. Therefore, the study in this thesis about the cryogenic suspension is a significant milestone for the future gravitational wave telescopes and also for a new gravitational wave astronomy.

Appendix A

Shear strength calculation

The relationship between applied torque and shear strength in the HCB strength test is shown in this appendix [92]. When the maximum torque T is applied on the sapphire sample, a constant torsion α is assumed in the sample. Displacement u_x, u_y, u_z can be written as below.

$$u_x = -\alpha z y \tag{A.1}$$

$$u_y = \alpha z x \tag{A.2}$$

$$u_z = 0 \tag{A.3}$$

The thickness of HCB is assumed to be enough thiner than the sapphire. Because the relationship between displacement u and strain ϵ is

$$\epsilon_{ij} = \frac{1}{2}\left(\frac{\partial u_i}{\partial x_j} + \frac{\partial u_j}{\partial x_i}\right), \tag{A.4}$$

strain ϵ can be written as below.

$$\epsilon_{yz} = \frac{1}{2}\alpha x \tag{A.5}$$

$$\epsilon_{zx} = -\frac{1}{2}\alpha y \tag{A.6}$$

$$\epsilon_{xx} = \epsilon_{yy} = \epsilon_{zz} = \epsilon_{xy} = 0 \tag{A.7}$$

Stress σ and strain ϵ have relationships in a xy plane.

$$\sigma_{xx} = \frac{Y}{1-\nu^2}(\epsilon_{xx} + \nu\epsilon_{yy}) = 0 \tag{A.8}$$

$$\sigma_{yy} = \frac{Y}{1-\nu^2}(\epsilon_{yy} + \nu\epsilon_{xx}) = 0 \tag{A.9}$$

$$\sigma_{xy} = \frac{Y}{1+\nu}\epsilon_{xy} \tag{A.10}$$

$$\sigma_{yz} = \frac{Y}{1+\nu}\epsilon_{yz} \tag{A.11}$$

Y is Young's modulus and ν is Poisson's ratio. Modulus of rigidity G is described as following using Y, ν.

$$G = \frac{Y}{2(1+\nu)} \tag{A.12}$$

Stress σ on the bonding surface can be described as the following.

$$\begin{aligned} \sigma_{yz} &= G\alpha x && \text{(A.13)} \\ \sigma_{zx} &= -G\alpha y && \text{(A.14)} \\ \sigma_{xx} &= \sigma_{yy} = \sigma_{zz} = \sigma_{xy} = 0 && \text{(A.15)} \end{aligned}$$

Summation of these moments equals to the applied torque T.

$$\begin{aligned} T &= \int\int (x\sigma_{yz} - y\sigma_{xz})\mathrm{dxdy} && \text{(A.16)} \\ &= G\alpha \int\int (x^2 + y^2)\mathrm{dxdy} && \text{(A.17)} \end{aligned}$$

The maximum shear stress τ_{max}, which is assumed the stress at the corner can be written as below.

$$\begin{aligned} \tau_{max} &= \sqrt{\sigma_{yz}^2 + \sigma_{xz}^2} && \text{(A.18)} \\ &= G\alpha\sqrt{a^2 + b^2} && \text{(A.19)} \\ &= \frac{T}{\int\int (x^2 + y^2)\mathrm{dxdy}}\sqrt{a^2 + b^2} && \text{(A.20)} \end{aligned}$$

Acknowledgements

It is a great pleasure to thank all the people who made this thesis possible.

First and foremost I would like to thank Professor Seiji Kawamura. He is not only my reliable supervisor but also the person who gave me the first attractive introduction into gravitational wave research 6 years ago when I was an undergraduate student. Without his introduction, continued advice and support this thesis would not have been possible.

I also want to thank the members in the KAGRA cryogenic group. Especially Dr. Kazuhiro Yamamoto and Dr. Aleksandr Khalaidovski gave me a lot of advice and took the time to discus with me. Dr. Toshikazu Suzuki, Dr. Nobuhiro Kimura, Dr. Takayuki Tomaru and Dr. Rahul Kumar at KEK also gave me much advice in meetings and in the lab. I am also indebted to Dr. Chihiro Tokoku who was a technician of ICRR and Mr. Shigeak Koike who was a technician of KEK. They were very helpful and supportive for my study.

There were many supports from Europe for this study. I wish to express my thanks to Dr. Luca Naticchioni, Dr. Andrea Conte, Dr. Paola Puppo and Dr. Ettore Majorana in the Rome University. They supported the vibration measurements of the KAGRA cryostat, mechanical loss measurements of sapphire fibers and simulations using ANSYS. Moreover, I must acknowledge the useful suggestion and helpful supports from Mr. Gerd Hofmann, Mr. Julius Komma, Dr. Christian Schwarz, Dr. Daniel Heinert and Dr. Ronny Nawrodt at the Jena University. The mechanical loss measurements of bondings and simulations using COMSOL were powerfully supported by them. Dr. Karen Anne Haughian and Ms. Rebecca Douglas in the Glasgow University kindly taught us the basically techniques about the HCB. I appreciate their useful advice and collaboration.

I would like to thank my current and previous office mates, especially Mr. Yusuke Sakakibara, Mr. Takanori Skiguchi, Ms. Yumiko Ejiri, Mr. Masayuki Nakano, Mr. Kenji Ono, Mr. Hiroki Tanaka and Mr. Takahiro Miyamoto. Their technical, physical and psychological support made my PhD an enjoyable and fruitful experience.

Finally, I would like to thank all of my family for their limitless love, patience and support.

Reference

[1] Albert Einstein, S. B. Preuss. Akad. Wiss. (1916) **33** 688.

[2] J.H.Taylor et al., [Furhter experiment tests of relativistic gravity using the binary pulser PSR 1913+16], The Astrophysics Journal(1989)

[3] G. M. Harry, [Advanced LIGO: the next generation of gravitational wave detectors] CQG, **27** (2010) 084006

[4] https://wwwcascina.virgo.infn.it/advirgo/

[5] The Virgo Collaboration, [Advanced Virgo Technical Design Report, Technical Report] (2012) https://tds.ego-gw.it/ql/?c=8940

[6] H. Luck et al., [The upgrade of GEO 600] (2010) J. Phys.: Conf. Ser. **228** 012012

[7] K. Somiya for the KAGRA collaboration, [Detector configuration of KAGRA—the Japanese cryogenic gravitational-wave detector] Class. Quantum Grav. **29** 124007 (2012)

[8] R. X. Adhikari, [Gravitational Radiation Detection with Laser Interferometry] (2014) arXiv:1305.5188v3

[9] K. Arai et al., [Status of Japanese gravitational wave detectors] 2009 Class. Quantum Grav. **26** 204020

[10] H. Grote for the LIGO Scientific Collaboration [The GEO 600 status] 2010, Classical and Quantum Gravity **27** 084003.

[11] T. Accadia et al., [Virgo: a laser interferometer to detect gravitational waves] (2012) JINST **7** P03012

[12] B. P. Abbott et al., [LIGO: the Laser Interferometer Gravitational-Wave Observatory] (2009) Rep. Prog. Phys. **72** 076901

[13] B. Sathyaprakash et al., [Scientific objectives of Einstein Telescope] (2012) Class. Quantum Grav. **29** 124013

[14] K. Agatsuma et al., [Thermal-noise-limited underground interferometer CLIO] 2010 Class. Quantum Grav. **27** 084022

[15] T. Uchiyama et al., [Reduction of Thermal Fluctuations in a Cryogenic Laser Interferometric Gravitational Wave Detector] 2012 Phys. Rev. Lett. **108** 141101

[16] K. Yamamotos et al., [Vibration measurement in the cryogenic interferometric gravitational wave detector (CLIO interferometer)] 2006 Presentation at Physical Society of Japan http://gwdoc.icrr.u-tokyo.ac.jp/DocDB/0004/G0600422/001/PSJ0603.pdf

[17] T. Uchiyama et al., [Mechanical quality factor of a sapphire fiber at cryogenic temperatures] Physics Letters A **273** (2000) 310—315

[18] Yu Levi, [Internal thermal noise in the LIGO test masses: A direct approach] Physical Review D, **57** (1998) 2

[19] T. Uchiyama et al., [Cryogenic cooling of a sapphire mirror-suspension for interferometric gravitational wave detectors] Physics Letters A **242** (1998) 211-214

[20] T. Suzuki et al., [APPLICATION OF SAPPHIRE BONDING FOR INTERFEROMETRIC GRAVITATIONAL WAVE DETECTOR WITH CRYOGENIC MIRRORS] International Journal of Modern Physics A **20** No. 29 (2005) 70607062

[21] F. Romero B. and H. Dehnen, [Generation of Gravitational Radiation in the Laboratory] Zeitschrift Naturforschung Teil A **36**, 948

[22] Masumura, [Analysis of continual gravitational waves using TAMA 300 data (Japanese)] Master thesis of the University of Tokyo (2005)

[23] J. Aasi et al., [GRAVITATIONAL WAVES FROM KNOWN PULSARS: RESULTS FROM THE INITIAL DETECTOR ERA] arXiv:1309.4027 (2014)

[24] Charles J. Lada, [STELLAR MULTIPLICITY AND THE INITIAL MASS FUNCTION: MOST STARS ARE SINGLE] The Astrophysical Journal **640**: L64-L66, 2006

[25] Y. Sekiguchi, et al., [Effects of Hyperons in Binary Neutron Star Mergers] Phys, Rev, Lett. **107** (2011) 211101

[26] Abadie, et al., [Predictions for the rates of compact binary coalescences observable by ground-based gravitational-wave detectors] CQG, **27** (2010) 173003

[27] Christian D Ott, [The gravitational-wave signature of core-collapse supernovae] CQG, **26** (2009) 063001

[28] B. Allen, [Stochastic gravity-wave background in inflationary-universe models] Phys. Rev. D, **37** 2078 (1988)

[29] M. S. Turner, [Detectability of inflation-produced gravitational waves] Phys. Rev. D, **55** R435 (1997)

[30] Steven Weinberg, [Damping of tensor modes in cosmology] Phys, Rev, D **69** (2004) 023503

[31] J. Weber, Phys. Rev. 117 (1960) 306

[32] J. Weber, Phys. Rev. Lett. 22 (1969) 1320

[33] Savas Dimopoulos, et al., [Atomic gravitational wave interferometric sensor] Phys. Rev. D, **78** (2008) 122002

[34] Masaki Ando, et al., [Torsion-Bar Antenna for Low-Frequency Gravitational-Wave Observations] Phys. Rev. Lett., **105** (2010) 161101

[35] P. A. Seoane et al., [The Gravitational Universe, Technical Report, Albert Einstein Institute Hannover] https://www.elisascience.org/whitepaper/

[36] N. Seto et al., [Possibility of Direct Measurement of the Acceleration of the Universe Using 0.1 Hz Band Laser Interferometer Gravitational Wave Antenna in Space] Phys.Rev.Lett. **87** (2001) 221103

[37] K. Somiya, [Detector configuration of KAGRA - the Japanese cryogenic gravitational-wave detector] ArXiv e-prints eprint 1111.7185 (2011)

[38] R. Abbott, et al., [Seismic isolation for Advanced LIGO] CQG, **19** (2002) 1591

[39] T. Accadia, et al., [LOW FREQUENCY NOISE, VIBRATION AND ACTIVE CONTROL] VOLUME **30** (2011) 1

[40] Yuk Tung Liu and Kip S.Thorne, [Thermoelastic noise and homogeneous thermal noise in finite sized gravitational-wave test masses] Phys, Rev, D **62** (2000) 122002

[41] K Numata, et al., [Wide-Band Direct Measurement of Thermal Fluctuations in an Interferometer] Phys. Rev. Lett., **91** (2003) 26

[42] G. M. Harry, [Thermal noise in interferometric gravitational wave detectors due to dielectric optical coatings] Class. Quantum Grav. **19** (2002) 897—917

[43] KAGRA Main Interferometer Working Group, [KAGRA Main Interferometer Design Document] KAGRA internal report (2014) http://gwdoc.icrr.u-tokyo.ac.jp/cgi-bin/DocDB/ShowDocument?docid=913

[44] K. Yamamoto, et al., [Measurement of the mechanical loss of a cooled reflective coating for gravitational wave detection] Phys. Rev. D **74** (2006) 022002

[45] F. Acernese, et al., [Advanced Virgo Baseline Design] The Virgo Collaboration note VIR-027A-09 (2009) https://tds.ego-gw.it/itf/tds/file.php?callFile=VIR-0027A-09.pdf

[46] T. Sekiguchi, [Modeling and Simulation of Vibration Isolation System for Large-scale Cryogenic Gravitational-wave Telescope (LCGT)] Master Thesis the University of Tokyo (2012) http://gwdoc.icrr.u-tokyo.ac.jp/cgi-bin/DocDB/ShowDocument?docid=770

[47] Toshiba Co., http://www.toshiba.co.jp/worldwide/index.html

[48] A. V. Cumming et al., [Design and development of the advanced LIGO monolithic fused silica suspension] Class. Quantum Grav. **29** (2012) 035003

[49] T. ACCADIA et al., [PROGRESSES IN THE REALIZATION OF A MONOLITHIC SUSPENSION SYSTEM IN VIRGO] Proceedings of the MG12 Meeting on General Relativity

[50] K. Hayama, [バイオリンモードの周波数について] Internal report of KAGRA (2014) http://gwdoc.icrr.u-tokyo.ac.jp/cgi-bin/private/DocDB/ShowDocument?docid=2825

[51] G. Gonzalez, [Suspensions thermal noise in the LIGO gravitational wave detector] Class. Quantum Grav. **17** (2000) 4409

[52] G. Gonzalez and P. R. Sauloson [Brownian motion of a mass suspended by an an elastic wire] J. Acoust. Soc. Am **96** (1), July (1994)

[53] Impex high tech http://www.impex-hightech.de/

[54] E. R. Dobrovinskaya et al., [Sapphire Material, Manufacturing, Applications] Springer Science+Business Media, LLC 2009

[55] G. Cagnoli et al., [Damping dilution factor for a pendulum in an interferometric gravitational waves detector] Physics Letters A 272 2000. 39—45

[56] Daniel Francis Fiore, [High Strength Diffusion Bonding of Sapphire] Master thesis of the Worcester Polytechnic Institute (2002)

[57] T. Uchiyama, [重力波レーザー干渉計用低温鏡の研究] Doctor thesis of the University of Tokyo (1999)

[58] Anna-Maria A. van Veggel and Christian J.K illow, [Hydroxide catalysis bonding for astronomical instruments] Adv. Opt. Techn. 2014; 3(3): 293-307

[59] E. J. Elliffe, J. Bogenstahl, A. Deshpande, et al.., [Hydroxide-catalysis bonding for stable optical systems for space] CQG, **22**:257, 2005

[60] R Douglas et al., [Cryogenic and room temperature strength of sapphire jointed by hydroxide-catalysis bonding] CQG **31** (2014) 045001

[61] D.-H. Gwo, US Patent no. US 6 284 085 B1 (2001)

[62] D.-H. Gwo, US Patent no. US6548176 (2003)

[63] D.-H. Gwo, SPIE Proc. 3435 136-42 (1998)

[64] Y.Sakakibara et al., [Progress on the cryogenic system for the KAGRA cryogenic interferometric gravitational wave telescope] CQG **31** (2014) 224003

[65] Y. Sakakibara et al., [A study of cooling time reduction of interferometric cryogenic gravitational wave detectors using a high-emissivity coating] AIP Conference Proceedings **1573**, 1176 (2014)

[66] H.B. Callen and T.A. Welton, [Irreversibility and Generalized Noise] Phys. Rev. **83** (1951) 34

[67] R.F. Greene and H.B. Callen, [On the Formalism of Thermodynamic Fluctuation Theory] Phys. Rev. **83** (1951) 1231

[68] H.B. Callen and R.F. Greene, [On a Theorem of Irreversible Thermodynamics] Phys. Rev. **86** (1952) 702

[69] R.F. Greene and H.B. Callen, [On a Theorem of Irreversible Thermodynamics. II] Phys. Rev. **88** (1952) 1387

[70] L. Cunningham et al., [Re-evaluation of the mechanical loss factor of hydroxide-catalysis bonds and its significance for the next generation of gravitational wave detectors] Physics Letters A **374** (2010) 3993

[71] J. B. WACHTMAN et al., [Exponential Temperature Dependence of Young's Modulus for Several Oxides] Phys. Rev. **122** (1961) 1754

[72] R. W. Chang, [INFLUENCE OF CRYOGENIC TEMPERATURE AND MICROSTRUCTURE ON FATIGUE FAILURE OF INDIUM SOLDER JOINT] Dissertation (2008)

[73] C. Zener, [Internal Friction in Solids. I. Theory of Internal Friction in Reeds] Phys. Rev. **52** (1937) 230

[74] C. Zener, [Internal Friction in Solids II. General Theory of Thermoelastic Internal Friction] Phys. Rev. **53** (1938) 90

[75] http://gwcenter.icrr.u-tokyo.ac.jp/researcher/parameters

[76] K. Somiya (for the KAGRA collaboration), [Detector configuration of KAGRA— the Japanese cryogenic gravitational-wave detector] 2012 Class. Quantum Grav. **29** 124007

[77] E. Hirose et al., [Sapphire for the LCGT project] http://gwdoc.icrr.u-tokyo.ac.jp/DocDB/0006/G1100664/001/GTAT_2011Sep30_hirose.pdf

[78] A. Khalaidovski et al., [Evaluation of heat extraction through sapphire fibers for the GW observatory KAGRA] Class. Quantum Grav. **31** (2014) 105004

[79] PHILTEC Inc http://www.philtec.com/

[80] L. Cunningham et al., [Re-evaluation of the mechanical loss factor of hydroxide-catalysis bonds and its significance for the next generation of gravitational wave detectors] Physics Letters A **374** (2010) 3993—3998

[81] T. Tomaru et al., [Maximum heat transfer along a sapphire suspension fiber for a cryogenic interferometric gravitational wave detector] Physics Letters A **301** (2002) 215—219

[82] Lake Shore Cryogenics http://www.lakeshore.com/Pages/Home.aspx

[83] Y. S. Touloukian, [Thermophysical Properties of Matter] 1970

[84] T. Uchiyama et al., [Mechanical quality factor of a cryogenic sapphire test mass for gravitational wave detectors] Physics Letters A **261** (1999) 5—11

[85] Torishya, http://www.jecctorisha.co.jp/index.html

[86] D. Chen et al., [Vibration measurement in the KAGRA cryostat] Class. Quantum Grav. **31** (2014) 224001

[87] RION CO., LTD. http://www.rion.co.jp/english/

[88] F. Frasconi et al., [A vertical accelerometer for cryogenics implementation in third-generation gravitational-wave detectors] Meas. Sci. Technol. **25** (2014) 015103

[89] M. Adier et al., [Progress and challenges in advanced ground-based gravitational-wave detectors] Gen. Rel. Grav. **46** (2014) 1749

[90] FGA21 www.thorlabs.co.jp/thorproduct.cfm?partnumber=FGA21

[91] M. Abernathy et al., [Einstein gravitational wave telescope conceptual design study document] 2011

[92] L. D. Landau and E. M. Lifshitz, [ランダウ=リフシッツ理論物理学教程シリーズ 弾性理論 (佐藤常三, 石橋善弘訳)] 東京図書 (1989)